



저작자표시-비영리-변경금지 2.0 대한민국

이용자는 아래의 조건을 따르는 경우에 한하여 자유롭게

- 이 저작물을 복제, 배포, 전송, 전시, 공연 및 방송할 수 있습니다.

다음과 같은 조건을 따라야 합니다:



저작자표시. 귀하는 원저작자를 표시하여야 합니다.



비영리. 귀하는 이 저작물을 영리 목적으로 이용할 수 없습니다.



변경금지. 귀하는 이 저작물을 개작, 변형 또는 가공할 수 없습니다.

- 귀하는, 이 저작물의 재이용이나 배포의 경우, 이 저작물에 적용된 이용허락조건을 명확하게 나타내어야 합니다.
- 저작권자로부터 별도의 허가를 받으면 이러한 조건들은 적용되지 않습니다.

저작권법에 따른 이용자의 권리는 위의 내용에 의하여 영향을 받지 않습니다.

이것은 [이용허락규약\(Legal Code\)](#)을 이해하기 쉽게 요약한 것입니다.

[Disclaimer](#)

이학박사 학위논문

폴리 3-헥실싸이오펜을 함유하고 있는 나노구조체의  
합성과 분광학적 특성분석

Fabrication and Spectroscopic Study of Nanostructured  
Materials Containing Poly(3-hexylthiophene)

2016 년 2 월

서울대학교 대학원  
화학과 물리화학 전공  
이 동 기

A Ph. D. Dissertation

Fabrication and Spectroscopic Study of Nanostructured  
Materials Containing Poly(3-hexylthiophene)

By Dongki Lee

Supervisor: Professor Du-Jeon Jang

Major: Physical Chemistry

Department of Chemistry

Graduate School of Seoul National University

February 2016

## **Abstract of Dissertation**

Excited-state dynamics of nanostructured materials containing regioregular poly(3-hexylthiophene) (P3HT) has been investigated by using static and time-resolved optical spectroscopy. A brief overview on synthetic methods and optical properties of P3HT and device applications of hybrid nanostructured materials containing P3HT is presented in Chapter 1.

Chapter 2 describes the effect of gold nanoparticles (NPs) on excited-state dynamics of P3HT. P3HT-coated gold (Au@P3HT) hybrid NPs have been prepared via a “grafting-to” approach, and compared with pristine P3HT to investigate the dynamics of exciton relaxation using time-resolved transient-absorption and fluorescence spectroscopy. In efforts to facilitate the efficient dissociation of photo-generated excitons, we have incorporated gold nanoparticles having surface-plasmon resonances into thiol-terminated P3HT to fabricate Au@P3HT nanocomposites. The first-excited singlet state of Au@P3HT decays faster than that of pristine P3HT due to interactions with surface-plasmon resonances; excitons undergo dissociation via energy transfer from P3HT to the surface-plasmon state of a gold nanoparticle in Au@P3HT nanocomposites. The lowest triplet state of P3HT is also less populated due to the energy transfer while its lifetime is slightly reduced by the presence of gold nanoparticles. Thus, it is suggested that our incorporation of gold nanoparticles into P3HT reduces the recombination of geminate excitons and, thereby, increases the probability of exciton dissociation.

Chapter 3 describes effects of gold nanorods (Au NRs) on excited-state

dynamics and photovoltaic performances of hybrid nanocomposites containing P3HT. P3HT-stabilized Au NRs (Au-NR@P3HT nanocomposites) have been facilely fabricated by incubating Au NRs with thiol-terminated P3HT. The  $S_1$  decay of Au-NR@P3HT nanocomposites is found to be slower than that of pristine P3HT, suggesting that the stretched-strand conformation of P3HT chains attached to Au NRs makes structural relaxation more difficult. The amplitude of  $T_1$  absorption is much smaller in Au-NR@P3HT nanocomposites than in pristine P3HT, indicating that the intersystem crossing of  $S_1$  excitons into  $T_1$  excitons does not occur efficiently in Au-NR@P3HT nanocomposites due to the nonflexible character of aggregated P3HT chains. From the comparison of the performances of organic photovoltaic devices, we have found that the device with the 3% embedding of Au-NR@P3HT nanocomposites into the P3HT matrix of the active layer shows significantly improved photovoltaic performances (27% enhancement in the power conversion efficiency), suggesting that the surface-plasmon resonances of Au NRs enhance the dissociation as well as the generation of excitons highly.

Chapter 4 describes the coupling-type dependent excited-state of P3HT NFs, such as J-aggregates and H-aggregates. Thin nanofibers (NFs) of J-dominant aggregates and thick NFs of H-dominant aggregates have been fabricated by self-assembling P3HT-coated Au NPs. With increasing excitation energy, the fraction of the fast emission decay component has been found to decrease, suggesting that the fast formation of polaron pairs, localized, and delocalized polarons results from higher singlet exciton states. In both NFs, whereas triplet ( $T_1$ ) excitons have been hardly observed with excitation at 532 nm, they have been observed with excitation

at 355 nm, revealing that  $T_1$  excitons within NFs are mainly generated through the singlet fission from a higher singlet exciton state rather than through intersystem crossing.

Chapter 5 describes excited-state dynamics of amphiphilic diblock-copolymer self-assembled in mixed selective solvents. An amphiphilic diblock-copolymer consisting of P3HT and poly(4-vinylpyridine) has been synthesized and self-assembled from mixed selective solvents of tetrahydrofuran and methanol to produce nanostructures having photoluminescence spanning from the blue to the red. The emission decay times of the nanostructures have been found to increase with the fraction of methanol, suggesting that the probability of the nongeminate recombination of relaxed  $S_1$  excitons decreases with the increase of medium polarity. The emission decay times are shorter at 690 nm than at 650 nm, indicating that two-dimensional interchain effect is more important for the 0-1 vibronic transition than for the 0-0 transition. The initial intensity percentage of the fast component of biphasic emission decay is much larger with excitation at 532 than with excitation at 355 nm, suggesting that other charge carriers such as polarons are generated rapidly from  $S_1$  excitons in competition with vibrational relaxation.

*Keywords:* excited-state, nanocomposites, nanofibers, P3HT, self-assembly, surface-plasmon resonance, time-resolved spectroscopy.

*Student Number:* 2011-30101

# **Table of Contents**

## **Abstract of Dissertation**

## **List of Figures and Tables**

### **Chapter 1. General Introduction**

1. 1. Synthetic Methods of Poly(3-hexylthiophene) (P3HT)
1. 2. Optical Properties of P3HT
1. 3. Applications of Nanostructured Materials Consisting of P3HT
1. 4. References

### **Chapter 2. Charge-Carrier Relaxation Dynamics of P3HT-Coated Gold Nanoparticles**

2. 1. Abstract
2. 2. Introduction
2. 3. Experimental Section
2. 4. Results and Discussion
2. 5. Conclusions
2. 6. Acknowledgements
2. 7. References
2. 8. Supporting Information

### **Chapter 3. Effects of Gold Nanorods on the Excited-State Dynamics and Photovoltaic Performances of Hybrid Nanocomposites Containing P3HT**

3. 1. Abstract
3. 2. Introduction
3. 3. Experimental Section
3. 4. Results and Discussion
3. 5. Conclusions
3. 6. Acknowledgements
3. 7. References
3. 8. Supporting Information

## **Chapter 4. Formation and Decay of Charge Carriers in Aggregated Nanofibers Consisting P3HT-Coated Gold Nanoparticles**

- 4. 1. Abstract
- 4. 2. Introduction
- 4. 3. Experimental Section
- 4. 4. Results and Discussion
- 4. 5. Conclusions
- 4. 6. Acknowledgements
- 4. 5. References
- 4. 6. Supporting Information

## **Chapter 5. Excited-State Dynamics of an Amphiphilic Diblock Copolymer Self-Assembled from Mixed Solvents**

- 5. 1. Abstract
- 5. 2. Introduction
- 5. 3. Experimental Section
- 5. 4. Results and Discussion
- 5. 5. Conclusions
- 5. 6. Acknowledgements
- 5. 5. References
- 5. 6. Supporting Information

## **Appendix**

- A.1. List of Publications
- A.2. List of Presentations
  - A.2.1. International Presentations
  - A.2.2. Domestic Presentations

## **Abstract (Korean)**

## List of Figures, Schemes, and Tables

**Figure 1-1.** Structural diagrams for polythiophene and the alkylthiophene derivatives: (a) chemical structure of polythiophene; (b) the two valence-bond configurations are not equivalent; (c) chemical structure of the soluble and processible poly(3-alkylthienylenes) -the P3AT's.

**Figure 1-2.** Excited-state self-trapping (1→2) and ground-state torsional relaxation (3→4) are depicted for a tetramer segment of P3HT.

**Figure 2-1.** Schematic for the synthesis of a Au@P3HT nanocomposite.

**Figure 2-2.** TEM images of P3HT (a) and Au@P3HT (b,c) and HRTEM image of Au@P3HT (d).

**Figure 2-3.** EDX elemental intensity profiles of Au@P3HT scanned along the line in the HRTEM image of the inset.

**Figure 2-4.** HRXRD patterns of the dropcoated films of P3HT and Au@P3HT before and after thermal annealing at 220 °C for 30 min.

**Figure 2-5.** DSC curves of P3HT (dotted) and Au@P3HT (solid) measured at a heating or cooling rate of 10 °C min<sup>-1</sup>.

**Figure 2-6.** Peak-normalized absorption (a) and emission (b) spectra of P3HT (dotted) and Au@P3HT (solid) in chloroform (left) and films on quartz plates (right).

**Figure 2-7.** Femtosecond time-resolved transient-absorption kinetic profiles of P3HT and Au@P3HT in chloroform. Samples were excited at 400 nm and monitored at 400 nm, and solid lines are the best-fitted curves to extract kinetic constants.

**Table 2-1.** Transient-Absorption and Fluorescence Kinetic Constants of P3HT and Au@P3HT in Chloroform.

**Figure 2-8.** Picosecond time-resolved fluorescence kinetic profiles of P3HT and Au@P3HT in chloroform. Samples were excited at 355 nm and monitored at 580 nm, and solid lines are the best-fitted curves to extract kinetic constants.

**Figure 2-9.** Nanosecond time-resolved transient-absorption kinetic profiles of P3HT and Au@P3HT in chloroform. Samples were excited at 355 nm and monitored at 820 nm. Solid lines are the best-fitted curves to extract time constants.

**Figure S2-1.**  $^1\text{H}$  NMR spectrum (500 MHz,  $\text{CDCl}_3$ ) of allyl-terminated P3HT.

**Figure S2-2.** MALDI-TOF mass spectrum of allyl-terminated P3HT.

**Figure S2-3.** Schematic for the synthesis of a Au@P3HT nanocomposite.

**Figure S2-4.** TGA curves (a) and TGA derivative curves (b) of P3HT (dotted) and Au@P3HT (solid).

**Table S2-1.** XRD Values of the Dropcoated Films of P3HT and Au@P3HT.

**Figure S2-5.** Schematic structures of P3HT (a) and Au@P3HT (b).

**Table S2-2.** Photophysical Properties of P3HT and Au@P3HT.

**Scheme 3-1.** Fabrication of P3HT-stabilized gold nanorods (Au-NR@P3HT nanocomposites).

**Figure 3-1.** TEM images of Au-NS@P3HT (a) and Au-NR@P3HT nanocomposites (b).

**Figure 3-2.** XPS spectra of P3HT-SH (a) and Au-NR@P3HT nanocomposites (b). Violet curves represent the sum of fitted curves.

**Table 3-1.** Binding Energies in eV for the Deconvoluted Curves of S 2p XPS Spectra.

**Figure 3-3.** Absorption spectra of pristine P3HT in THF (red), Au-NS@P3HT nanocomposites in THF (green), Au-NR@P3HT nanocomposites in THF (blue), and CTAB-stabilized Au NRs in water (orange).

**Figure 3-4.** Difference absorption spectrum in the range of 450 nm to 670 nm (black circles) obtained by subtracting the red curve of pristine P3HT from the blue curve of Au-NR@P3HT nanocomposites in Figure 3, fitted with four Gaussian curves of  $\lambda_1$  (blue),  $\lambda_2$  (green),  $\lambda_3$  (orange), and  $\lambda_4$  (red); the violet curve represents the sum of four fitted curves.

**Table 3-2.** Spectral Positions of Four Gaussian Curves Fitted to Subtracted Absorption Spectrum of Figure 3-4

**Figure 3-5.** Emission spectra of pristine P3HT (red), Au-NS@P3HT nanocomposites (green), and Au-NR@P3HT nanocomposites (blue) dispersed in THF, with excitation at 355 nm (a) and 532 nm (b).

**Figure 3-6.** Emission kinetic profiles of pristine P3HT (red) and Au-NR@P3HT nanocomposites (green) dissolved in THF, monitored at 580 nm after excitation at 355 nm. Solid lines are best-fitted curves to extract kinetic constants.

**Table 3-3.** Emission and Transient-Absorption Kinetic Constants of Pristine P3HT and Au-NR@P3HT Nanocomposites in THF.

**Figure 3-7.** Nanosecond transient-absorption kinetic profiles of pristine P3HT (red) and Au-NR@P3HT nanocomposites (green) dissolved in THF, probed at 820 nm after excitation at 355 nm. Solid lines are best-fitted curves to extract kinetic constants.

**Figure 3-8.**  $J-V$  curves of P3HT/PCBM photovoltaic devices with different additives in the active layer.

**Table 3-4.** Photovoltaic Operation Parameters of P3HT/PCBM Devices with Different Additives in the Active Layer.

**Figure S3-1.** TEM image of Au NRs.

**Figure S3-2.** Difference absorption spectrum obtained by subtracting the red curve of pristine P3HT from the blue curve of Au-NR@P3HT nanocomposites in Figure 3-3.

**Scheme 4-1.** Schematic for the fabrication of Au@P3HT NFs.

**Scheme 4-2.** Schematic representation for the dynamics of singlet ( $S_1$ ) and triplet excitons ( $T_1$ ), triplet pairs (TT), localized (LP) and delocalized polarons (DP), polaron pairs (PP) in thick (thin) Au@P3HT NFs, where time constants are indicated in the units of ps. Key: <sup>a</sup> singlet fusion, <sup>b</sup> vibrational relaxation, <sup>c</sup> PP

formation, <sup>d</sup>P or DP formation, <sup>e</sup> geminate recombination to S<sub>1</sub>, <sup>f</sup> singlet fission, <sup>g</sup> triplet fusion, <sup>h</sup>T<sub>1</sub> formation, and <sup>i</sup> intersystem crossing.

**Figure 4-1.** TEM (left) and SEM images (right) of thin (top) and thick NFs (bottom).

**Figure 4-2.** Absorption (a) and emission spectra (b) of non-aggregate Au@P3HT NPs in chloroform (blue), thin NFs in cyclohexanone (green), and thick NFs in cyclohexanone (red). Samples were excited at 355 nm for the emission spectra.

**Figure 4-3.** Emission spectra (black) of thin (a) and thick NFs (b) in cyclohexanone with excitation at 355 nm, fitted with three Gaussian curves  $\lambda_1$  (blue),  $\lambda_2$  (green), and  $\lambda_3$  (red); violet curves represent the sum of the three fitted curves.

**Figure 4-4.** Emission spectra of thick NFs (b) in cyclohexanone with excitation at 355 (blue) and 532 nm (red).

**Table 4-1.** Three Gaussian Curves Fitted to Each Emission Spectrum of NFs Dispersed in Cyclohexanone.

**Figure 4-5.** Emission kinetic profiles of thick NFs excited at 355 nm and monitored at 580 (blue), 650 (green), and 690 nm (red) (a), thin (green) and thick NFs (red) excited at 355 nm and monitored at 650 nm (b), and thick NFs excited at 355 (blue)

and 532 nm (green) and monitored at 650 nm (c). NFs were dispersed in cyclohexanone, and solid lines are best-fitted curves to extract kinetic constants.

**Table 4-2.** Emission Decay Kinetic Constants of NFs Dispersed in Cyclohexanone.

**Figure 4-6.** Picosecond transient-absorption kinetic profiles of thin NFs (green) and thick NFs (red) excited at 355 nm and probed at 660 (a), 740 (b), and 1000 nm (c). NFs were dispersed in cyclohexanone, and solid lines are best-fitted curves to extract kinetic constants.

**Table 4-3.** Transient-Absorption Kinetic Constants of NFs Dispersed in Cyclohexanone with Excitation at 355 nm.

**Figure 4-7.** Picosecond transient-absorption kinetic profiles of pristine NFs (a), thin NFs (b), and thick NFs (c) excited at 355 nm and monitored at 820 (blue) and 1200 nm (red). Green triangles in each panel have been obtained by subtracting red squares from blue circles. Solid lines are best-fitted curves to extract time constants.

**Figure 4-8.** Nanosecond transient-absorption kinetic profiles of pristine NFs (blue), thin NFs (green), and thick NFs (red). Samples were excited at 355 nm and probed at 820 nm. Solid lines are best-fitted curves to extract time constants.

**Figure S4-1.** Proposed formation mechanisms of thin and thick NFs.

**Figure S4-2.** AFM images of thin (left) and thick NFs (right).

**Figure S4-3.** Absorption spectra (circles) of thin (a) and thick NFs (b). While Gaussian-fitted curves 1 (violet) and 2 (blue) are attributed to the  $S_0$ - $S_1$  transition of free chains, curves 3 (green), 4 (yellow), and 5 (red) are attributed to the 0-2, the 0-1, and the 0-0 transitions of aggregated chains, respectively. Black curves represent the sum of the five fitted curves. The exact locations and the absorbance percentages of the five fitted curves are outlined in Table S4-1.

**TABLE S4-1.** Spectral Positions of Five Gaussian Curves Fitted to Each Absorption Spectrum of NFs Dispersed in Cyclohexanone.

**Figure S4-4.** Absorption spectra of pristine NFs (blue), thin NFs (green), and thick NFs (red).

**Figure S4-5.** Emission spectra of pristine NFs (green) and thin NFs (red) in cyclohexanone with excitation at 430 nm.

**Figure S4-6.** Emission spectra (circles) of thin (a) and thick NFs (b) in cyclohexanone with excitation at 532 nm, fitted with three Gaussian curves  $\lambda_1$  (blue),  $\lambda_2$  (green), and  $\lambda_3$  (red); black curves represent the sum of the three fitted curves.

**Figure S4-7.** Picosecond transient-absorption kinetic profiles of thin NFs (green) and thick NFs (red) excited at 355 nm and probed at 660 (a), 740 (b), 820 (c), 1000 (d), and 1200 nm (e) observed in time windows of 50 ps. NFs were dispersed in cyclohexanone, and solid lines are best-fitted curves to extract kinetic constants.

**Table S4-2.** Transient-Absorption Kinetic Constants of NFs Dispersed in Cyclohexanone with Excitation at 355 nm, Observed in Time Windows of 50 ps.

**Scheme 5-1.** Schematic for the fabrication of P3HT-*b*-P4VP nanostructures self-assembled from mixed selective solvents, where the red and the green indicate P3HT and P4VP, respectively.

**Figure 5-1.** TEM image of P3HT-*b*-P4VP nanostructures self-assembled in a mixed solvent of  $R = 1.0$ .

**Figure 5-2.** Absorption spectra of P3HT-*b*-P4VP self-assembled in mixed solvents of indicated  $R$  values (a). Absorption spectra (yellow circles) of P3HT-*b*-P4VP in mixed solvents of  $R = 0.2$  (b) and 5.0 (c); Gaussian curves of  $\lambda_{a1}$  (violet),  $\lambda_{a2}$  (blue),  $\lambda_{a3}$  (green),  $\lambda_{a4}$  (orange), and  $\lambda_{a5}$  (red), whose sums are represented by black curves, have been fitted to the absorption spectra.

**Table 5-1.** Spectral Positions of Gaussian Curves Fitted to Each Absorption Spectrum of P3HT-*b*-P4VP in Solutions of Different  $R$  Values.

**Figure 5-3.** Emission spectra of P3HT-*b*-P4VP self-assembled in mixed solvents of indicated *R* values (a). Emission spectra (yellow circles) of P3HT-*b*-P4VP in mixed solvents of *R* = 0.2 (b) and 5.0 (c) with excitation at 355 nm; Gaussian curves of  $\lambda_{e1}$  (violet),  $\lambda_{e2}$  (blue),  $\lambda_{e3}$  (green),  $\lambda_{e4}$  (orange), and  $\lambda_{e5}$  (red), whose sums are represented by black curves, have been fitted to the emission spectra.

**Table 5-2.** Gaussian Curves Fitted to Each Emission Spectrum of P3HT-*b*-P4VP Self-Assembled from Mixed Solvents of Different *R* Values with Excitation at 355 nm.

**Figure 5-4.** Peak-normalized emission spectra of self-assembled P3HT-*b*-P4VP in mixed solvents of indicated *R* values with excitation at 532 nm.

**Figure 5-5.** Emission kinetic profiles of P3HT-*b*-P4VP in mixed solvents of *R* = 0.2 (red) and 5.0 (blue) excited at 355 nm and monitored at 451 (a), 572 (b), 651 (c), and 691 nm (d). Solid lines are best-fitted curves to extract kinetic constants.

**Table 5-3.** Emission Kinetic Constants of P3HT-*b*-P4VP Self-Assembled in Mixed Solvents of MeOH and THF at various *R* Values.

**Figure 5-6.** Emission kinetic profiles of P3HT-*b*-P4VP in mixed solvents of *R* = 0.2 (red) and 5.0 (blue) excited at 532 nm and monitored at 610+ nm. Solid lines are best-fitted curves to extract kinetic constants.

**Scheme S5-1.** Synthesis of P3HT-*b*-P4VP.

**Figure S5-1.** <sup>1</sup>H NMR spectra (500 MHz, CDCl<sub>3</sub>) of diblock copolymer P3HT-*b*-P4VP (top) and trithiocarbonate-terminated P3HT (bottom).

**Figure S5-2.** Maximum-normalized absorption (a) and emission spectra (b) of P3HT-*b*-P4VP in mixed solvents of indicated *R* values. Samples were excited at 355 nm for the emission spectra.

**Figure S5-3.** Emission spectra (yellow circles) of P3HT-*b*-P4VP in solutions at *R* = 0.2 (a) and 5.0 (b) with excitation at 532 nm. Gaussian curves of  $\lambda_{e3}$  (green),  $\lambda_{e4}$  (orange), and  $\lambda_{e5}$  (red), whose sums are represented by black curves, have been fitted to the emission spectra.

**Table S5-1.** Gaussian Curves Fitted to Each Emission Spectrum of P3HT-*b*-P4VP Self-Assembled from Mixed Solvents of Different *R* Values with Excitation at 532 nm.

## **Chapter 1. General Introduction**

## **1. 1. Synthetic Methods of Poly(3-hexylthiophene) (P3HT)**

Poly(3-alkylthiophenes) (P3ATs) have been extensively studied because of their high environmental stability, good solubility and high electrical conductivity.<sup>1</sup> In particular, regioregular poly(3-hexylthiophene) (RR-P3HT) has received intense attention for applications in optoelectronic devices such as light-emitting diodes, biosensors, and photovoltaic cells because of its facilely tunable optical and electrical properties controlled by regulating the conformation, packing, and morphology of individual chains.<sup>2-4</sup> The substitution of the alkylchain improve the solubility of the polymer and makes P3HT self-assembled into a two-dimensional high-interchain lamella with favorable head-to-head coupling or into a one-dimensional (1D) high-intrachain nanostructure with unfavorable HH coupling, depending on diverse formation conditions.<sup>5,6</sup>

In 1980, unsubstituted polythiophene (PT) was chemically synthesized for the first time by using the 2,5-coupling reaction of 2,5-dibromothiophene monomer.<sup>7</sup> Although the prepared PT has advantages such as a high environmental stability and electrical conductivity, it had a low solubility disadvantage. In 1985, Elsenbaumer et al. were synthesized substituted PT (P3AT).<sup>8</sup> They also used the 2,5-coupling reaction of 2,5-diiodo-3-alkylthiophene monomer. Because random 2,5-coupling reaction of monomer creates multiple head-to-head (HH) and tail-to-tail (TT) couplings, the loss of regioregularity in P3ATs occurred. This causes a steric interaction of substituted alkylchain and an increase of the torsion angles of

polymer backbone. Thus, a loss of  $\pi$ -conjugation of polymer backbone is caused, which leads a decrease of charge transport of P3AT.<sup>1b</sup> To overcome this drawback, in 1992, regioregular P3ATs (RR-P3ATs), were synthesized by McCullough et al. and Rieke et al.<sup>9,10</sup> Especially, McCullough et al. also developed the Grignard metathesis (GRIM) method.<sup>11</sup> This development makes that both cryogenic temperatures and highly reactive metals are unnecessary. Mobilities of RR-P3HT are as high as  $0.2 \text{ cm}^2/(\text{V s})$ , while those of regioirregular P3HT are  $\sim 10^{-5} \text{ cm}^2/(\text{V s})$ .<sup>1b</sup> Recently, the facile synthesis method has been developed to introduce a variety of functional groups in the terminal of P3HT.<sup>12</sup>

## 1. 2. Optical Properties of P3HT

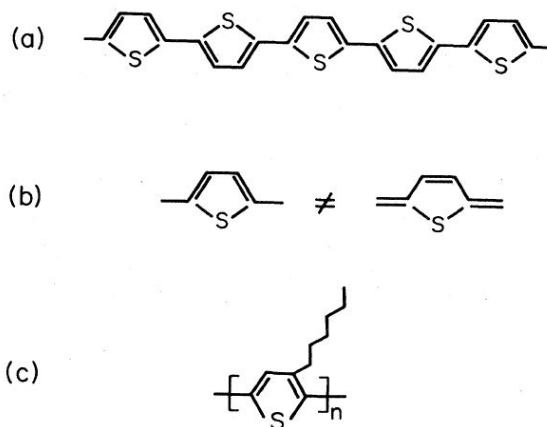


**Figure 1-1.** Structural diagrams for polythiophene and the alkylthiophene derivatives: (a) chemical structure of polythiophene; (b) the two valence-bond configurations are not equivalent; (c) chemical structure of the soluble and processible poly(3-alkylthienylenes)-the P3AT's. Reproduced from ref. 13.

Because polyacetylene is a linear polymer, Polyacetylene has the degenerate ground

state leading to solitons as the important excitations.<sup>13</sup> On the other hand, as shown Figure 1-1, since PT has a nondegenerate ground state related to the nonenergetic equivalence of their two limiting mesomeric forms, aromatic and quinoid, it has a polaron bands in the higher doping level.<sup>13</sup> Since the Decay mechanisms in organic conjugated polymers (CPs) affect the improvement of device efficiency made of CPs a critical impact, the comprehensive investigation and understanding of the fundamental photophysical dynamics of CPs are important research points. The relaxation dynamics of excited states and the decay mechanisms of photoinduced charge carriers for CPs have been investigated extensively by using time-resolved spectroscopy.<sup>14-16</sup> In Figure 1-2, excited-state self-trapping and ground-state torsional relaxation of tetramer segment of P3HT are well represented schematically.<sup>17</sup>

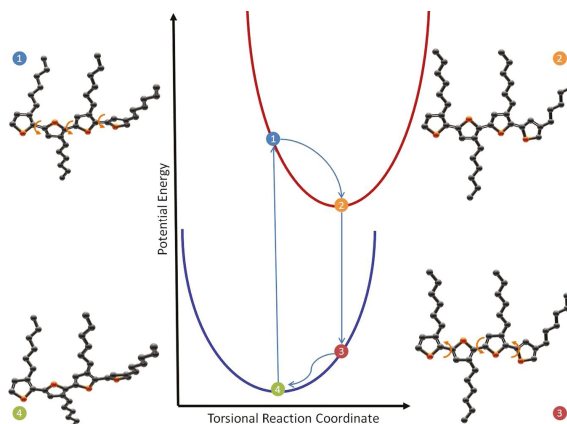


**Figure 1-2.** Excited-state self-trapping (1→2) and ground-state torsional relaxation (3→4) are depicted for a tetramer segment of P3HT. Reproduced from ref. 17.

Upon photoexcitation, the self trapping of excitons (~100 fs), vibrational relaxation

processes, the downhill relaxation of self-trapped excitons ( $\sim 1$  ps), torsional relaxation (3-10 ps), and intrachain/interchain excitation energy transfer are occurred in the excited-state of P3HT.<sup>17</sup> Heeger et al. reported that energy migration processes in pristine P3HT, polymer/fullerene blend system, and fullerene attached to P3HT system have been widely investigated.<sup>18,19</sup> Xie et al. reported a femtosecond time-resolved fluorescence study of a RR-P3HT in solution and in blend films made of P3HT/PCBM, suggesting that the interchain and intrachain interaction could be a more competitive process than the exciton-exciton annihilation.<sup>20</sup>

In practice, since aggregate P3HT systems such as film and nanofibers (NFs) have been used in diverse optoelectronic application fields, spectroscopic studies on aggregate P3HT systems are the most important research point in the excited-state dynamics of P3HT. Guo et al. reported the comprehensive investigation on the formation and decay dynamics of triplet ( $T_1$ ) excitons and polarons to depend on the regioregularity of P3HT films.<sup>14</sup> Singlet ( $S_1$ ) excitons are more delocalized to form interchain excitons due to the strong interchain interactions in RR-P3HT films, on the other hand,  $S_1$  excitons generated from the amorphous structure of regiorandom P3HT films are substantially converted to  $T_1$  excitons through the singlet fission.<sup>14</sup> Grey et al. have investigated the formation of  $T_1$  excitons in J-aggregate NFs.<sup>21</sup> They suggest that  $T_1$  excitons can be formed via a recombination of long-lived polarons in J-aggregate NFs having high intrachain order. High intrachain order in J-aggregate P3HT NFs facilitates the delocalization of  $S_1$  excitons, leading to the eventual formation of  $T_1$  excitons via the nongeminate recombination of delocalized polaron

species.<sup>21</sup>

### **1. 3. Applications of Nanostructured Materials Consisting of P3HT**

As mentioned above, RR-P3HT has a high electrical conductivity due to its characteristic structure. Because of facilely tunable optical and electrical properties of RR-P3HT controlled by regulating the conformation, packing, and morphology of individual chains, RR-P3HT and its nanostructures are popular material to the device applications in electronics and optoelectronics.<sup>22,23</sup> Especially, RR-P3HT can be self-assembled to one-dimensional (1D) nanostructure such as NFs in a poor solvent condition. Since 1D nanostructures of P3HT have good advantages such as large surface areas and 1D path ways at the nanosized level for the migration of charge carriers, they are expected to have improved optoelectronic device performances such as organic field-effect transistors and organic photovoltaic.<sup>6,24</sup> RR-P3HT can be formed thin films with amorphous or polycrystalline morphology in various conditions. Because of the prospect for greater control of their spatial organization, crystallinity, and overall morphology, RR-P3HT and its nanostructures expected to offer approaches to improve current optical devices and the design of optoelectronic devices of next-generation.

### **1. 4. References**

- (1) (a) McCullough, R. D. *Adv. Mater.* **1998**, *10*, 93-116. (b) Osaka, I.; McCullough, R. D. *Acc. Chem. Res.* **2008**, *41*, 1202-1214.

- (2) Park, S.-J.; Kang, S.-G.; Fryd, M.; Saven, J. G.; Park, S.-J. *J. Am. Chem. Soc.* **2010**, *132*, 9931-9933.
- (3) Gilroy, J. B.; Lunn, D. J.; Patra, S. K.; Whittell, G. R.; Winnik, M. A.; Manners, I. *Macromolecules* **2012**, *45*, 5806-5815.
- (4) Palaniappan, K.; Hundt, N.; Sista, P; Nguyen, H; Hao, J.; Bhatt, M. P.; Han, Y.-Y.; Schmiedel, E. A.; Sheina, E. E.; Biewer, M. C.; et al. *J. Polym. Sci., Part A: Polym. Chem.* **2011**, *49*, 1802-1808.
- (5) Choi, S. Y.; Lee, J. U.; Lee, J. W.; Lee, S.; Song, Y. J.; Jo, W. H.; Kim, S. H. *Macromolecules* **2011**, *44*, 1771-1774.
- (6) Kim, F. S.; Jenekhe, S. A. *Macromolecules* **2012**, *45*, 7514-7519.
- (7) Yamamoto, T.; Sanechika, K.; Yamamoto, A., *J. Polym. Sci., Polym Lett. Ed.* **1980**, *18*, 9-12.
- (8) Elsenbaumer, R.; Jen, K. Y.; Oboodi, R., *Polym. Mater. Sci. Eng.* **1985**, *53*, 79.
- (9) McCullough, R. D.; Lowe, R. D. *J. Chem. Soc., Chem. Commun.* **1992**, 70-72.
- (10) Chen, T. A.; Rieke, R. D. *J. Am. Chem. Soc.* **1992**, *114*, 10087-10088.
- (11) Loewe, R. S.; Khersonsky, S. M.; McCullough, R. D. *Adv. Mater.* **1999**, *11*, 250-253.
- (12) Iovu, M. C.; Sheina, E. E.; Gil, R. R.; McCullough, R. D. *Macromolecules* **2005**, *38*, 8649-8656.
- (13) Heeger, A. J.; Kivelson, S.; Schrieffer, J.; Su, W.-P. *Rev. Mod. Phys.* **1988**, *60*, 781.

- (14) (a) Guo, J.; Ohkita, H.; Bente, H.; Ito, S. *J. Am. Chem. Soc.* **2010**, *132*, 6154-6164. (b) Guo, J.; Ohkita, H.; Bente, H.; Ito, S. *J. Am. Chem. Soc.* **2009**, *131*, 16869-16880.
- (15) Xie, Y.; Li, Y.; Xiao, L. X.; Qiao, Q. Q.; Dhakal, R.; Zhang, Z. L.; Gong, Q. H.; Galipeau, D.; Yan, X. Z. *J. Phys. Chem. C* **2010**, *114*, 14590-14600.
- (16) Ferreira, B.; da Silva, P. F.; Seixas de Melo, J. S.; Pina, J.; Maçanita, A. J. *Phys. Chem. B* **2012**, *116*, 2347-2355.
- (17) Busby, E.; Carroll, E. C.; Chinn, E. M.; Chang, L.; Moulé, A. J.; Larsen, D. S. *J. Phys. Chem. Lett.* **2011**, *2*, 2764-2769.
- (18) Hwang, I. W.; Moses, D.; Heeger, A. J. *J. Phys. Chem. C* **2008**, *112*, 4350-4354.
- (19) (a) Banerji, N.; Cowan, S.; Vauthey, E.; Heeger, A. J. *J. Phys. Chem. C* **2011**, *115*, 9726-9739. (b) Banerji, N.; Seifert, J.; Wang, M.; Vauthey, E.; Wudl, F.; Heeger, A. J. *Phys. Rev. B* **2011**, *84*, 075206.
- (20) Xie, Y.; Li, Y.; Xiao, L.; Qiao, Q.; Dhakal, R.; Zhang, Z.; Gong, Q.; Galipeau, D.; Yan, X. *J. Phys. Chem. C* **2010**, *114*, 14590-14600.
- (21) Thomas, A. K.; Garcia, J. A.; Ulibarri-Sanchez, J.; Gao, J.; Grey, J. K. *ACS Nano* **2014**, *8*, 10559-10568.
- (22) Park, D. H.; Kim, M. S.; Joo, J. *Chem. Soc. Rev.* **2010**, *39*, 2439-2452.
- (23) Reiss, P.; Couderc, E.; De Girolamo, J.; Pron, A. *Nanoscale* **2011**, *3*, 446-489.
- (24) Kim, J. S.; Lee, J. H.; Park, J. H.; Shim, C.; Sim, M.; Cho, K. *Adv. Funct. Mater.* **2011**, *21*, 480-486.

## **Chapter 2. Charge-Carrier Relaxation Dynamics of P3HT-Coated Gold Hybrid Nanoparticles†**

†This is reproduced from Dongki Lee and Du-Jeon Jang, *polymer*, **2014**, *55*, 5469.

© 2014 Elsevier Ltd.

## 2. 1. Abstract

P3HT-coated gold (Au@P3HT) hybrid NPs have been prepared via a “grafting-to” approach, and compared with pristine P3HT to investigate the dynamics of exciton relaxation using time-resolved transient-absorption and fluorescence spectroscopy. In efforts to facilitate the efficient dissociation of photo-generated excitons, we have incorporated gold nanoparticles having surface-plasmon resonances into thiol-terminated P3HT to fabricate Au@P3HT nanocomposites. The first-excited singlet state of Au@P3HT decays faster than that of pristine P3HT due to interactions with surface-plasmon resonances; excitons undergo dissociation via energy transfer from P3HT to the surface-plasmon state of a gold nanoparticle in Au@P3HT nanocomposites. The lowest triplet state of P3HT is also less populated due to the energy transfer while its lifetime is slightly reduced by the presence of gold nanoparticles. Thus, it is suggested that our incorporation of gold nanoparticles into P3HT reduces the recombination of geminate excitons and, thereby, increases the probability of exciton dissociation.

## 2. 2. Introduction

The design and controlled fabrication of nanostructured materials having functional properties have been extensively studied.<sup>1-4</sup> In particular, hybrid nanocomposites of conjugated polymers and inorganic nanocrystals have received intense attention for applications in optoelectronic devices such as light-emitting diodes, biosensors, and photovoltaic cells.<sup>5-7</sup> Organic solar cells containing active layers based on conjugated polymers have been widely explored due to their low device-fabrication cost, solution-process ability, light weight, and flexibility.<sup>8-11</sup> In spite of these important advantages, they have not been commercialized well due to their low power- conversion efficiency.<sup>12,13</sup> Thus, in order to overcome this low-efficiency problem, diverse research groups have focused on the synthesis of low band-gap conjugated polymers,<sup>17-19</sup> the enhancement of the functionality of conjugated polymers,<sup>20,21</sup> the development of a variety of device-fabrication processes,<sup>22,23</sup> and the preparation of hybrid nanocomposites composed of inorganic nanocrystals and organic conjugated polymers for use in active layer materials.<sup>24-27</sup>

Hybrid nanocomposites can provide diverse opportunities for the development of novel nanomaterials having improved physical and chemical properties against single-component counterparts.<sup>24,28-30</sup> The presence of an interface within a hybrid nanocomposite containing inorganic nanocrystals such as Au, Ag, CdSe, and TiO<sub>2</sub> and conjugated polymers such as poly(3-hexylthiophene) (P3HT) and alkoxy-substituted poly(phenylenevinylenes) may promote charge transfer and charge separation.<sup>27-29,31,32</sup> Moreover, organic conjugated-polymer shells can protect

unstable inorganic nanocrystal cores from chemical poisoning, corrosion, and dissolution, as inorganic nanocrystals alone tend to react or aggregate because of their poor stability in a medium. Among inorganic nanocrystals, in particular, nanoclusters and colloids of noble metals show strong absorption bands in the visible region due to the surface-plasmon oscillation modes of their conduction electrons. Thus, the optical properties of silver and gold nanoparticles (NPs) have received considerable attention.<sup>33-35</sup> Since the enhancement of power-conversion efficiency in organic solar cells is an important challenge, the comprehensive investigation and understanding of the fundamental photophysical dynamics of conjugated polymers such as P3HT, most commonly used in the active layer of an organic solar-cell device, are critical research points for the development of new materials used for the active layer. The relaxation dynamics of excited states and the decay mechanisms of photoinduced charge carriers for conjugated polymers have been investigated extensively by using time-resolved spectroscopy.<sup>36-43</sup> In particular, the efficient dissociation and transfer of excitons photo-generated from P3HT have a lot of influence on the overall efficiency of organic solar-cell devices. To improve these processes within an active layer, we have introduced a gold NP having surface-plasmon resonances (SPRs), which exhibit intense light absorption in the visible region, in a P3HT matrix to fabricate a P3HT-coated gold (Au@P3HT) nanocomposite. Since the SPR band of a Au NP is spectrally similar to the absorption band of P3HT, we anticipate that the degree of light absorption will be enhanced in the nanocomposite.<sup>35</sup> In order to maximize the dissociation and transfer of the photo-generated excitons of P3HT, it is necessary to disperse gold NPs

homogeneously at the molecular level through the P3HT matrix of the nanocomposites via chemical-bond interactions and to find optimum conditions for the dissociation of photo-generated excitons.

In this paper, we present that a Au@P3HT nanocomposite has been synthesized via a “grafting-to” approach with thiol-terminated P3HT (P3HT-SH) and  $\text{HAuCl}_4$  (Figure 2-1). Since the well dispersion of inorganic gold NPs within a P3HT matrix is important for the efficient interactions of gold NPs with P3HT, we have incorporated inorganic gold NPs by reducing a gold precursor directly in P3HT-SH so that a well-dispersed homogeneous system of organic and inorganic phases at the molecular level has been achieved. The dynamics of charge-carrier relaxation in Au@P3HT nanocomposites has also been investigated in comparison with that in pristine P3HT using time-resolved transient-absorption and fluorescence spectroscopy, revealing that our incorporation of gold NPs into P3HT reduces the recombination of geminate excitons to increase the probability of exciton dissociation.

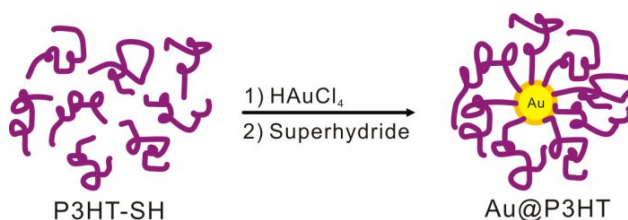


**Figure 2-1.** Schematic for the synthesis of a Au@P3HT nanocomposite.

## 2. 3. Experimental Section

**2. 3. 1. Materials.**  $\text{HAuCl}_4 \cdot 3\text{H}_2\text{O}$  (s, 99.9%), lithium triethylborohydride (0.1 M in THF), 2,5-dibromo-3-hexylthiophene (l, 97%), tert-butylmagnesium chloride (1.0 M in THF), [1,3-bis(diphenylphosphino)propane]dichloronickel(II)(s), allyl magnesium bromide (1.0 M in diethyl ether), 9-borabicyclo[3.3.1]nonane (0.5 M in THF), triphenylphosphine (s, 99%), diisopropyl azodicarboxylate (l, 95%), thioacetic acid (l, 96%), lithium aluminum hydride (1.0 M in THF), *o*-dichlorobenzene (l, 99%),  $\text{CHCl}_3$  (l,  $\geq 99\%$ ), and  $\text{CDCl}_3$  (l, 99.8 atom% D, contains 0.03 v/v% TMS and 0.5% silver foil as a stabilizer) were used as purchased from Sigma-Aldrich without further purification. Sodium hydroxide (s,  $\geq 98.0\%$ ) and methanol (l,  $\geq 99.5\%$ ) was used as purchased from Daejung Chemicals & Metals, and hydrogen peroxide (34% in water) was used as purchased from Samchun Pure Chemicals. Tetrahydrofuran (THF, l,  $\geq 99\%$ ) purchased from Daejung Chemicals & Metals was stirred over sodium and benzophenone with mild refluxing for 24 h, distilled into a round-bottom flask with a vacuum stopcock, and followed by three freeze-pump-thaw cycles on a Schlenk line with liquid nitrogen.

**2. 3. 2. Syntheses.** Allyl-terminated P3HT ( $M_n = 10,322 \text{ g mol}^{-1}$ , PDI = 1.07, MALDI-MS  $m/z = 7268.0$ ; Figures S2-1 and S2-2 in the Supporting Information) was synthesized in a 99.999% argon glove box according to the Grignard metathesis reaction,<sup>14</sup> and P3HT-SH ( $M_n = 10,565 \text{ g mol}^{-1}$ , PDI = 1.26, MALDI-MS  $m/z = 6,875.3$ ) was synthesized as previously described.<sup>15</sup> P3HT-functionalized gold (Au@P3HT) nanoparticles were synthesized in a 99.999% argon glove box at room

temperature via a “grafting-to” approach, as described in detail elsewhere.<sup>16</sup> 4.0 mg of H<sub>2</sub>AuCl<sub>4</sub>·3H<sub>2</sub>O and 20 mL of THF were placed in a 150 mL three-neck reaction vessel and 0.10 g P3HT-SH was solubilized in 34 mL of THF, which was added to the vessel. Then, the reaction mixture was magnetically stirred to reach a homogeneous solution in the dark. For the reduction of H<sub>2</sub>AuCl<sub>4</sub>, 1.0 mL of 1.0 M lithium triethylborohydride in THF was added to the flask at once. The homogeneously mixed solution was stirred for 24 h in the dark and then poured into 600 mL of methanol to precipitate produced Au@P3HT nanocomposites, which were filtered into an extraction thimble and purified by Soxhlet extraction with methanol. The Au@P3HT nanocomposites were then dried under vacuum for 24 h at 40 °C. For the preparation of a film sample, 1.0% P3HT or Au@P3HT in chloroform was filtered with a 0.45 μm PTFE filter and spincoated on a 250 mm<sup>2</sup> quartz plate at 3000 rpm for 30 s and then dried in an argon glovebox at room temperature. 4.0 g L<sup>-1</sup> P3HT or Au@P3HT in chloroform was also filtered with a 0.45 μm PTFE filter and dropcast onto a 250 mm<sup>2</sup> quartz plate in an argon glovebox. After being annealed in a vacuum oven at 220 °C for 30 min, the dropcoated film on a quartz plate was kept in the vacuum oven at 30 °C for 24 h.

**2.3.3. Characterization.** <sup>1</sup>H NMR spectra were acquired in CDCl<sub>3</sub> using a 500 MHz Varian/Oxford As-500 spectrometer. Size-exclusion chromatography was performed using a Waters system (1515 pump, 2414 refractive index detector) and a Shodex GPC LF-804 column. Matrix-assisted laser desorption ionization time-of-flight (MALDI-TOF) mass spectra were recorded using an Applied Biosystems Voyager-DE STR biospectrometry workstation. Thermogravimetry analysis (TGA)

was carried out with a TA TGA Q50 instrument under nitrogen atmosphere using 10 mg of a sample at a scan rate of 10 °C min<sup>-1</sup>. Differential scanning calorimetry (DSC) was carried out with a Perkin Elmer DSC 7 under nitrogen atmosphere from 30 °C to 250 °C at a heating or cooling rate of 10 °C min<sup>-1</sup>. While transmission electron microscopy (TEM) images were obtained with a JEOL JEM-2000 microscope, energy-dispersive X-ray (EDX) elemental intensity profiles and high-resolution TEM (HRTEM) images were measured with a JEOL JEM-3000F microscope. High-resolution X-ray diffraction (HRXRD) patterns were recorded with a Bruker D8 DISCOVER diffractometer using Cu K $\alpha$  radiation (0.15418 nm). A dried dropcoated sample was mounted on an aluminum sample holder, and the scanning angle was varied from 3° to 40° at a scanning rate of 5° min<sup>-1</sup>. While absorption spectra were measured with a Scinco S3100 UV/vis spectrophotometer, photoluminescence spectra were detected using a Princeton Instruments ICCD576G CCD attached to a 0.5 m Acton Research SpectraPro-500 spectrometer with excitation of 355 nm pulses from a Q-switched Quantel Brilliant Nd: YAG laser of 6 ns.

**2. 3. 4. Transient-Absorption and Fluorescence Kinetic Profiles.** For the measurement of a femtosecond time-resolved single-color transient-absorption kinetic profile, the fundamental output (800 nm, 50 fs, 1 kHz) of a femtosecond Coherent Libra regenerative amplifier was frequency-doubled with a  $\beta$ -Ba<sub>2</sub>BO<sub>4</sub> crystal to generate the transient-absorption light source. The frequency-doubled beam of 400 nm was split by a beam splitter into two parts, which were used as a pump and a probe. Both the pump and the probe beams were focused with a lens

having a focal length of 10 cm onto the sample and then only the probe was detected using a Si photodiode with the pump blocked. For phase-sensitive detection, the pump beam was modulated by a chopper synchronized with the regenerative amplifier and the modulated probe signal was then recorded with a lock-in amplifier. The polarizations of the pump and the probe were vertical.

Nanosecond time-resolved transient-absorption kinetic profiles were obtained by monitoring the beam intensity of a 75 W Acton Research XS 432 Xe lamp after being transmitted through a sample, which was excited with 355 nm pulses having a duration time of 6 ns from a Q-switched Quantel Brilliant Nd:YAG laser. The wavelength of the probe beam was selected using an Acton Research SP-150 monochromator of 0.15 m and a Kratos GM 200 double monochromator of 0.2 m. The probe beam was detected with a Hamamatsu R928 PMT and digitized with a Lecroy Wavepro 950 oscilloscope of 1 GHz. The laser and the oscilloscope were triggered with variable delays using a Stanford Research Systems DG535 pulse/delay generator.

Picosecond time-resolved fluorescence kinetic profiles with excitation of third-harmonic pulses (355 nm) from a mode-locked Quantel YG901-10 Nd:YAG laser of 25 ps were detected using a Hamamatsu C2830 streak camera of 10 ps attached to a Princeton Instruments RTE128H CCD detector. Emission wavelengths were selected using combined band-pass and cutoff filters. Fluorescence and transient-absorption kinetic constants were extracted by fitting measured kinetic profiles to computer-simulated kinetic curves convoluted with instrument temporal response functions.

## 2. 4. Results and discussion

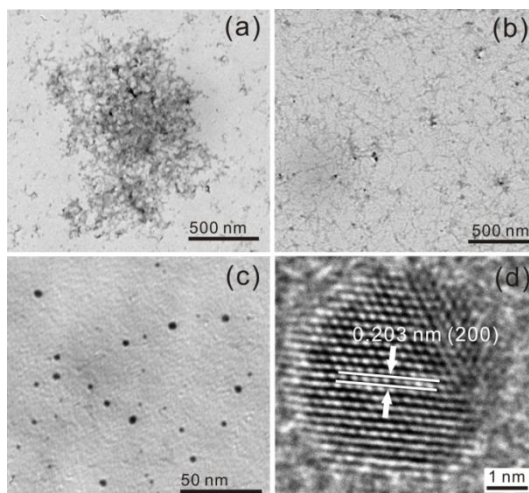


**Figure 2-2.** TEM images of P3HT (a) and Au@P3HT (b,c) and HRTEM image of Au@P3HT (d).

The synthetic procedures of Au@P3HT nanocomposites are shown in Figure S2-3 of the Supporting Information; for the efficient interactions of gold NPs with P3HT, we have incorporated gold NPs directly in P3HT-SH via a ‘grafting-to’ approach. Figure 2-2 shows the TEM images of pristine P3HT and hybrid Au@P3HT prepared by evaporating a droplet of dilute P3HT or Au@P3HT in chloroform on a carbon-coated copper grid. Whereas Figure 2-2a shows that pristine P3HT is nonuniformly aggregated due to attractive interactions of P3HT chains, Figure 2-2b,c reveals that gold NPs are incorporated in P3HT to form Au@P3HT nanocomposites. As gold can bind strongly with thiol molecules, gold NPs formed in P3HT-SH during the ‘grafting-to’ process have been coated with an organic matrix of P3HT via chemical-bond interactions, consequently producing

well-dispersed Au@P3HT nanocomposites having organic and inorganic phases homogeneously at the molecular level. The nanostructural details of a Au@P3HT nanocomposite have been further provided by measuring the HRTEM image of Figure 2-2d; the gold NP is spherical and single-crystalline with a lattice-fringe distance of 0.203 nm, which agrees reasonably well with the literature value (0.2039 nm) of separation between the (200) lattice planes of the fcc gold crystal (JCPDS 04-0784).

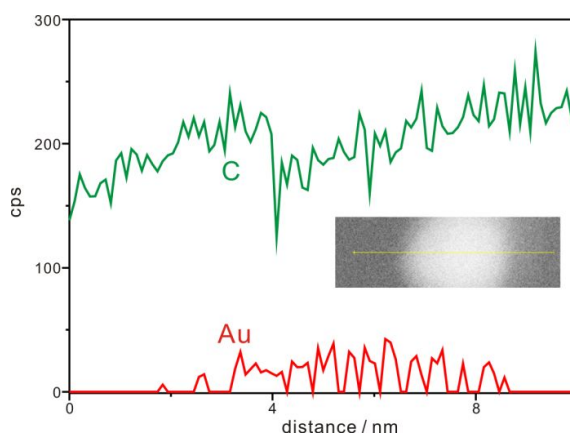


**Figure 2-3.** EDX elemental intensity profiles of Au@P3HT scanned along the line in the HRTEM image of the inset.

The EDX line-scanned intensity profiles of Figure 2-3 designate that the composite nanostructure consists of gold and P3HT indeed, which are located in the core and the shell positions, respectively, of the nanocomposite. This result indicates that the gold NP within a Au@P3HT nanocomposite has been coated with P3HT chains; the thiol group of P3HT-SH binds to the surface of the gold NP via forming a thiolate bond during the ‘grafting-to’ process to cap the gold nanocrystal.

The TGA curves of Figure S2-4a in the Supporting Information have been

measured to quantify the gravimetric ratio of inorganic gold NPs to organic P3HT in Au@P3HT nanocomposites; pristine P3HT and hybrid Au@P3HT show weight losses of 72.6% and 58.4%, respectively, as being heated from 30 °C to 700 °C, implying that the content of inorganic gold NPs in Au@P3HT nanocomposites is 14.2%. The TGA derivative curves of Figure S2-4b also indicate that the decomposition temperature of Au@P3HT nanocomposites (449.8 °C) is higher by 2.7 °C than that of pristine P3HT (447.1 °C). This thermal-stability increase supports that covalent-bond interactions between the thiol groups of P3HT-SH chains and the surfaces of gold NPs exist indeed in Au@P3HT nanocomposites.

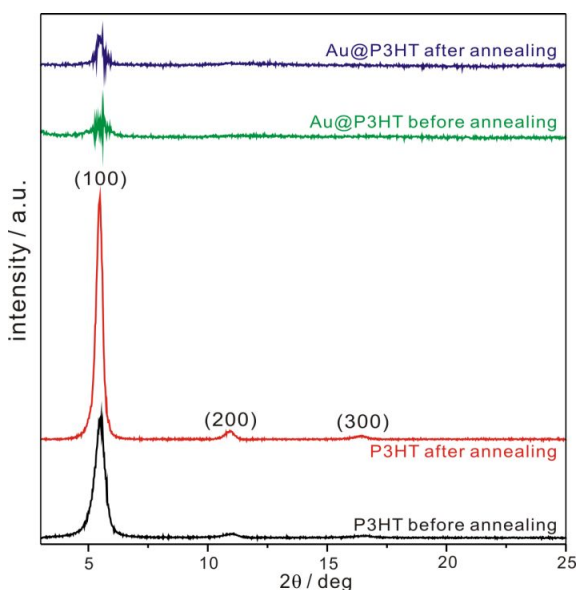


**Figure 2-4.** HRXRD patterns of the dropcoated films of P3HT and Au@P3HT before and after thermal annealing at 220 °C for 30 min.

The HRXRD pattern of a dropcoated pristine P3HT film in Figure 2-4 shows three distinct peaks at  $2\theta = 5.48^\circ$ ,  $10.95^\circ$ , and  $16.48^\circ$ , which have been assigned to

the crystallographic (100), (200), and (300) planes, respectively, of the lamellar structure of P3HT, demonstrating that our pristine P3HT sample has a high degree of crystallinity. The peak at  $2\theta = 5.48^\circ$  corresponds to the  $d$ -spacing value of 1.61 nm, which is known to be the characteristic intrachain distance between P3HT chains in a lamellar packing structure.<sup>44,46b</sup> The  $2\theta$  positions and the intrachain  $d$ -spacing value of our pristine P3HT film are in good agreement with the corresponding literature values.<sup>44b</sup> After thermal annealing, the diffraction peaks retain their positions nearly, but increases its (integrated) intensity by 1.44 times (Table S2-1 in the Supporting Information), indicating that the treatment of thermal annealing has improved the crystallinity of the P3HT film remarkably.

Figure 2-4 also displays that the diffraction intensity of a Au@P3HT film is much smaller than that of the pristine P3HT film. Since P3HT chains are attached to the metallic surfaces of gold NPs in Au@P3HT nanocomposites, their lamellar structures are less organized, reducing the diffraction intensity by 7.94 times (Table S2-1). The thermal-annealing effect of the Au@P3HT film is similar to that of the pristine P3HT film; the diffraction intensity of the (100) planes has been clearly increased after thermal annealing.<sup>44,46b</sup> This result implies that crystalline domains exist obviously in Au@P3HT nanocomposites as shown in Figure S2-5 of the Supporting Information. Thermal annealing has increased the  $d_{100}$ -spacing values of both P3HT and Au@P3HT by 0.01 nm, suggesting that the alkyl side chains of P3HT and Au@P3HT have been expanded by thermal annealing.

The mean diameter,  $d$ , of crystallites can be determined from the line width of a HRXRD peak by using the Scherrer's formula  $d = (0.94 \lambda)/(B \cos\theta_B)$ , where  $\lambda$  is the

X-ray wavelength,  $B$  is the full width at the half maximum of the diffraction peak (in radian), and  $\theta_B$  is the half angle of the diffraction peak on the  $2\theta$  scale.<sup>2d,3b-3d,45</sup> Mean crystallite diameters, calculated by using the diffraction line widths of the (100) planes, indicate that crystallite sizes increase significantly by thermal annealing. In particular, the mean crystallite diameter of Au@P3HT increases by a factor of 2.43 with thermal annealing. This suggests that thermal annealing is essential to enhance the crystallinity of Au@P3HT nanocomposites.

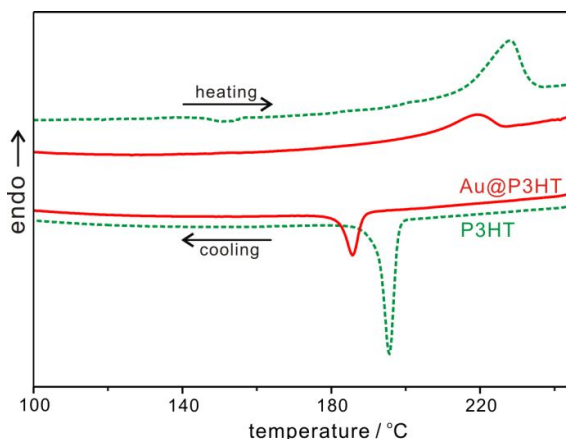


**Figure 2-5.** DSC curves of P3HT (dotted) and Au@P3HT (solid) measured at a heating or cooling rate of  $10\text{ }^{\circ}\text{C min}^{-1}$ .

The DSC curves of Figure 2-5 were measured to determine the melting ( $T_m$ ) and recrystallization ( $T_c$ ) temperatures of pristine P3HT and composite Au@P3HT. The  $T_m$  value of Au@P3HT nanocomposites ( $219.1\text{ }^{\circ}\text{C}$ ) is lower by  $9.0\text{ }^{\circ}\text{C}$  than that of pristine P3HT ( $228.1\text{ }^{\circ}\text{C}$ ) while the  $T_c$  value of Au@P3HT ( $185.8\text{ }^{\circ}\text{C}$ ) is lower by  $9.6\text{ }^{\circ}\text{C}$  than that of P3HT ( $195.4\text{ }^{\circ}\text{C}$ ). Furthermore, the intensities of the melting and recrystallization transitions of Au@P3HT nanocomposites are as weak as 36% of

those of pristine P3HT. Thus, these results suggest that gold NPs in Au@P3HT nanocomposites act as defects suppressing the ordering of polymer chains to reduce the crystallinity of P3HT.<sup>43b,46a</sup> This reduced crystallinity also results in the broadening of  $T_m$  and  $T_c$ ; the line widths of  $T_m$  and  $T_c$  in Au@P3HT are broader by 1.6 and 1.3 times than the respective ones in P3HT. Nevertheless, Figure 2-5 clearly shows that crystalline domains still remain in Au@P3HT nanocomposites. In other words, although the crystallinity of Au@P3HT nanocomposites has been reduced significantly in comparison with that of P3HT, the crystallinity of Au@P3HT nanocomposites has not been completely perished. Thus, if Au@P3HT nanocomposites are employed in photovoltaic applications, the remaining crystalline domains in Au@P3HT nanocomposites can play an important role in enhancing device efficiencies.

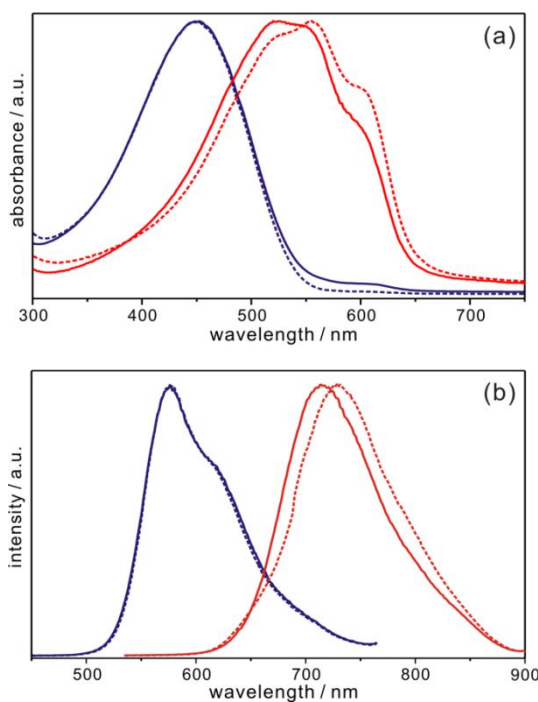


**Figure 2-6.** Peak-normalized absorption (a) and emission (b) spectra of P3HT (dotted) and Au@P3HT (solid) in chloroform (left) and films on quartz plates (right).

Figure 2-6a illustrates that the absorption spectra of pristine P3HT and composite Au@P3HT in chloroform have a broad featureless band with the maximum at 452 nm, which arises from the characteristic intrachain  $\pi$ - $\pi$  transition of P3HT.<sup>40a,42a,47b</sup> The optical band gap of pristine P3HT in chloroform estimated from the absorption edge, is 2.29 eV, whereas the band gap of Au@P3HT nanocomposites in chloroform is 2.27 eV (Table S2-2 in the Supporting Information). The absorption spectra of the spincoated films of pristine P3HT and composite Au@P3HT are considerably different from the absorption spectra of pristine P3HT and composite Au@P3HT in chloroform. The absorption spectrum of a P3HT film with the maximum at 555 nm is largely red-shifted by 103 nm from that

of P3HT in chloroform due to the increased conjugation length of the intrachain  $\pi$ - $\pi$  transition resulting from the ordered stacking of P3HT backbones.<sup>48</sup> The absorption spectrum of a P3HT film has been deconvoluted into a vibronic band at 565 nm and two shoulders at 529 and 608 nm. While the absorption peak at 529 nm can be ascribed to the intrachain  $\pi$ - $\pi$  transition of P3HT chains, the peak at 565 nm is assigned to the 0-1 transition and the shoulder peak at 608 nm is due to the 0-0 transition of interchain-delocalized excitation resulting from the strong  $\pi$ -stacking of the polymer chains.<sup>40a,42,43,46-48</sup> Highly regioregular P3HT can self-organize to align polymer chains and form semicrystalline lamellar morphologies, which possess highly ordered packing and alignment, high hole mobility, and strong interchain and interlayer interactions.<sup>43a</sup> On the other hand, the absorption spectrum of a spincoated Au@P3HT film has been deconvoluted into three bands having the maxima at 523, 561, and 605 nm, indicating that the absorption spectrum of the composite Au@P3HT film is shifted to the blue from that of the pristine P3HT film. In addition, the intensity of the band at 605 nm is less pronounced than that of the pristine P3HT film at 608 nm. Thus, the results suggest that the incorporation of gold NPs into P3HT to fabricate Au@P3HT nanocomposites deteriorates the crystallinity of P3HT significantly.<sup>43</sup>

Figure 2-6b shows that the emission spectra of both pristine P3HT and composite Au@P3HT in chloroform show the maximum at 577 nm and a shoulder at 618 nm. The broad shoulder with a long tail should be attributed to strong vibrational motions corresponding to chain stretching and torsional twisting.<sup>43a</sup> The emission maximum of a dropcoated pristine P3HT film is largely red-shifted by 153

nm from the emission maximum of the P3HT solution. Such a large red shift of the thin-film emission is a well-known consequence of improved electron delocalization in the solid state or good intermolecular ordering in a semicrystalline conjugated polymer.<sup>47</sup> On the other hand, the emission spectrum of a dropcoated composite Au@P3HT film is blue-shifted by 16 nm from that of the pristine P3HT film, suggesting that the conformation of P3HT backbones in Au@P3HT nanocomposites is coil-like or twisted considerably due to the presence of gold NPs.<sup>40a,43b</sup>

While the Stokes shift of P3HT in chloroform (0.14 eV), determined with the absorption edge and the emission maximum,<sup>40a,43b</sup> is substantially larger than that of Au@P3HT in chloroform (0.12 eV), the Stokes shift of a P3HT film (0.20 eV) is much larger than that of a Au@P3HT film (0.14 eV) (Table S2-2). It has been reported<sup>40a</sup> that the Stokes shifts of amorphous polymers are much larger than those of crystalline polymers due to the larger structural relaxation of the amorphous polymers following photoexcitation. Since gold NPs are coated by P3HT chains, the structure of Au@P3HT nanocomposites is more amorphous than that of pristine P3HT. Thus, Au@P3HT nanocomposites are expected to have a larger Stokes shift than P3HT.<sup>40a,42b,43b</sup> However, the Stokes shifts of Au@P3HT nanocomposites are smaller than those of pristine-P3HT samples. This has been attributed to the presence of strong coupling between the plasmonic field and excitons in Au@P3HT nanocomposites<sup>35</sup> (see below).

To gain an insight into photophysical interactions between SPRs of gold NPs and photo-generated excitons of P3HT within Au@P3HT nanocomposites, we have

obtained transient-absorption and fluorescence kinetic profiles of pristine P3HT and composite Au@P3HT in chloroform. Each femtosecond time-resolved transient-absorption kinetic profile of Figure 2-7 has been deconvoluted into three ground-state bleach (GSB) recovery components of 0.8 ps (55%), 8 ps (20%), and 25 ps (25%) for pristine P3HT and 0.3 ps (40%), 3 ps (32%), and 20 ps (28%) for composite Au@P3HT (Table 2-1). The exciton relaxation dynamics of P3HT in solvents has been reported<sup>36-38,40a,42,43</sup> to depend on various factors such as the self trapping of excitons (~100 fs), vibrational relaxation processes, the downhill relaxation of self-trapped excitons (~1 ps), torsional relaxation (3-10 ps), and intrachain/interchain excitation energy transfer. Thus, we have assigned the fast recovery component (0.8 ps for P3HT and 0.3 ps for Au@P3HT) to the downhill relaxation of self-trapped excitons and the medium recovery component (8 ps for P3HT and 3 ps for Au@P3HT) to the torsional relaxation of the first-excited singlet state of P3HT. The slow recovery component (25 ps for P3HT and 20 ps for Au@P3HT) has been considered to originate from the intrachain energy transfer or relaxation of first-excited singlet-state excitons. The mean GSB recovery time of Au@P3HT nanocomposites (6.7 ps) is shorter than that of P3HT (8.3 ps) (Table 2-1), indicating that energy transfer from the excited state of P3HT to the SPR state of gold NPs takes place in Au@P3HT nanocomposites.

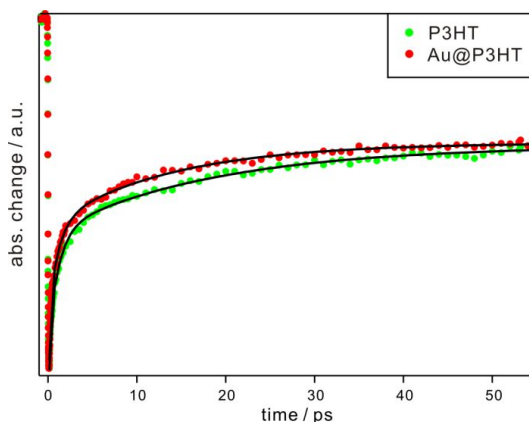


**Figure 2-7.** Femtosecond time-resolved transient-absorption kinetic profiles of P3HT and Au@P3HT in chloroform. Samples were excited at 400 nm and monitored at 400 nm, and solid lines are the best-fitted curves to extract kinetic constants.

**Table 2-1. Transient-Absorption and Fluorescence Kinetic Constants of P3HT and Au@P3HT in Chloroform**

method	sample	recovery/decay time (ps)	mean time (ps)
femtosecond absorption <sup>a</sup>	P3HT	0.8 (55%) + 8 (20%) + 25 (25%)	8.3
	Au@P3HT	0.3 (40%) + 3 (32%) + 20 (28%)	6.7
picosecond emission <sup>b</sup>	P3HT	110 (40%) + 520 (60%)	338
	Au@P3HT	95 (40%) + 485 (60%)	314
nanosecond absorption <sup>c</sup>	P3HT	240000	
	Au@P3HT	230000	

<sup>a</sup>Excited at 400 nm and probed at 400 nm. <sup>b</sup>Excited at 355 nm and monitored at 580 nm.

<sup>c</sup>Excited at 355 nm and probed at 820 nm.

Figure 2-8 shows that the fluorescence decay kinetic profiles of pristine P3HT and composite Au@P3HT in chloroform have been deconvoluted into two decay components of 110 ps (40%) and 520 ps (60%) for P3HT and 95 ps (40%) and 485 ps (60%) for Au@P3HT (Table 2-1). The fluorescence of P3HT in methylcyclohexane has been reported<sup>37</sup> to have a lifetime of ~500 ps with two

shorter decay times of 20 and 120 ps; the two shorter times have been assigned to intrachain energy transfer. Thus, we have assigned the shorter decay component (110 ps for P3HT and 95 ps for Au@P3HT) to intrachain energy transfer and the longer decay component (520 ps for P3HT and 480 ps for Au@P3HT) to the relaxation of singlet-state excitons. Because the existence of torsional defects and the coil-like conformation of polymer chains lead to a more difficult process for planarization in the excited state, the torsional relaxation of Au@P3HT nanocomposites is expected to take a longer time than that of pristine P3HT.<sup>38,40a,42,43</sup> However, as shown in Table 2-1, composite Au@P3HT has a shorter mean decay time than pristine P3HT. The shorter decay time of Au@P3HT nanocomposites is considered to associate with energy transfer from the excited state of P3HT to the SPR state of gold NPs.<sup>35</sup> The enhanced light absorption of Au@P3HT nanocomposites is considered to induce energy transfer from the excited electronic state of P3HT to the SPR state of gold NPs. Thus, while the dissociation degree of excitons is increased, the radiative and/or nonradiative recombination processes are reduced in Au@P3HT nanocomposites.<sup>35</sup> This result is in good agreement with that from the femtosecond time-resolved transient-absorption kinetic profiles of Figure 2-7.

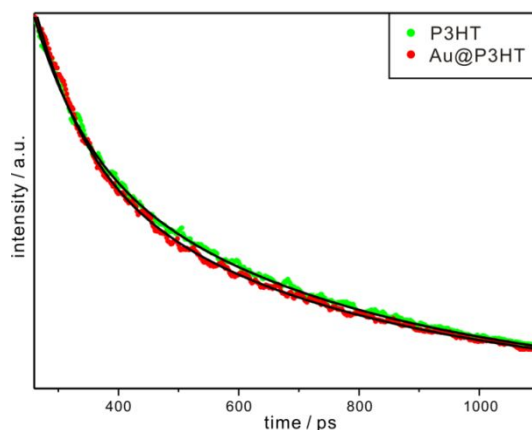


**Figure 2-8.** Picosecond time-resolved fluorescence kinetic profiles of P3HT and Au@P3HT in chloroform. Samples were excited at 355 nm and monitored at 580 nm, and solid lines are the best-fitted curves to extract kinetic constants.

The nanosecond time-resolved transient-absorption kinetic profiles of pristine P3HT and composite Au@P3HT in chloroform (Figure 2-9) have been deconvoluted into a single decay component of 240 ns for pristine P3HT and 230 ns for composite Au@P3HT (Table 2-1). We have assigned the observed decay time to the lifetime of triplet-state excitons,<sup>36</sup> suggesting that the triplet state of P3HT is slightly quenched by the presence of gold NPs in Au@P3HT nanocomposites. Furthermore, the amplitude of triplet-state absorption is less pronounced in the nanocomposites; triplet-state excitons are populated in a smaller quantum yield in Au@P3HT nanocomposites.<sup>42b</sup> This has been attributed to energy transfer from the first-excited singlet state of P3HT to the SPR state of gold NPs in the nanocomposites, as already described with Figures 2-7 and 2-8. Thus, we consider the incorporation of gold NPs into P3HT reduces the recombination of geminate excitons and increases the probability of exciton dissociation. The increase of exciton dissociation via decreasing exciton recombination by the presence of gold

NPs would enhance both the photocurrent and fill factors of P3HT-employed organic photovoltaic devices significantly.

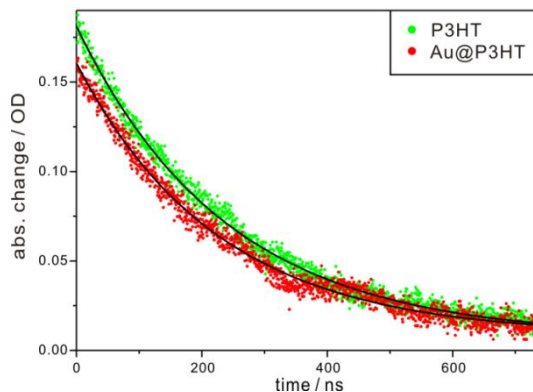


**Figure 2-9.** Nanosecond time-resolved transient-absorption kinetic profiles of P3HT and Au@P3HT in chloroform. Samples were excited at 355 nm and monitored at 820 nm. Solid lines are the best-fitted curves to extract time constants.

## 2. 5. Conclusions

Gold nanoparticles (NPs) have been incorporated by reducing a gold precursor directly into thiol-terminated P3HT to fabricate P3HT-coated gold (Au@P3HT) hybrid nanoparticles, where organic and inorganic phases are well-dispersed at the molecular level. The decomposition temperature of Au@P3HT nanocomposites is higher by 2.7 °C than that of pristine P3HT, suggesting that covalent-bond interactions between the thiol group of P3HT and the surface of gold NPs exist in the nanocomposites. The diffraction intensity of a Au@P3HT film is eight times smaller than that of a pristine P3HT film, indicating that the lamellar structures of Au@P3HT nanocomposites are less organized because P3HT chains are attached to the metallic surfaces of gold NPs. The mean crystallite diameter of Au@P3HT has

been found to increase by a factor of 2.4 with thermal annealing, suggesting that thermal annealing is essential to enhance the crystallinity of the composite nanostructures. Melting and recrystallization temperatures have revealed that although the crystallinity of Au@P3HT nanocomposites has been reduced significantly in comparison with that of P3HT, it has not been completely perished. The Stokes shift of composite Au@P3HT has been found to be smaller than that of pristine P3HT, suggesting that the plasmonic field of gold NPs couples strongly with excitons of P3HT in Au@P3HT nanocomposites. Femtosecond time-resolved transient absorption kinetic profiles as well as fluorescence kinetic profiles have shown that the relaxation of the first-excited singlet state of P3HT is significantly faster in composite Au@P3HT than in pristine P3HT, suggesting that energy transfer from the first-excited singlet state of P3HT to the SPR state of gold NPs takes place in Au@P3HT nanocomposites. On the other hand, the triplet-state lifetime of P3HT is slightly reduced by the presence of gold NPs in Au@P3HT nanocomposites. However, triplet-state excitons are populated in a smaller quantum yield in Au@P3HT nanocomposites. This result also indicates that energy transfer from the first-excited singlet state of P3HT to the SPR state of gold NPs takes place in the nanocomposites. Thus, it is suggested that our incorporation of gold nanoparticles into P3HT reduces the recombination of geminate excitons and, thereby, increases the probability of exciton dissociation, enhancing both the photocurrents and fill factors of P3HT-employed organic photovoltaic devices significantly.

## 2. 6. References

- (1) (a) Noguez, C. *J. Phys. Chem. C* **2007**, *111*, 3806–3819. (b) Ray, P. C. *Chem. Rev.* **2010**, *110*, 5332–5365.
- (2) (a) Kim, S. J.; Ah, C. S.; Jang, D.-J. *Adv. Mater.* **2007**, *19*, 1064–1068. (b) Kim, M. R.; Park, S.-Y.; Jang, D.-J. *Adv. Funct. Mater.* **2009**, *19*, 3910–3916. (c) Park, S.-Y.; Jeong, H.; Kim, H.; Lee, J. Y.; Jang, D.-J. *J. Phys. Chem. C* **2011**, *115*, 24763–24770. (d) Kim, J.-Y.; Lee, D.; Kim, H. J.; Lim, I.; Lee, W. I.; Jang, D.-J. *J. Mater. Chem. A* **2013**, *1*, 5982–5988.
- (3) (a) Kim, J.-Y.; Kim, S. J.; Jang, D.-J. *J. Phys. Chem. C* **2011**, *115*, 672–675. (b) Kim, Y.; Kim, J.-Y.; Jang, D.-J. *J. Phys. Chem. C* **2012**, *116*, 10296–10302. (c) Kim, H.-B.; Jang, D.-J. *CrystEngComm* **2012**, *14*, 6946–6951. (d) Kim, Y.; Jang, D.-J. *Chem. Commun.* **2013**, *49*, 8940–8942.
- (4) (a) Kim, M. R.; Kim, J.-Y.; Kim, S. J.; Jang, D.-J. *Appl. Catal., A* **2011**, *393*, 317–322. (b) Kwak, J.-A.; Lee, D.; Jang, D.-J. *Appl. Catal., B* **2013**, *142–143*, 323–328.
- (5) Reiss, P.; Couderc, E; De Girolamo, J.; Pron, A. *Nanoscale* **2011**, *3*, 446–489.
- (6) Duarte, A.; Pu, K.-Y.; Liu, B.; Bazan, G. C. *Chem. Mater.* **2011**, *23*, 501–515.
- (7) Stratakis, E.; Kymakis, E. *Mater. Today* **2013**, *16*, 133–146.

- (8) (a) Scharber, M. C.; Mühlbacher, D.; Koppe, M.; Denk, P.; Waldauf, C.; Heeger, A. J.; Brabec, C. J. *Adv. Mater.* **2006**, *18*, 789–794. (b) Hains, A. W.; Liang, Z.; Woodhouse, M. A.; Gregg, B. A. *Chem. Rev.* **2010**, *110*, 6689–6735. (c) Lubber, E. J.; Buriak, J. M. *ACS Nano* **2013**, *7*, 4708–4714.
- (9) (a) Halls, J. J. M.; Pichler, K.; Friend, R. H.; Moratti, S. C.; Holmes, A. B. *Appl. Phys. Lett.* **1996**, *68*, 3120–3122. (b) Shaheen, S. E.; Brabec, C. J.; Sariciftci, N. S.; Padinger, F.; Fromherz, T.; Hummelen, J. C. *Appl. Phys. Lett.* **2001**, *78*, 841–843.
- (10)(a) Jamieson, F. C.; Agostinelli, T.; Azimi, H.; Nelson, J.; Durrant, J. R. *J. Phys. Chem. Lett.* **2010**, *1*, 3306–3310. (b) Albrecht, S.; Schindler, W.; Kurpiers, J.; Kniepert, J.; Blakesley, J. C.; Dumsch, I.; Allard, S.; Fostiropoulos, K.; Scherf, U.; Neher, D. *J. Phys. Chem. Lett.* **2012**, *3*, 640–645.
- (11)(a) Brenner, T. J. K.; McNeill, C. R. *J. Phys. Chem. C* **2011**, *115*, 19364–19370. (b) Luria, J. L.; Hoepker, N.; Bruce, R.; Jacobs, A. R.; Groves, C.; Marohn, J. A. *ACS Nano* **2012**, *6*, 9392–9401.
- (12) Coakley, K. M.; McGehee, M. D. *Chem. Mater.* **2004**, *16*, 4533–4542.
- (13) Facchetti, A. *Chem. Mater.* **2011**, *23*, 733–758.
- (14)(a) Iovu, M. C.; Sheina, E. E.; Gil, R. R.; McCullough, R. D. *Macromolecules* **2005**, *38*, 8649–8656. (b) Jeffries-El, M.; Sauv e, G.; McCullough, R. D. *Macromolecules* **2005**, *38*, 10346–10352. (c) Osaka, I.; McCullough, R. D. *Acc. Chem. Res.* **2008**, *41*, 1202–1214.

- (15) (a) Palaniappan, K.; Murphy, J. W.; Khanam, N.; Horvath, J.; Alshareef, H.; Quevedo-Lopez, M.; Biewer, M. C.; Park, S. Y.; Kim, M. J.; Gnade, B. E.; et al. *Macromolecules* **2009**, *42*, 3845–3848. (b) Palaniappan, K.; Hundt, N.; Sista, P.; Nguyen, H.; Hao, J.; Bhatt, M. P.; Han, Y.-Y.; Schmiedel, E. A.; Sheina, E. E.; Biewer, M. C.; et al. *J. Polym. Sci., Part A: Polym. Chem.* **2011**, *49*, 1802–1808.
- (16) (a) Wuelfing, W. P.; Gross, S. M.; Miles, D. T.; Murray, R. W. *J. Am. Chem. Soc.* **1998**, *120*, 12696–12697. (b) Corbierre, M. K.; Cameron, N. S.; Sutton, M.; Mochrie, S. G. J.; Lurio, L. B.; Rühm, A.; Lennox, R. B. *J. Am. Chem. Soc.* **2001**, *123*, 10411–10412. (c) Corbierre, M. K.; Cameron, N. S.; Lennox, R. B. *Langmuir* **2004**, *20*, 2867–2873. (d) Hussain, I.; Graham, S.; Wang, Z.; Tan, B.; Sherrington, D. C.; Rannard, S. P.; Cooper, A. I.; Brust, M. *J. Am. Chem. Soc.* **2005**, *127*, 16398–16399.
- (17) Yamamoto, S.; Ohkita, H.; Benten, H.; Ito, S. *J. Phys. Chem. C* **2012**, *116*, 14804–14810.
- (18) Hou, J.; Chen, T. L.; Zhang, S.; Chen, H.-Y.; Yang, Y. *J. Phys. Chem. C* **2009**, *113*, 1601–1605.
- (19) Fischer, F. S. U.; Tremel, K.; Saur, A.-K.; Link, S.; Kayunkid, N.; Brinkmann, M.; Herrero-Carvajal, D.; López Navarrete, J. T.; Ruiz Delgado, M. C.; Ludwigs, S. *Macromolecules* **2013**, *46*, 4924–4931.
- (20) Mao, Z.; Vakhshouri, K.; Jaye, C.; Fischer, D. A.; Fernando, R.; DeLongchamp, D. M.; Gomez, E. D.; Sauvé, G. *Macromolecules* **2013**,

46, 103–112.

- (21) Richter, T. V.; Braun, C. H.; Link, S.; Scheuble, M.; Crossland, E. J. W.; Stelzl, F.; Würfel, U.; Ludwigs, S. *Macromolecules* **2012**, *45*, 5782–5788.
- (22) Sary, N.; Richard, F.; Brochon, C.; Leclerc, N.; Lévêque, P.; Audinot, J.-N.; Berson, S.; Heiser, T.; Hadziioannou, G.; Mezzenga, R. *Adv. Mater.* **2010**, *22*, 763–768.
- (23) Lombardo, C. J.; Danielson, E. L.; Glaz, M. S.; Ooi, Z.-E.; Vanden Bout, D. A.; Dodabalapur, A. *J. Phys. Chem. B* **2013**, *117*, 4503–4509.
- (24) Liao, H.-C.; Tsao, C.-S.; Lin, T.-H.; Jao, M.-H.; Chuang, C.-M.; Chang, S.-Y.; Huang, Y.-C.; Shao, Y.-T.; Chen, C.-Y.; Su, C.-J.; et al. *ACS Nano* **2012**, *6*, 1657–1666.
- (25) Tu, Y.-C.; Lin, J.-F.; Lin, W.-C.; Liu, C.-P.; Shyue, J.-J.; Su, W.-F. *CrystEngComm* **2012**, *14*, 4772–4776.
- (26) Shen, H.; Bienstman, P.; Maes, B. *J. Appl. Phys.* **2009**, *106*, 073109.
- (27) Yen, W.-C.; Lee, Y.-H.; Lin, J.-F.; Dai, C.-A.; Jeng, U.-S.; Su, W.-F. *Langmuir* **2011**, *27*, 109–115.
- (28) Huynh, W. U.; Dittmer, J. J.; Alivisatos, A. P. *Science* **2002**, *295*, 2425–2427.
- (29) Sun, B.; Marx, E.; Greenham, N. C. *Nano Lett.* **2003**, *3*, 961–963.
- (30) Xu, J.; Wang, J.; Mitchell, M.; Mukherjee, P.; Jeffries-EL, M.; Petrich, J. W.; Lin, Z. *J. Am. Chem. Soc.* **2007**, *129*, 12828–12833.
- (31)(31). (a) Kim, K.; Carrola, D. L. *Appl. Phys. Lett.* **2005**, *87*, 203113. (b)

- Kim, C.-H.; Cha, S.-H.; Kim, S. C.; Song, M.; Lee, J.; Shin, W. S.; Moon, S.-J.; Bahng, J. H.; Kotov, N. A.; Jin, S.-H. *ACS Nano* **2011**, *5*, 3319–3325.
- (32) Liao, W.-P.; Hsu, S.-C.; Lin, W.-H.; Wu, J.-J. *J. Phys. Chem. C* **2012**, *116*, 15938–15945.
- (33) (a) Kuila, B. K.; Garai, A.; Nandi, A. K. *Chem. Mater.* **2007**, *19*, 5443–5452. (b) Stavvytska-Barba, M.; Salvador, M.; Kulkarni, A.; Ginger, D. S.; Kelley, A. M. *J. Phys. Chem. C* **2011**, *115*, 20788–20794.
- (34) Nicholson, P. G.; Ruiz, V.; Macpherson, J. V.; Unwin, P. R. *Chem. Commun.* **2005**, 1052–1054.
- (35) Wu, J.-L.; Chen, F.-C.; Hsiao, Y.-S.; Chien, F.-C.; Chen, P.; Kuo, C.-H.; Huang, M. H.; Hsu, C.-S. *ACS Nano* **2011**, *5*, 959–967.
- (36) Cook, S.; Furube, A.; Katoh, R. *Energ. Environ. Sci.* **2008**, *1*, 294–299.
- (37) Ferreira, B.; da Silva, P. F.; Seixas de Melo, J. S.; Pina, J.; Maçanita, A. *J. Phys. Chem. B* **2012**, *116*, 2347–2355.
- (38) Busby, E.; Carroll, E. C.; Chinn, E. M.; Chang, L.; Moulé, A. J.; Larsen, D. S. *J. Phys. Chem. Lett.* **2011**, *2*, 2764–2769.
- (39) (a) Sariciftci, N. S.; Smilowitz, L.; Heeger, A. J.; Wudi, F. *Science* **1992**, *258*, 1474–1476. (b) Yu, G.; Gao, J.; Hummelen, J. C.; Wudi, F.; Heeger, A. J. *Science* **1995**, *270*, 1789–1791.
- (40) (a) Ohkita, H.; Cook, S.; Astuti, Y.; Duffy, W.; Tierney, S.; Zhang, W.; Heeney, M.; McCulloch, I.; Nelson, J.; Bradley, D. D. C.; et al. *J. Am. Chem. Soc.* **2008**, *130*, 3030–3042. (b) Guo, J.; Ohkita, H.; Benten, H.;

- Ito, S. *J. Am. Chem. Soc.* **2010**, *132*, 6154–6164. (c) Guo, J.; Ohkita, H.; Bente, H.; Ito, S. *J. Am. Chem. Soc.* **2009**, *131*, 16869–16880.
- (41)(a) Grancini, G.; Polli, D.; Fazzi, D.; Cabanillas-Gonzalez, J.; Cerullo, G.; Lanzani, G. *J. Phys. Chem. Lett.* **2011**, *2*, 1099–1105. (b) Grancini, G.; Biasiucci, M.; Matria, R.; Scotognella, F.; Tassone, F.; Polli, D.; Gigli, G.; Lanzani, G. *J. Phys. Chem. Lett.* **2012**, *3*, 517–523.
- (42)(a) Banerji, N.; Cowan, S.; Vauthey, E.; Heeger, A. J. *J. Phys. Chem. C* **2011**, *115*, 9726–9739. (b) Banerji, N.; Seifert, J.; Wang, M.; Vauthey, E.; Wudl, F.; Heeger, A. J. *Phys. Rev. B* **2011**, *84*, 075206.
- (43)(a) Xie, Y.; Li, Y.; Xiao, L.; Qiao, Q.; Dhakal, R.; Zhang, Z.; Gong, Q.; Galipeau, D.; Yan, X. *J. Phys. Chem. C* **2010**, *114*, 14590–14600. (b) Xu, T.; Yan, M.; Hoefelmeyer, J. D.; Qiao, Q. *RSC Adv.* **2012**, *2*, 854–862.
- (44)(a) Yang, H.; Shin, T. J.; Yang, L.; Cho, K.; Ryu, C. Y.; Bao, Z. *Adv. Funct. Mater.* **2005**, *15*, 671–676. (b) Ma, W.; Yang, C.; Gong, X.; Lee, K.; Heeger, A. J. *Adv. Funct. Mater.* **2005**, *15*, 1617–1622. (c) Martín, J.; Nogales, A.; Martín-González, M. *Macromolecules* **2013**, *46*, 1477–1483.
- (45)(a) Routkevitch, D.; Bigioni, T.; Moskovits, M.; Xu, J. M. *J. Phys. Chem.* **1996**, *100*, 14037–14047. (b) Chen, J.; Yu, X.; Hong, K.; Messman, J. M.; Pickel, D. L.; Xiao, K.; Dadmun, M. D.; Mays, J. W.; Rondinone, A. J.; Sumpter, B. G.; et al. *J. Mater. Chem.* **2012**, *22*, 13013–13022.

- (46) (a) Lee, J. U.; Jung, J. W.; Emrick, T.; Russell, T. P.; Jo, W. H. *J. Mater. Chem.* **2010**, *20*, 3287–3294. (b) Lee, J. U.; Jung, J. W.; Emrick, T.; Russell, T. P.; Jo, W. H. *Nanotechnology* **2010**, *21*, 105201.
- (47) (a) Wu, P.-T.; Xin, H.; Kim, F. S.; Ren, G.; Jenekhe, S. A. *Macromolecules* **2009**, *42*, 8817–8826. (b) Carach, C.; Gordon, M. J. *J. Phys. Chem. B* **2013**, *117*, 1950–1957.
- (48) He, M.; Zhao, L.; Wang, J.; Han, W.; Yang, Y.; Qiu, F.; Lin, Z. *ACS Nano* **2010**, *4*, 3241–3247.

## 2. 7. Supporting Infomation

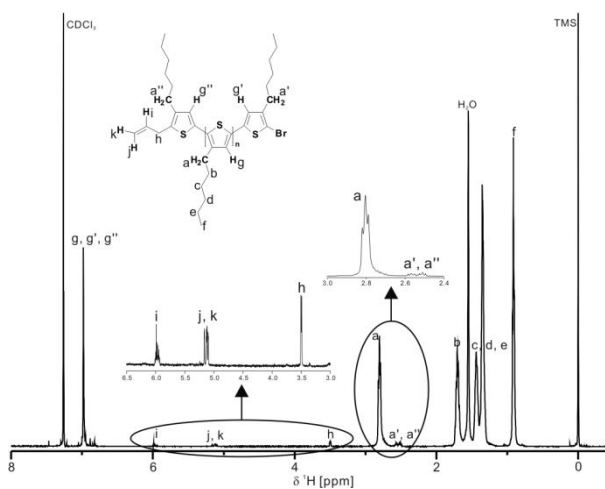


**Figure S2-1.** <sup>1</sup>H NMR spectrum (500 MHz, CDCl<sub>3</sub>) of allyl-terminated P3HT.

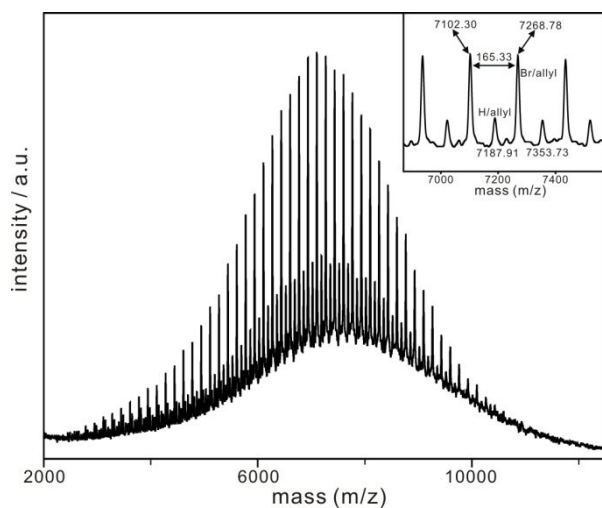


Figure S2-2. MALDI-TOF mass spectrum of allyl-terminated P3HT.

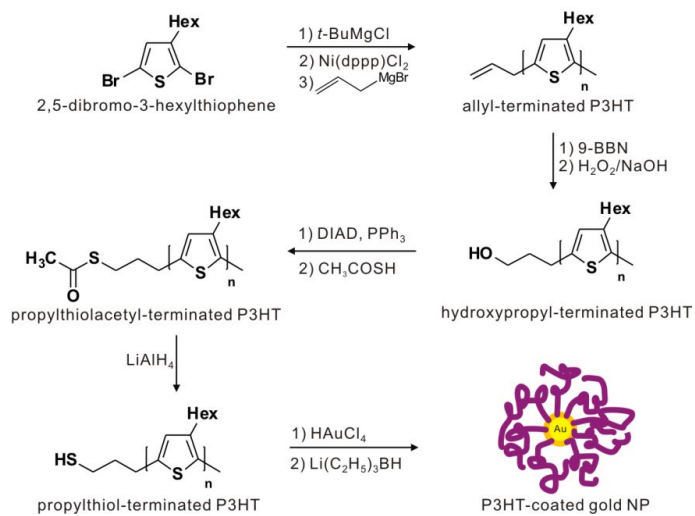
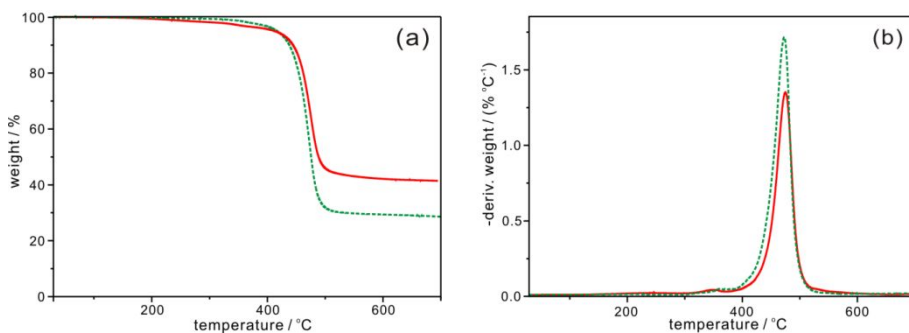


Figure S2-3. Schematic for the synthesis of a Au@P3HT nanocomposite.



**Figure S2-4.** TGA curves (a) and TGA derivative curves (b) of P3HT (dotted) and Au@P3HT (solid).

**Table S2-1. XRD Values of the Dropcoated Films of P3HT and Au@P3HT**

Sample	Relative (integrated) intensity	$2\theta_{100}$ (degree)	$d_{100}$ -spacing (nm)	Diameter (nm)
P3HT before annealing	1.00	$5.48 \pm 0.25$	$1.61 \pm 0.07$	16
P3HT after annealing	1.44	$5.46 \pm 0.17$	$1.62 \pm 0.05$	25
Au@P3HT before annealing	0.126	$5.53 \pm 0.38$	$1.60 \pm 0.11$	11
Au@P3HT after annealing	0.166	$5.48 \pm 0.15$	$1.61 \pm 0.04$	27

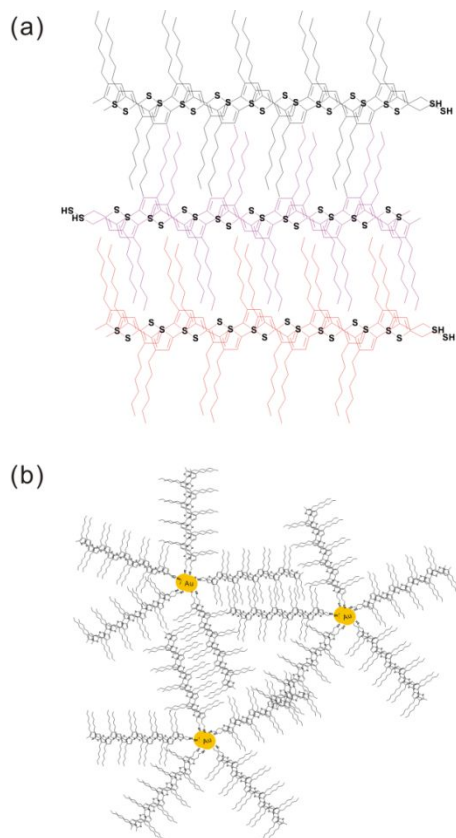


**Figure S2-5.** Schematic structures of P3HT (a) and Au@P3HT (b).

**Table S2-2. Photophysical Properties of P3HT and Au@P3HT**

Sample	Absorption $\lambda_{\max}$ (nm)	Emission $\lambda_{\max}$ (nm)	$E_g^{\text{opt}}$ (eV)	$\Delta E_{\text{Stokes}}$ (eV)
P3HT in chloroform	452	577	2.29	0.14
Au@P3HT in chloroform	452	577	2.27	0.12
P3HT film	565	730	1.90	0.20
Au@P3HT film	523	714	1.88	0.14

## **Chapter 3. Effects of Gold Nanorods on the Excited-State Dynamics and Photovoltaic Performances of Hybrid Nanocomposites Containing P3HT**

### 3. 1. Abstract

Poly(3-hexylthiophene)-stabilized gold nanorods (Au-NR@P3HT nanocomposites) have been facilely fabricated by incubating Au nanorods (NRs) with thiol-terminated P3HT to investigate the effects of Au NRs on the excited-state dynamics and photovoltaic performances of P3HT. The  $S_1$  decay of Au-NR@P3HT nanocomposites is found to be slower than that of pristine P3HT, suggesting that the stretched-strand conformation of P3HT chains attached to Au NRs makes structural relaxation more difficult. The amplitude of  $T_1$  absorption is much smaller in Au-NR@P3HT nanocomposites than in pristine P3HT, indicating that the intersystem crossing of  $S_1$  excitons into  $T_1$  excitons does not occur efficiently in Au-NR@P3HT nanocomposites due to the nonflexible character of aggregated P3HT chains. From the comparison of the performances of organic photovoltaic devices, we have found that the device with the 3% embedding of Au-NR@P3HT nanocomposites into the P3HT matrix of the active layer shows significantly improved photovoltaic performances (27% enhancement in the power conversion efficiency), suggesting that the surface-plasmon resonances of Au NRs enhance the dissociation as well as the generation of excitons highly.

### 3. 2. Introduction

Hybrid nanocomposites can provide diverse opportunities for the development of novel nanomaterials having improved physical and chemical properties against single-component counterparts.<sup>1-2</sup> In particular, hybrid nanocomposites consisting of conjugated polymers (CPs) and inorganic nanoparticles (NPs) have received intense attention for applications in optoelectronic devices because of their excellent optical and transport properties highly dependent on their nanoscale morphology.<sup>3-6</sup> The presence of an interface within a hybrid nanocomposite containing organic CPs such as poly(3-hexylthiophene) (P3HT) and alkoxy-substituted poly(phenylenevinylenes) and inorganic NPs such as Au, Ag, CdSe, and TiO<sub>2</sub> may promote charge transfer and charge separation.<sup>7,8</sup> Moreover, organic polymer shells can protect unstable inorganic NPs cores from chemical poisoning, corrosion, and dissolution, as inorganic NPs alone tend to react or aggregate because of their poor stability in a medium.<sup>9</sup> Organic photovoltaic (OPV) devices containing active layers based on CPs have been widely explored due to their low device-fabrication cost, lightweight, and large area.<sup>10-12</sup> In spite of these important advantages, they have rarely been commercialized well due to their low power-conversion efficiency.<sup>13,14</sup> Thus, in order to overcome this low-efficiency problem, diverse researchers have focused on the synthesis of low band-gap conjugated polymers,<sup>15</sup> the enhancement of the functionality of conjugated polymers,<sup>16</sup> the development of a variety of device-fabrication processes,<sup>17</sup> and the preparation of hybrid nanocomposites

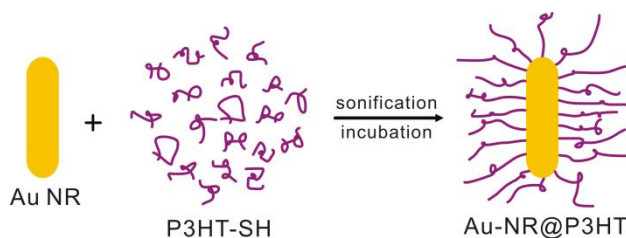
composed of inorganic nanocrystals and organic CPs for use in active layer materials.<sup>18</sup>

Among inorganic NPs, in particular, nanoclusters and colloids of noble metals show strong absorption bands in the visible region due to the surface-plasmon oscillation modes of their conduction electrons.<sup>19,20</sup> Thus, the optical properties of Ag and Au NPs have received considerable attention. Au nanorods (NRs) exhibit rich surface-plasmon resonances (SPRs)-derived properties, which have made them useful for many interesting applications such as optical and optoelectronic devices and biomedical technologies.<sup>21,22</sup> Au NRs possess two distinctive, transverse and longitudinal, SPR modes, the latter one of which exhibits a strong peak tunable from the visible to the near-infrared region with increasing aspect ratios.<sup>23</sup>

Since the enhancement of power-conversion efficiency in organic solar cells is an important challenge, the comprehensive investigation and understanding of the fundamental photophysical dynamics of conjugated polymers such as P3HT, most commonly used in the active layer of an organic solar-cell device, are critical research points for the development of new materials used for the active layer.<sup>24,25</sup> The formation and decay mechanisms of photoinduced charge carriers for CPs have been investigated extensively by using time-resolved spectroscopy.<sup>26-30</sup> The efficient dissociation and transfer of excitons photo-generated from P3HT have a lot of influence on the overall efficiency of OPV devices. To improve these processes within an active layer, we have introduced Au NPs having SPRs, which exhibit intense light absorption in the visible region, in a P3HT matrix to fabricate a P3HT-stabilized Au NPs. Since a SPR band of Au NPs is spectrally similar to the

absorption band of P3HT, we anticipate that the degree of light absorption will be enhanced in the hybrid nanocomposites.<sup>31</sup> In order to maximize the dissociation and transfer of the photo-generated excitons of P3HT, it is necessary to disperse Au NPs homogeneously at the molecular level through the P3HT matrix of the nanocomposites via chemical-bond interactions and to find optimum conditions for the dissociation of photo-generated excitons.

In this paper, poly(3-hexylthiophene)-stabilized Au nanorods (Au-NR@P3HT nanocomposites) have been facilely fabricated by incubating Au NRs with thiol-terminated P3HT (Scheme 3-1) to investigate the effects of Au NRs on the excited-state dynamics and photovoltaic performances of P3HT. In static emission spectra, a shoulder around 620 nm arising from vibronic transitions related to the strong chain-stretching and torsional-twisting motions of Au-NR@P3HT nanocomposites is much stronger than that of pristine P3HT or P3HT-stabilized gold nanospheres (Au-NS@P3HT nanocomposites). The  $S_1$  decay of Au-NR@P3HT nanocomposites is found to be slower than that of pristine P3HT nanocomposites. This result suggests that the stretched-strand conformation of P3HT chains attached to Au NRs makes structural relaxation more difficult. Because the intersystem crossing of  $S_1$  excitons into  $T_1$  excitons does not occur efficiently,  $T_1$  excitons are populated in a smaller quantum yield in Au-NR@P3HT nanocomposites. Measuring the performances of organic photovoltaic devices (OPVs) prepared with and without Au-NR@P3HT nanocomposites in active layers, we have found that the 3% embedding of Au-NR@P3HT nanocomposites increases the power conversion efficiency by 27%.



**Scheme 3-1.** Fabrication of P3HT-stabilized gold nanorods (Au-NR@P3HT nanocomposites).

### 3. 3. Experimental Section

**3. 3. 1. Syntheses.** The detailed synthetic and characterization procedures of thiol-terminated poly(3-hexylthiophene) (P3HT-SH) ( $M_n = 10,565 \text{ g mol}^{-1}$ , PDI = 1.26, MALDI-MS  $m/z = 6,875.3$ ) and P3HT-functionalized gold nanospheres (Au-NS@P3HT nanocomposites) have already been reported.<sup>27b</sup> Cetyltrimethylammonium bromide (CTAB)-stabilized Au NRs dispersed in water were fabricated according to a reported seed-mediated and CTAB-assisted method.<sup>23a</sup> P3HT-functionalized Au NRs (Au-NR@P3HT nanocomposites) were synthesized as described in detail elsewhere.<sup>32</sup> 0.5 mL of a concentrated ( $1.0 \text{ mg mL}^{-1}$ ) aqueous colloidal solution of Au NRs was added to 5.0 mL of a 0.2 wt% solution of P3HT-SH in tetrahydrofuran (THF), and the mixed solution was sonicated for 30 min and incubated for 24 h. Produced Au-NR@P3HT nanocomposites were centrifuged twice for 30 min at 10,000 rpm for the elimination of excess pristine P3HT-SH chains. The precipitated nanocomposites were then dried under a vacuum for 24 h at 40 °C. The Au-NR@P3HT composites were well-dispersed in THF without being precipitated.

**3. 3. 2. Characterization.** Transmission electron microscopy (TEM) images were obtained with a Hitachi H7600 microscope, and high resolution X-ray photoelectron spectroscopy (HRXPS) data were obtained using a Sigma Probe ThermoVG photoelectron spectrometer with an excitation source of Al Ka radiation (1486.7 eV). While absorption spectra were measured with a Scinco S3100 UV/vis spectrophotometer, emission spectra were obtained using a home-built fluorometer consisting of a 75 W Acton Research XS 432 Xe lamp with a 0.15 m Acton Research Spectrapro150 monochromator and an Acton Research PD438 photomultiplier tube attached to a 0.30 m Acton Research Spectrapro300 monochromator. Nanosecond transient-absorption kinetic profiles were obtained by monitoring the beam intensity of a 75 W Acton Research XS 432 Xe lamp transmitted through a sample, which was excited with 355 nm pulses having a duration time of 6 ns from a Q-switched Quantel Brilliant Nd:YAG laser. Picosecond fluorescence kinetic profiles with excitation of 355 nm pulses from a 25 ps mode-locked Quantel YG901-10 Nd:YAG laser were detected using a 10 ps Hamamatsu C2830 streak camera attached to a Princeton Instruments RTE128H CCD detector. Transient-absorption and emission kinetic constants were extracted by fitting measured kinetic profiles to computer-simulated curves convoluted with instrumental temporal-response functions.

**3. 3. 3. Solar cell device fabrication and measurements.** Solar cells were fabricated with the structure of ITO/PEDOT:PSS/P3HT:PCBM:P3HT-functionalized Au NPs/Ca/Al. The patterned indium tin oxide (ITO) glass

substrate was pre-cleaned in an ultrasonic bath of distilled water, acetone, and isopropanol, and then exposed to a UV-ozone clean (Ahtech LTS) for 20 min. A 30–40 nm layer of PEDOT:PSS (Clavious P VP AI 4083) was spin-coated onto the ITO glass (5000 rpm, 30 s) and baked on a hot plate at 150 °C for 20 min. Subsequently, the weight ratio-blended solution (18 mg mL<sup>-1</sup> in chlorobenzene or 20 mg mL<sup>-1</sup> in o-dichlorobenzene) of P3HT (Rieke Metals, RMI-001EE) and PCBM (Nano-C), P3HT-functionalized Au NPs were filtered using 0.50 µm syringe filters and spin-coated at 1300 rpm for 60 s in a chlorobenzene solution or 600 rpm for 60 s in an o-dichlorobenzene solution in a N<sub>2</sub> glovebox. After drying the resulting films in a N<sub>2</sub> glovebox at room temperature for 1 h, a 7 nm layer of Ca and a 100 nm layer of Al were deposited via thermal evaporation under a vacuum of 10<sup>-6</sup> torr. The current density (*J*) – voltage (*V*) characteristics of the solar cells were measured using a Keithley 4200 source measurement unit. The solar cell performances were characterized under AM 1.5G conditions with an illumination intensity of 100 mW cm<sup>-2</sup> generated by an Oriel Sol3A solar simulator. The lamp irradiation was calibrated using an NREL-certified KG-5 filtered standard silicon photodiode (VLSI Standards). The active area was 0.05 cm<sup>2</sup>, and measurements were carried out through a shadow mask under an ambient atmosphere.

### 3. 4. Results and Discussion

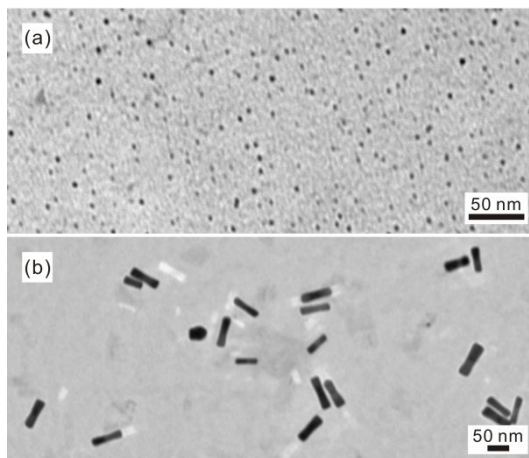


**Figure 3-1.** TEM images of Au-NS@P3HT (a) and Au-NR@P3HT nanocomposites (b).

Figure 3-1a shows the TEM images of Au-NS@P3HT nanocomposites having an average gold diameter of  $2.8 \pm 1.4$  nm. We have incorporated Au NSs directly into P3HT-SH via a ‘grafting-to’ approach.<sup>29b</sup> While Figure S3-1 shows the TEM image of Au NRs having an average length of  $69 \pm 10$  nm with a typical aspect ratio of  $3.8 \pm 0.6$  and the absorption maximum of longitudinal surface-plasmon resonances at 824 nm, Figure 3-1b shows the TEM image of Au-NR@P3HT nanocomposites prepared by adding an aqueous solution of Au NRs to a THF solution of P3HT-SH. Because Au NRs are surrounded by P3HT-SH chains, Au-NR@P3HT nanocomposites can be well-dispersed and stabilized in THF. The grafting density of P3HT-SH on the surface of Au NRs was estimated by calculating the molar concentration ratio of P3HT to Au NRs with the absorption spectrum of Au-NR@P3HT nanocomposites dispersed in THF.<sup>23b</sup>  $3.0 \times 10^4$  P3HT chains have been estimated to surround a Au NR. In other words, the molar mass of

Au-NR@P3HT nanocomposites becomes  $3.6 \times 10^8$  g and the weight ratio of Au NRs to P3HT chains corresponds to  $5.6 \times 10^{-4}$  as the molar masses of P3HT chains and Au NRs have been estimated to be 10.565 and  $2.0 \times 10^5$  g, respectively. As gold can bind strongly with thiol molecules, Au NRs have been coated with an organic matrix of P3HT-SH via chemical-bond interactions, consequently producing well-dispersive and stable Au-NR@P3HT nanocomposites having organic and inorganic phases homogeneously at the molecular level.

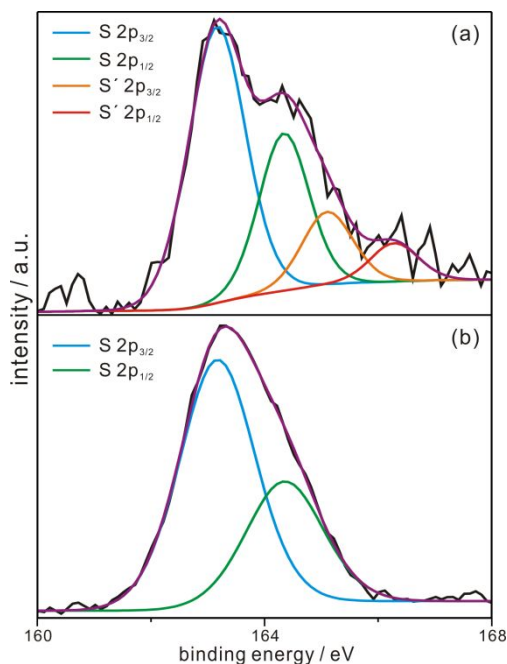


**Figure 3-2.** XPS spectra of P3HT-SH (a) and Au-NR@P3HT nanocomposites (b). Violet curves represent the sum of fitted curves.

**Table 3-1. Binding Energies in eV for the Deconvoluted Curves of S 2p XPS Spectra**

sample	S 2p <sub>3/2</sub>	S 2p <sub>1/2</sub>	S' 2p <sub>3/2</sub>	S' 2p <sub>1/2</sub>
P3HT-SH	163.16 (54.0%)	164.34 (27.0%)	165.10 (12.7%)	166.28 (6.3%)
Au-NR@P3HT	163.17 (66.7%)	164.35 (33.3%)		

The XPS spectra of P3HT-SH and Au-NR@P3HT nanocomposites in Figure 3-2 can provide significant information further on chemical-bond interactions between thiol molecules and Au NR surfaces. The S 2p XPS spectrum of pristine P3HT-SH in Figure 3-2a exhibits two sets of doublet peaks having a spin-orbit splitting of 1.18 eV in each set and an area ratio of 1:2 in accord with theoretical numbers from the spin-orbit splitting effect (Table 3-1). These two sets of peaks corroborate the presence of two types of sulfur species in pristine P3HT chains; S and S' species with the lower and the higher binding energies, respectively, of Table 3-1 are attributed to arise from thiophene rings and free thiol terminal groups, respectively. However, the XPS spectrum of Au-NR@P3HT nanocomposites in Figure 3-2b shows only one set of doublet peaks because the binding energy of sulfur covalently bonded to gold, whose electronegativity value (2.54) is very similar to the electronegativity value of carbon (2.55), is almost the same as that of sulfur in a thiophene ring. Therefore, the XPS spectra of Figure 3-2 provide a direct evidence for the chemical-bond interactions of the thiol group of P3HT-SH with the metallic surface of a Au NR.

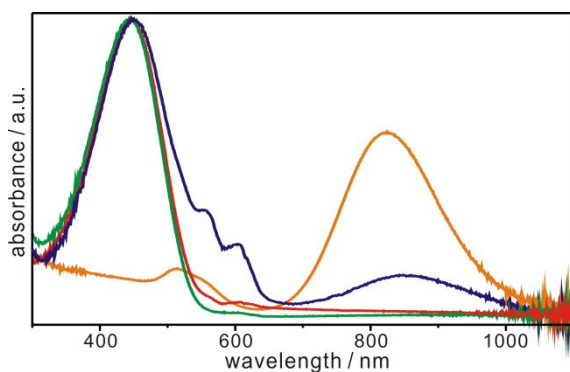


**Figure 3-3.** Absorption spectra of pristine P3HT in THF (red), Au-NS@P3HT nanocomposites in THF (green), Au-NR@P3HT nanocomposites in THF (blue), and CTAB-stabilized Au NRs in water (orange).

Figure 3-3 shows that each of the absorption spectra of pristine P3HT, Au-NS@P3HT nanocomposites, and Au-NR@P3HT nanocomposites in THF has a broad featureless band with the maximum around 450 nm, which arises from the characteristic intrachain  $\pi$ - $\pi$  transition of P3HT. The absorption maximum of the longitudinal SPRs of Au-NR@P3HT composites in THF has been observed to shift to the red by 42 nm from that of Au NRs in water due to the polarity decrease of the medium that surrounds Au NRs. Especially, unlike the absorption spectrum of pristine P3HT in THF, the absorption spectrum of Au-NR@P3HT nanocomposites in THF has two characteristic bands around 600 nm. This result also suggests that the thiol group of a P3HT-SH chain strongly binds chemically to the surface of the Au NR (see below).

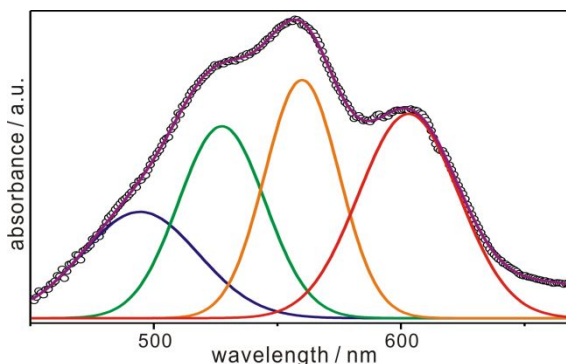


**Figure 3-4.** Difference absorption spectrum in the range of 450 nm to 670 nm (black circles) obtained by subtracting the red curve of pristine P3HT from the blue curve of Au-NR@P3HT nanocomposites in Figure 3-3, fitted with four Gaussian curves of  $\lambda_1$  (blue),  $\lambda_2$  (green),  $\lambda_3$  (orange), and  $\lambda_4$  (red); the violet curve represents the sum of four fitted curves.

**Table 3-2. Spectral Positions of Four Gaussian Curves Fitted to Subtracted Absorption Spectrum of Figure 3-4**

$\lambda_1$ (nm)	$\lambda_2$ (nm)	$\lambda_3$ (nm)	$\lambda_4$ (nm)
494±27 (19%) <sup>a</sup>	527±20 (24%)	559±17 (26%)	603±23 (31%)

<sup>a</sup>Absorbance percentage of each curve.

To have an insight into the effect of chemical-bond interactions between the thiol group of P3HT-SH and the metallic surface of Au NRs on the photophysical properties of Au-NR@P3HT nanocomposites, we have obtained the difference absorption spectrum of Figure S3-2. The appearance of absorption peaks in a low-energy region is a general phenomenon in aggregate P3HT systems having strong intrachain and interchain interactions. As shown in Figure 3-4 and Table 3-2, the difference absorption spectrum in the range of 450 nm to 670 nm can be deconvoluted into four bands having the maxima at 494 ( $\lambda_1$ ), 527 ( $\lambda_2$ ), 559 ( $\lambda_3$ ), and 603 nm ( $\lambda_4$ ). While the  $\lambda_1$  curve arises from the transition of amorphous chains, the  $\lambda_2$ ,  $\lambda_3$ , and  $\lambda_4$  curves

originate from the 0-2, 0-1, and 0-0 transitions, respectively, of aggregated P3HT chains. In other words, although the chemical-bond interactions of the thiol group of P3HT-SH with the metallic surface of Au NSs also exist within Au-NS@P3HT nanocomposites, any absorption peaks originating from aggregated P3HT chains have not been observed in the absorption spectrum of Au-NS@P3HT nanocomposites. This result suggests that compared with P3HT chains attached to Au NSs, P3HT chains bound to Au NRs are much more aggregated.

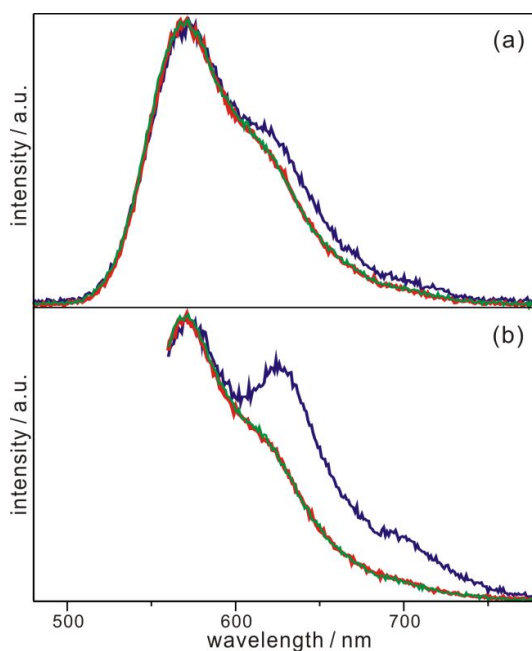


**Figure 3-5.** Emission spectra of pristine P3HT (red), Au-NS@P3HT nanocomposites (green), and Au-NR@P3HT nanocomposites (blue) dispersed in THF, with excitation at 355 nm (a) and 532 nm (b).

Like the absorption spectra, the emission spectra of Au-NR@P3HT nanocomposites in Figure 3-5 also show that the thiol group of P3HT-SH

chains strongly binds chemically to the surface of Au NR. A shoulder around 620 nm in the emission spectrum of Au-NR@P3HT nanocomposites arising from vibronic transitions related to the strong chain-stretching and torsional-twisting motions of P3HT chains is much stronger than that of pristine P3HT or Au-NS@P3HT nanocomposites (Figure 3-5a). In addition, we have also obtained the emission spectra of three respective samples with excitation at 532 nm (Figure 3-5b). The shoulder around 620 nm and the tail around 700 nm are more eminently protrudent in the emission spectrum of Au-NR@P3HT nanocomposites with excitation at 532 nm than in the spectrum with excitation at 355 nm, demonstrating clearly that P3HT chains are evidently aggregated on the surface of Au NRs.

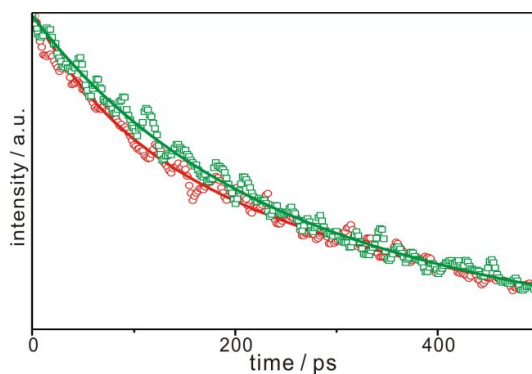


**Figure 3-6.** Emission kinetic profiles of pristine P3HT (red) and Au-NR@P3HT nanocomposites (green) dissolved in THF, monitored at 580 nm after excitation at 355 nm. Solid lines are best-fitted curves to extract kinetic constants.

**Table 3-3. Emission and Transient-Absorption Kinetic Constants of Pristine P3HT and Au-NR@P3HT Nanocomposites in THF**

method	sample	decay time (ps)
picosecond emission <sup>a</sup>	pristine P3HT	80 (30%) + 420 (70%) <sup>b</sup>
	Au-NR@P3HT	155 (40%) + 470 (60%)
nanosecond absorption <sup>c</sup>	pristine P3HT	217,000
	Au-NR@P3HT	226,000

<sup>a</sup>Excited at 355 nm and monitored at 580 nm. <sup>b</sup>Initial intensity percentage of each component. <sup>c</sup>Excited at 355 nm and probed at 820 nm.

Each emission decay kinetic profile of pristine P3HT and Au-NR@P3HT nanocomposites in Figure 3-6 has been deconvoluted into two decay components (Table 3-3). We have assigned the shorter decay component to the intra or interchain energy transfer of the first-excited singlet state ( $S_1$ ) and the longer decay component to the decay of the relaxed  $S_1$  excitons.<sup>27</sup> The intensity percentage of the energy transfer component has been found to be significantly larger in Au-NR@P3HT nanocomposites than in pristine P3HT, as chemical-bond interactions exist between the thiol group and the metallic surface of the nanocomposites. However, because the stretched-strand conformation of P3HT chains attached to Au NRs makes structural relaxation more difficult, the decay time constant of the shorter component is even slowed down drastically by the presence of Au NRs. These results also support that P3HT chains are rigidly bound in parallel, as presented in Scheme 3-1, suggesting strong interchain or intrachain aggregation interactions in Au-NR@P3HT nanocomposites.

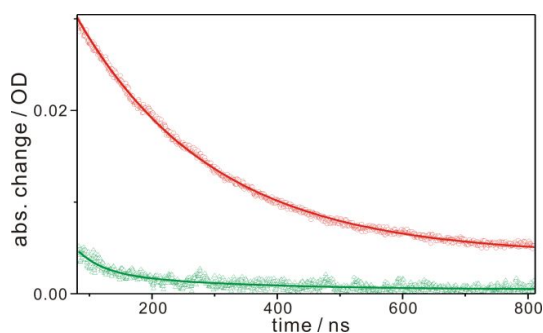


**Figure 3-7.** Nanosecond transient-absorption kinetic profiles of pristine P3HT (red) and Au-NR@P3HT nanocomposites (green) dissolved in THF, probed at 820 nm after excitation at 355 nm. Solid lines are best-fitted curves to extract kinetic constants.

Each nanosecond transient-absorption kinetic profile of pristine P3HT and Au-NR@P3HT nanocomposites dissolved in THF (Figure 3-7) has been deconvoluted into a single decay component of  $\sim 220$  ns (Table 3-3). We have assigned the observed decay time to the lifetime of triplet-state ( $T_1$ ) excitons.<sup>26</sup>  $T_1$  excitons decay more slowly in Au-NR@P3HT nanocomposites than in pristine P3HT due to the stretched-strand conformation of P3HT chains bound to Au NRs. The amplitude of  $T_1$  absorption is much smaller in Au-NR@P3HT nanocomposites than in pristine P3HT. This indicates that the intersystem crossing of  $S_1$  excitons into  $T_1$  excitons does not occur efficiently in Au-NR@P3HT nanocomposites due to the nonflexible character of aggregated P3HT chains.

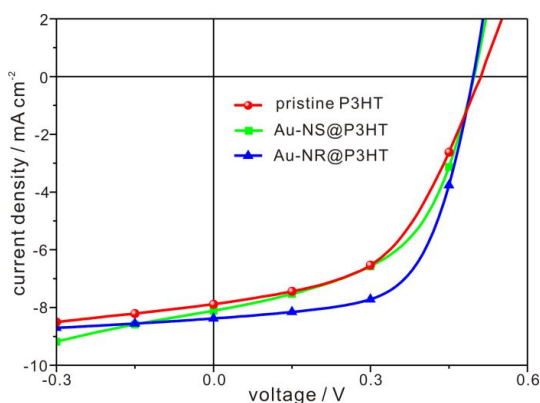


**Figure 3-8.**  $J$ - $V$  curves of P3HT/PCBM photovoltaic devices with different additives in the active layer.

**Table 3-4. Photovoltaic Operation Parameters of P3HT/PCBM Devices with Different Additives in the Active Layer**

sample <sup>a</sup>	$V_{OC}$ (V)	$J_{SC}$ (mA cm <sup>-2</sup> )	FF (%)	PCE (%)
pristine P3HT	0.51	7.88	0.50	2.02
Au-NS@P3HT	0.50	8.11	0.52	2.11
Au-NR@P3HT	0.50	8.38	0.61	2.56

<sup>a</sup>P3HT-functionalized Au NPs (3%) embedded into the P3HT of the active layer.

Figure 3-8 shows the current density-voltage ( $J$ - $V$ ) characteristic curves of optimized devices under  $100 \text{ mW cm}^{-2}$  and AM 1.5G solar illumination, and Table 3-4 indicates that the photovoltaic operation parameters such as the short-circuit current density ( $J_{sc}$ ), the fill factor (FF), and the power conversion efficiency (PCE), obtained from the  $J$ - $V$  characteristic curves of Figure 3-8, have been improved significantly with the addition of Au-NS@P3HT and Au-NR@P3HT nanocomposites into the active layer. The enhancement of PCE with the addition of nanocomposites containing Au NPs into the active layer can be attributed to the fact that the SPRs of Au NPs increase the degree of light absorption and, thereby,

enhance the exciton generation rate.<sup>31,33</sup> In addition, our incorporation of Au NPs into the P3HT matrix reduces the geminate recombination of excitons and increases the probability of exciton dissociation.<sup>31</sup> The increase of exciton dissociation *via* the decrease of exciton recombination by the presence of Au NPs would enhance both the  $J_{sc}$  and FF of organic photovoltaic devices.<sup>7,31</sup> In particular, as compared with the device with the pristine P3HT active layer, the device with the 3% embedding of Au-NR@P3HT nanocomposites into the active layer shows highly improved photovoltaic performances (27% enhancement in PCE). Because the weight ratio of Au NRs to P3HT in Au-NR@P3HT nanocomposites has been found to be  $5.6 \times 10^{-4}$ , the 3% addition of Au-NR@P3HT nanocomposites into the P3HT matrix of the active layer corresponds to the 17 ppm doping of Au into P3HT. The notable PCE enhancement of 27% by the 17 ppm addition of Au into the P3HT matrix suggests that the probability of charge transfer to the conduction band of the PCBM acceptor is increased substantially by the stretched-strand conformation of P3HT chains attached to Au NRs,<sup>31</sup> which makes intra or interchain interactions more efficient in Au-NR@P3HT nanocomposites.

### **3. 5. Conclusions**

Poly(3-hexylthiophene)-stabilized gold nanorods (Au-NR@P3HT nanocomposites) have been facilely fabricated by incubating Au nanorods (NRs) with thiol-terminated P3HT to investigate the effects of Au NRs on the excited-state dynamics

and photovoltaic performances of P3HT. In Au-NR@P3HT nanocomposites, each Au NR is surrounded by  $3.4 \times 10^4$  P3HT chains and the weight ratio of Au NRs to P3HT chains has been found to be  $5.6 \times 10^{-4}$ . In static emission spectra, a shoulder around 620 nm in the emission spectrum of Au-NR@P3HT nanocomposites arising from vibronic transitions related to the strong chain-stretching and torsional-twisting motions of P3HT chains is much stronger than that of pristine P3HT or P3HT-stabilized gold nanospheres (Au-NS@P3HT nanocomposites). The  $S_1$  decay of Au-NR@P3HT nanocomposites is found to be slower than that of pristine P3HT, suggesting that the stretched-strand conformation of P3HT chains attached to Au NRs makes structural relaxation more difficult. The amplitude of  $T_1$  absorption is much smaller in Au-NR@P3HT nanocomposites than in pristine P3HT, indicating that the intersystem crossing of  $S_1$  excitons into  $T_1$  excitons does not occur efficiently in Au-NR@P3HT nanocomposites due to the nonflexible character of aggregated P3HT chains. From the comparison of the performances of organic photovoltaic devices prepared with and without Au-NS@P3HT and Au-NR@P3HT nanocomposites in the P3HT matrix of the active layer, the enhancement of PCE with the addition of nanocomposites containing Au NPs into the active layer has suggested that the SPRs of Au NPs increase the degree of light absorption and, thereby, enhance the exciton generation rate. Especially, the device with the 3% embedding of Au-NR@P3HT nanocomposites into the P3HT matrix of the active layer, the 17 ppm doping of Au into P3HT, shows significantly improved photovoltaic performances (27% enhancement in PCE).

### 3. 6. References

- (1) Kaushik, A.; Kumar, R.; Arya, S. K.; Nair, M.; Malhotra, B.; Bhansali, S. *Chem. Rev.* **2015**, *115*, 4571-4606.
- (2) Yin, P. T.; Shah, S.; Chhowalla, M.; Lee, K.-B. *Chem. Rev.* **2015**, *115*, 2483-2531.
- (3) Stratakis, E.; Kymakis, E. *Mater. Today* **2013**, *16*, 133–146.
- (4) Liao, H.-C.; Tsao, C.-S.; Lin, T.-H.; Jao, M.-H.; Chuang, C.-M.; Chang, S.-Y.; Huang, Y.-C.; Shao, Y.-T.; Chen, C.-Y.; Su, C.-J. *ACS nano* **2012**, *6*, 1657-1666.
- (5) Reiss, P.; Couderc, E; De Girolamo, J.; Pron, A. *Nanoscale* **2011**, *3*, 446–489.
- (6) Goodman, M. D.; Xu, J.; Wang, J.; Lin, Z. *Chem. Mater.* **2009**, *21*, 934-938.
- (7) Kim, K.; Carrola, D. L. *Appl. Phys. Lett.* **2005**, *87*, 203113.
- (8) (a) Sun, B.; Marx, E.; Greenham, N. C. *Nano Lett.* **2003**, *3*, 961-963. (b) Yen, W.-C.; Lee, Y.-H.; Lin, J.-F.; Dai, C.-A.; Jeng, U.-S.; Su, W.-F. *Langmuir* **2011**, *27*, 109-115.
- (9) (a) Wuelfing, W. P.; Gross, S. M.; Miles, D. T.; Murray, R. W. *J. Am. Chem. Soc.* **1998**, *120*, 12696-12697. (b) Corbierre, M. K.; Cameron, N. S.; Lennox, R. B. *Langmuir* **2004**, *20*, 2867-2873.
- (10) Scharber, M. C.; Mühlbacher, D.; Koppe, M.; Denk, P.; Waldauf, C.; Heeger, A. J.; Brabec, C. J. *Adv. Mater.* **2006**, *18*, 789-794.

- (11) Hains, A. W.; Liang, Z.; Woodhouse, M. A.; Gregg, B. A. *Chem. Rev.* **2010**, *110*, 6689-6735.
- (12) Lubber, E. J.; Buriak, J. M. *ACS Nano* **2013**, *7*, 4708-4714.
- (13) Coakley, K. M.; McGehee, M. D. *Chem. Mater.* **2004**, *16*, 4533-4542.
- (14) Facchetti, A. *Chem. Mater.* **2011**, *23*, 733-758.
- (15) Fischer, F. S. U.; Tremel, K.; Saur, A.-K.; Link, S.; Kayunkid, N.; Brinkmann, M.; Herrero-Carvajal, D.; López Navarrete, J. T.; Ruiz Delgado, M. C.; Ludwigs, S. *Macromolecules* **2013**, *46*, 4924-4931.
- (16) Mao, Z.; Vakhshouri, K.; Jaye, C.; Fischer, D. A.; Fernando, R.; DeLongchamp, D. M.; Gomez, E. D.; Sauv e, G. *Macromolecules* **2013**, *46*, 103-112.
- (17) Lombardo, C. J.; Danielson, E. L.; Glaz, M. S.; Ooi, Z.-E.; Vanden Bout, D. A.; Dodabalapur, A. *J. Phys. Chem. B* **2013**, *117*, 4503-4509.
- (18) Shen, H.; Bienstman, P.; Maes, B. *J. Appl. Phys.* **2009**, *106*, 073109.
- (19) Kim, S. J.; Ah, C. S.; Jang, D.-J. *J. Nanopart. Res.* **2009**, *11*, 2023-2030.
- (20) Kim, J.-Y.; Kim, S. J.; Jang, D.-J. *J. Phys. Chem. C* **2011**, *115*, 672-675.
- (21) Chon, J. W. M.; Bullen, C.; Zijlstra, P.; Gu, M. *Adv. Funct. Mater.* **2007**, *17*, 875-880.
- (22) Choi, W.; Sahu, A.; Kim, Y.; Tae, G. *Ann. Biomed. Eng.* **2012**, *40*, 534-546.
- (23) (a) Son, M.; Jeong, S.; Jang, D.-J. *J. Phys. Chem. C* **2014**, *118*, 5961-5967. (b) Orendorff, C. J.; Murphy, C. J. *J. Phys. Chem. B* **2006**, *110*, 3990-3994.
- (24) Banerji, N.; Cowan, S.; Vauthey, E.; Heeger, A. J. *J. Phys. Chem. C* **2011**,

115, 9726-9739.

- (25) Banerji, N.; Seifert, J.; Wang, M.; Vauthey, E.; Wudl, F.; Heeger, A. J. *Phys. Rev. B* **2011**, *84*, 075206.
- (26) Cook, S.; Furube, A.; Katoh, R. *Energ. Environ. Sci.* **2008**, *1*, 294-299.
- (27) (a) Ferreira, B.; da Silva, P. F.; Seixas de Melo, J. S.; Pina, J.; Maçanita, A. *J. Phys. Chem. B* **2012**, *116*, 2347-2355. (b) Lee, D.; Jang, D.-J. *Polymer* **2014**, *55*, 5469-5476.
- (28) Busby, E.; Carroll, E. C.; Chinn, E. M.; Chang, L.; Moulé, A. J.; Larsen, D. *S. J. Phys. Chem. Lett.* **2011**, *2*, 2764-2769.
- (29) (a) Guo, J.; Ohkita, H.; Bente, H.; Ito, S. *J. Am. Chem. Soc.* **2010**, *132*, 6154-6164. (b) Lee, D.; Lee, J.; Song, K.-H.; Rhee, H.; Jang, D.-J. *Phys. Chem. Chem. Phys.* **2016**, *18*, 2087-2096.
- (30) Guo, J.; Ohkita, H.; Bente, H.; Ito, S. *J. Am. Chem. Soc.* **2009**, *131*, 16869-16880.
- (31) Wu, J.-L.; Chen, F.-C.; Hsiao, Y.-S.; Chien, F.-C.; Chen, P.; Kuo, C.-H.; Huang, M. H.; Hsu, C.-S. *ACS Nano* **2011**, *5*, 959-967.
- (32) (a) Nie, Z.; Fava, D.; Kumacheva, E.; Zou, S.; Walker, G. C.; Rubinstein, M. *Nat. Mater.* **2007**, *6*, 609-614. (b) Kim, H.; Lim, Y.; Kim, S.; Kim, S.-S.; Sohn, B.-H. *Nanotechnology* **2014**, *25*, 455602.
- (33) Nicholson, P. G.; Ruiz, V.; Macpherson, J. V.; Unwin, P. R. *Chem. Commun.* **2005**, 1052-1054.

### 3.7. Supporting Information

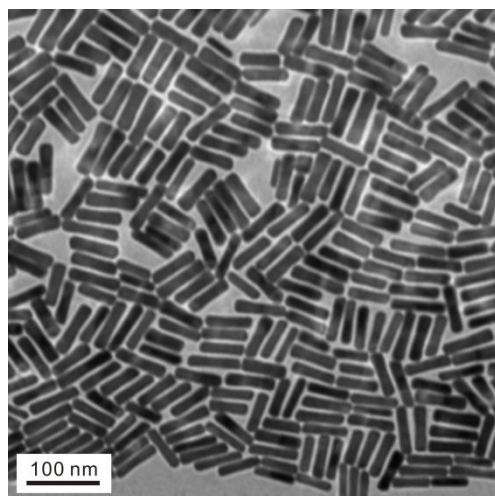


**Figure S3-1.** TEM image of Au NRs.

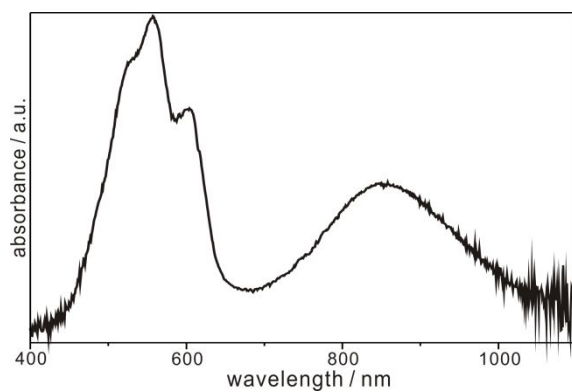


**Figure S3-2.** Difference absorption spectrum obtained by subtracting the red curve of pristine P3HT from the blue curve of Au-NR@P3HT nanocomposites in Figure 3-3.

## **Chapter 4. Formation and Decay of Charge Carriers in Aggregate Nanofibers Consisting of P3HT-Coated Gold Nanoparticles†**

†This is reproduced from Dongki Lee, Jaewon Lee, Ki-Hee Song, Hanju Rhee, and Du-Jeon Jang, *Phys. Chem. Chem. Phys.* **2016**, *18*, 2087. © The Royal Society of Chemistry 2016.

#### 4. 1. Abstract

Thin nanofibers (NFs) of J- dominant aggregates having thickness of 15 nm and thick NFs of H-dominant aggregates having thickness of 25 nm have been fabricated by self-assembling poly(3-hexylthiophene)-coated gold nanoparticles. The formation and decay dynamics of charge carriers, which are dependent on the aggregate types of NFs, has been investigated by time-resolved emission and transient-absorption spectroscopy. With increasing excitation energy, the fraction of the fast emission decay component has been found to decrease, suggesting that the fast formation of polaron pairs (PP), localized (LP), and delocalized polarons (DP) results from higher singlet exciton states produced by the singlet fusion. The faster decay dynamics of DP and LP in thick NFs than in thin NFs is due to the increased delocalization of DP and LP. As interchain aggregation is weaker than intrachain aggregation, PP decays faster in thin NFs than in thick NFs. In both thin and thick NFs, whereas triplet ( $T_1$ ) excitons have been hardly observed with excitation at 532 nm on a nanosecond time scale, they have been observed with excitation at 355 nm, revealing that  $T_1$  excitons within NFs are mainly generated through the singlet fission from a higher singlet exciton state rather than through intersystem crossing.

## 4. 2. Introduction

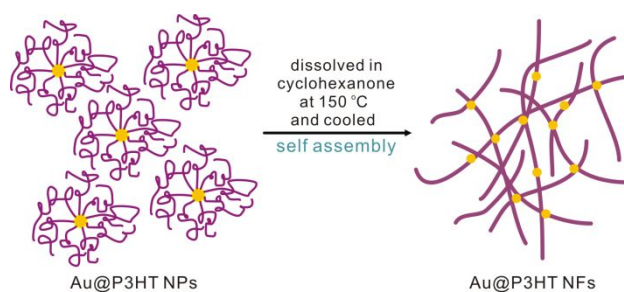
The design and controlled fabrication of nanostructured materials having functional properties have been extensively studied.<sup>1-4</sup> In particular, hybrid nanocomposites consisting of conjugated polymers and inorganic materials have received intense attention for applications in optoelectronic devices such as light-emitting diodes, biosensors, and photovoltaic cells because of their ability to provide diverse opportunities for the development of novel nanomaterials having improved physical and chemical properties against single-component counterparts.<sup>5-8</sup> Among numerous conjugated polymers, poly(3-hexylthiophene) (P3HT), which is most commonly used in optoelectronic devices, has been extensively studied because of its facilely tunable optical and electrical properties controlled by regulating the conformation, packing, and morphology of individual chains.<sup>9-12</sup> The modification of the hexyl substitution changes the solubility of the polymer to make P3HT self-assembled into a two-dimensional high-interchain lamella with favorable head-to-head (HH) coupling or into a one-dimensional (1D) high-intrachain nanostructure with unfavorable HH coupling, depending on diverse formation conditions such as the degree of regioregularity<sup>13-15</sup> and the types of solvents.<sup>16-19</sup> Especially, since 1D nanostructures, namely nanofibers (NFs), of P3HT have good advantages such as large surface areas and 1D path ways at the nanosized level for the migration of charge carriers, they are expected to have improved optoelectronic device performances.<sup>20-24</sup> The dynamics of charge carriers generated from the excited states of P3HT within NFs plays an important role on device performances and is heavily

influenced by conformational behaviors of P3HT chains. Therefore, not only a fundamental understanding of the photophysics of non-aggregate individual P3HT chains but also the comprehensive investigation of photoinduced charge carriers affected by the types of aggregate NFs are critical research points in diverse optoelectronic application fields where P3HT is used.<sup>25-32</sup>

Aggregates of conjugated polymers can be distinguished by two types of fundamental electronic interactions: one occurring within a given chain and the other occurring between chains.<sup>33a</sup> The impact of such excitonic interactions on the photophysics of polymer films can be understood using the concepts of J- and H-aggregation. In polymer assemblies, intrachain head-to-tail (HT) through-bond interactions lead to J-aggregate behaviors, whereas interchain Coulombic HH interactions lead to H-aggregate behaviors.<sup>33</sup> Different coupling types of J- and H-aggregates are readily distinguished by intensity difference between the origin (0–0) transition and the sideband (0–1, or higher) vibronic transitions. When interchain HH order is dominant in H-aggregate NFs, the 0-0 electronic transition is forbidden by symmetry and less intense than the 0-1 vibronic sideband. In contrast, when intrachain HT order is dominant in J-aggregate NFs, the 0-0 transition is allowed and more intense than the 0-1 vibronic sideband.<sup>33-36</sup> In H-aggregate systems, typical in most thin films, the 0–0 transition in emission is weakly allowed due to structural or thermal disorder, and most of the emission intensity is carried in the 0–1 vibronic transition. This gives rise to 0–0/0–1 intensity ratios smaller than 1 for H-aggregate systems. Conversely, the rigid linear arrangement of thiophene units results in dominant intrachain coupling manifested as J-aggregate behaviors, where the 0–0

transition is strongly allowed, thus giving rise to 0–0/0–1 intensity ratios larger than 1.<sup>37,38</sup>

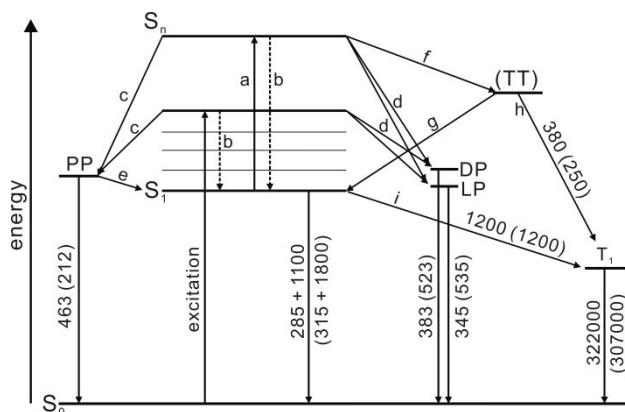
Diverse recent spectroscopic studies on aggregate P3HT systems have shown that the formation and decay of charge carriers such as excitons and polarons are strongly dependent on the aggregate behaviors of P3HT chains.<sup>11-15,34-37,39,40</sup> Grey et al.<sup>11</sup> have demonstrated that a triplet exciton can also form *via* a recombination of long-lived polarons in J-aggregate NFs having high intrachain order. High intrachain order in J-aggregate P3HT NFs facilitates the delocalization of singlet excitons, leading to the eventual formation of triplet excitons *via* the nongeminate recombination of delocalized polaron species. The formation and decay dynamics of triplet excitons and polarons has been reported<sup>13,14</sup> to depend on the regioregularity of P3HT films. Because of strong interchain interactions in regioregular P3HT films, singlet excitons are more delocalized to form interchain excitons, whereas intrachain singlet excitons formed in regiorandom P3HT films are substantially converted to triplet excitons through the singlet fission.<sup>13</sup> Although previous studies<sup>13,14</sup> have provided useful information on charge carriers generated in aggregate P3HT systems, the formation and decay dynamics of charge carriers dependent on aggregate types in aggregate P3HT NFs has not been fully understood over the wide wavelength region from the visible to the near infrared.



**Scheme 4-1. Schematic for the fabrication of Au@P3HT NFs.**

In this paper, we present that NFs with H-dominant and J- dominant aggregates have been fabricated by self-assembling P3HT-coated gold nanoparticles (Au@P3HT NPs) in cyclohexanone (Scheme 4-1 and Figure S4-1). The picosecond dynamics of charge carriers such as singlet ( $S_1$ ) and triplet excitons ( $T_1$ ), polaron pairs (PP), and localized (LP) and delocalized polarons (DP) of H-aggregate-dominant NFs with thickness of 25 nm (thick NFs) and J-aggregate-dominant NFs with thickness of 15 nm (thin NFs) has been also investigated using time-resolved emission and transient-absorption (TA) spectroscopy (Scheme 4-2). To understand the role of gold nanoparticles (Au NPs) within NFs, we have also fabricated pristine NFs using Au NPs-free pristine P3HT *via* the same preparation procedure of thin NFs. The decay time constants of  $S_1$  excitons in thick NFs are found to be smaller than those in thin NFs due to the increase of interchain stacking effects. With increasing excitation energy, the fraction of the fast emission decay component has been found to decrease, suggesting that the fast formation of PP, LP, and DP results from higher singlet exciton states. The faster decay dynamics of LP and DP in thick NFs indicates that the interchain delocalization effect is predominant. However, as interchain aggregation is weaker than intrachain aggregation, PP decays faster in

thin NFs than in thick NFs. In both thin and thick NFs,  $T_1$  excitons were hardly observed with excitation at 532 nm. On the other hand, they have been observed with excitation at 355 nm, revealing that  $T_1$  excitons in NFs mainly arise from the singlet fission of a higher singlet exciton state.



**Scheme 4-2.** Schematic representation for the dynamics of singlet ( $S_1$ ) and triplet excitons ( $T_1$ ), triplet pairs (TT), localized (LP) and delocalized polarons (DP), polaron pairs (PP) in thick (thin) Au@P3HT NFs, where time constants are indicated in the units of ps. Key: <sup>a</sup> singlet fusion, <sup>b</sup> vibrational relaxation, <sup>c</sup> PP formation, <sup>d</sup> P or DP formation, <sup>e</sup> geminate recombination to  $S_1$ , <sup>f</sup> singlet fission, <sup>g</sup> triplet fusion, <sup>h</sup>  $T_1$  formation, and <sup>i</sup> intersystem crossing.

### 4. 3. Experimental Section

**4. 3. 1. Synthesis.** The detailed synthetic and characterization procedures of P3HT-functionalized gold nanoparticles (Au@P3HT NPs) have already been reported.<sup>30</sup> Thin and thick NFs were prepared in a poor solvent *via* a self-assembly process, as described in detail elsewhere.<sup>20,22</sup> For the fabrication of thin NFs, 4.0 mg of Au@P3HT NPs was dissolved in 10 mL of cyclohexanone (l, 99%, Sigma-Aldrich) in a 50 mL three-neck reaction vessel. The colloid was slowly heated to

150 °C and kept in the dark under N<sub>2</sub> atmosphere. The mixture was turned into a homogeneous limpid orange-colored solution and then cooled to room temperature naturally to generate self-assembled NFs. Then, the produced opaque violet-colored colloidal solution was centrifuged for 30 min at 13,500 rpm. The supernatant was discarded and the precipitated NFs were dispersed in 0.5 mL of cyclohexanone. The preparation procedure of thick NFs was the same as that of thin NFs, except that the weight of Au@P3HT NPs was increased three times.

**4. 3. 2. Characterization.** Transmission electron microscopy (TEM) images were obtained with a Hitachi H7600 microscope; a TEM sample was prepared by evaporating and drying a colloidal droplet on a carbon-coated copper grid in an argon glovebox at room temperature. Scanning electron microscopy (SEM) images were obtained with a JEOL-6700F microscope; the same TEM samples were also used for SEM measurements. Atomic force microscopy (AFM) images were obtained with a Veeco Instrument MultiMode 8 and Nanoscope V controller; AFM samples were prepared by spin-coating a colloidal drop for 30 s at 3,000 rpm on highly ordered pyrolytic graphite (HOPG) substrates, and the all images were obtained on tapping modes. While absorption spectra were measured with a Scinco S3100 UV/vis spectrophotometer, emission spectra were obtained using a home-built fluorometer consisting of a 75 W Acton Research XS 432 Xe lamp with an Acton Research Spectrapro150 monochromator of 0.15 m and an Acton Research PD438 photomultiplier tube attached to an Acton Research Spectrapro300 monochromator of 0.30 m.

**4. 3. 3. Transient-Absorption (TA) and Emission Kinetics.** For femtosecond TA measurements, a 40 fs pump beam and a 200 fs probe beam were generated from a non-collinear Light Conversion ORPHEUS-N optical parametric amplifiers (OPA) and a collinear Light Conversion ORPHEUS OPA, respectively, and amplified using a Light Conversion PHAROS Yb:KGW-doped regenerative amplifier with a repetition rate of 1 kHz. The pump was tuned to a fixed wavelength of 355 nm and the probe over a wide wavelength region from the visible to the near infrared. Time delays between the pump and the probe pulses were controlled with a Newport M-ILS150CC motorized linear delay stage. Whereas both the pump (10 nJ) and the probe (1 nJ) pulses were focused into a sample by a CaF<sub>2</sub> lens with a focal length of 10 cm, only the probe beam was then detected by a Si 350-1100 nm photodiode with the pump blocked. The pump and the probe polarizations were set to be the same. To remove light scattered from the pump beam and the residual second harmonic of the probe beam, long-pass filters with variable-wavelength cut-off filters were used in front of the detector. For the phase-sensitive detection of the pump-induced TA signal, the pump beam was modulated by an optical chopper synchronized at a sub-harmonic frequency (500 Hz) of the laser repetition rate and the modulated probe signal was finally recorded at a Stanford Research Systems SR830 lock-in amplifier *via* a Stanford Research Systems SR250 gated integrator.

Nanosecond TA kinetic profiles were obtained by monitoring the beam intensity of a 75 W Acton Research XS 432 Xe lamp after being transmitted through a sample, which was excited with 355 or 532 nm pulses having a duration time of 6 ns from a Q-switched Quantel Brilliant Nd:YAG laser. The wavelength of

the probe beam was selected using an Acton Research Spectrapro150 monochromator of 0.15 m and a Kratos GM 200 double monochromator of 0.2 m. The probe beam was detected with a Hamamatsu R928 PMT and digitized with a Lecroy Wavepro 950 oscilloscope of 1 GHz. The laser and the oscilloscope were triggered with variable delays using a Stanford Research Systems DG535 pulse/delay generator.

Picosecond emission kinetic profiles with excitation of 355 or 532 nm pulses from a mode-locked Quantel YG901-10 Nd:YAG laser of 25 ps were detected using a Hamamatsu C2830 streak camera of 10 ps attached to a Princeton Instruments RTE128H CCD detector. Emission wavelengths were selected using combined band-pass and cut-off filters. Emission and TA kinetic constants were extracted by fitting measured kinetic profiles to computer-simulated kinetic curves convoluted with instrument temporal response functions.

#### 4. 4. Results and Discussion

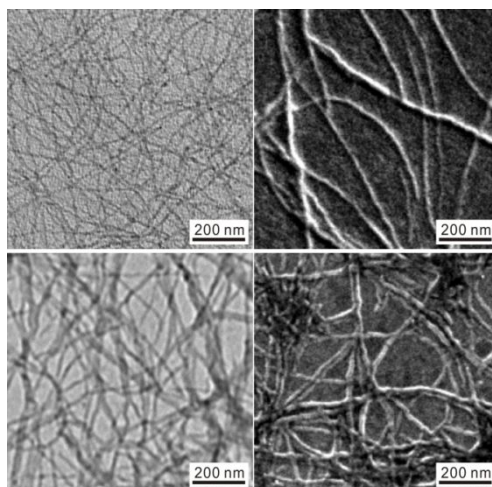


**Figure 4-1.** TEM (left) and SEM images (right) of thin (top) and thick NFs (bottom).

TEM and SEM images of thin and thick NFs prepared by evaporating a droplet of dilute thin or thick NFs dispersed in cyclohexanone on a carbon-coated copper grid are shown in Figure 4-1. AFM images of thin and thick NFs are also shown in Figure S4-2. The morphology of thin NFs has the network structure of silk fibers with thickness of  $15\pm 2$  nm, whereas that of thick NFs has the network structure of blood vessels with thickness of  $25\pm 6$  nm. As shown in Figure S4-1, the formation mechanisms of NFs have been proposed to depend on two critical factors: the concentration of Au@P3HT NPs in cyclohexanone and the chemical-bond interactions of thiol-terminated P3HT (P3HT-SH) with gold NPs.<sup>30</sup> With the concentration increase of Au@P3HT NPs in cyclohexanone, the thickness of NFs increases and the morphology of NFs becomes more complicated, suggesting that the dominant tendency of aggregation during the formation of NFs changes from a

intrachain aggregate along the transverse axis into a interchain aggregate along the longitudinal axis. As a result, thin NFs having thickness of  $15\pm 2$  nm have been predominantly formed along the transverse axis at a low concentration to have folded or extended polymer backbones extensively. On the other hand, thick NFs having thickness of  $25\pm 6$  nm have been prevalingly formed along the longitudinal axis at a high concentration to have stacked polymer backbones abundantly. The formation kinetics of NFs as well as the molecular weight ( $M_n$ ) of P3HT has been reported to play an important role in determining the dominant coupling types of aggregate P3HT NFs during the formation of NFs.<sup>11,34</sup> The rapid formation kinetics of NFs in a poor solvent such as anisole promotes H-type NFs, whereas the slow self-assembly process of P3HT chains over several days in toluene cultivates J-type NFs.<sup>11</sup> In the low  $M_n$  condition, H-type NFs are predominantly formed, and in the high  $M_n$  condition, J-type NFs are prevalently produced.<sup>34</sup> In our formation conditions of NFs, although we have chosen the rapid formation kinetics in a poor solvent such as cyclohexanone and P3HT-attached gold NPs having low  $M_n$  ( $10,565$  g mol<sup>-1</sup>),<sup>30</sup> J-aggregate-dominant NFs have been abundantly formed in the low-concentration condition due to strong chemical-bond interactions between P3HT-SH and gold NPs, inducing the transverse aggregation rather than the longitudinal aggregation. Since the effect of chemical-bond interactions competes with the concentration effect of Au@P3HT NPs in the high-concentration condition, the longitudinal aggregation becomes as important as the transvers aggregation in the formation of thick NFs. Consequently, the thickness of NFs associated with transition in dominant exciton coupling from intrachain coupling to interchain

coupling in NFs has been facilyly tuned *via* controlling the concentration of Au@P3HT NPs in cyclohexanone, producing stable and well-ordered NFs with H-dominant and J-dominant aggregates homogeneously at the molecular level.

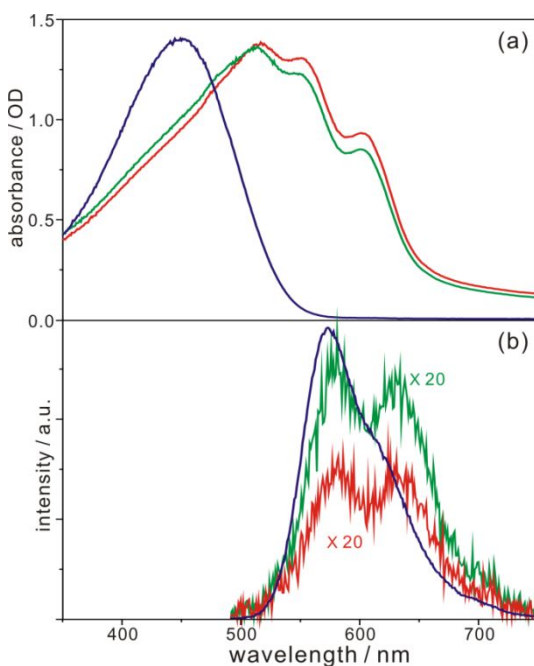


**Figure 4-2.** Absorption (a) and emission spectra (b) of non-aggregate Au@P3HT NPs in chloroform (blue), thin NFs in cyclohexanone (green), and thick NFs in cyclohexanone (red). Samples were excited at 355 nm for the emission spectra.

Figure 4-2a shows that the absorption spectra of thin and thick NFs in cyclohexanone are considerably different from the absorption spectrum of non-aggregated Au@P3HT NPs in chloroform. The absorption maxima of thin and thick NFs in cyclohexanone have been observed to shift to the red by 60 and 64 nm, respectively, from that of Au@P3HT NPs in chloroform due to the increased conjugation length of intrachain or interchain  $\pi$ - $\pi$  transition in

aggregated P3HT backbones.<sup>11,12,30,34-40</sup> Based on previous studies,<sup>16,34</sup> each absorption spectrum of thin and thick NFs in Figure S4-3 has been deconvoluted into five bands having the maxima at 448 (violet), 486 (blue), 523 (green), 559 (yellow), and 604 nm (red), as given in Table S4-1. The deconvoluted absorption spectrum of thin or thick NFs consists of two parts: a high-energy region of the violet and blue bands arising from the transition of free or amorphous chains and a low-energy region of the green, yellow, and red bands originating from the 0-2 ( $A_{0-2}$ ), 0-1 ( $A_{0-1}$ ), and 0-0 vibronic transitions ( $A_{0-0}$ ), respectively, of aggregated chains.<sup>16</sup>

Information on the dominant coupling type, H-type (interchain aggregate) or J-type (intrachain aggregate) is related to the intensity ratio of the origin (0-0) and the first-vibronic (0-1) transitions according to eq 1<sup>16,33,35a</sup>

$$\frac{A_{0-0}}{A_{0-1}} = \left( \frac{1 - 0.24W / \omega_0}{1 + 0.073W / \omega_0} \right)^2 \quad (1)$$

where  $W$  is the exciton bandwidth and  $\omega_0$  is the vibrational energy of the symmetric vinyl stretch. Since the exciton bandwidth is related to the strength of excitonic coupling between neighboring chains, the dominant coupling type of NFs can be readily figured out by intensity difference between the 0-0 and the 0-1 vibronic transitions of absorption spectra. The 0-0 transition and the 0-1 vibronic transition within aggregated NFs are restrained by selection rules. In H-type NFs, the 0-0 transition is forbidden because antiparallel transition dipole moments ( $\Sigma\mu = 0$ ) are formed in the lower of two excited states. However, the 0-1 vibronic transition is allowed because parallel

transition dipole moments ( $\Sigma\mu \neq 0$ ) are formed in the higher of two excited states. On the other hand, the 0-0 transition is allowed in J-type NFs since head-to-tail aggregation causes parallel dipole moments ( $\Sigma\mu \neq 0$ ) in the lower of two excited states. Because antiparallel transition dipole moments ( $\Sigma\mu = 0$ ) are formed in the higher of two excited states, the 0-1 transition is forbidden in J-type NFs.<sup>33-36,38</sup>

The apparent absorbance ratio,  $A_{0-0}/A_{0-1}$ , of the 0-0 transition to the 0-1 vibronic transition in thin NFs (2.3) is 1.9 times greater than that in thick NFs (1.2) (Table S4-1). As discussed in the formation mechanisms of NFs (Figure S4-1), the intrachain-aggregation effect is predominant in the low-concentration condition, resulting in J-aggregate-dominant NFs (thin NFs), whereas the interchain-aggregation effect is competitive in the high-concentration condition, resulting in H-aggregate-dominant NFs (thick NFs). Thus, the absorption spectra of NFs in Figure 4-2a also support that the J-aggregate character is predominant in thin NFs due to the effect of intrachain aggregation along the transverse axis, whereas the H-aggregate character becomes as important as the J-aggregate character in thick NFs due to the increase of interchain interactions along the longitudinal axis between neighboring chains. To understand the role of Au NPs within NFs, we have also fabricated pristine NFs using Au NPs-free pristine P3HT via the same preparation procedure of thin NFs. The absorption spectra of Figure S4-4, as well as Table S4-1, show increased absorption around 480 nm for pristine NFs, suggesting that the structure of pristine NFs is more amorphous than that

of thin NFs because the chemical-bond interactions of P3HT-SH with gold NPs inducing highly transverse aggregation do not exist.

As shown in Figure 4-2b, unlike the emission spectrum of non-aggregated Au@P3HT NPs in chloroform, each emission spectrum of thin and thick NFs in cyclohexanone has two characteristic bands at 650 and 690 nm and the emission intensity of NFs is ~20 times weaker than that of NPs. The drastic quenching of emission is indicative of the existence of well-ordered aggregated P3HT chains and strong exciton coupling in NFs. The emission spectra of aggregate P3HT NFs with two featured peaks, the 0-0 transition at 650 nm and the 0-1 vibronic transition at 690 nm, have been numerously investigated<sup>33-40</sup> to distinguish the dominant coupling type.

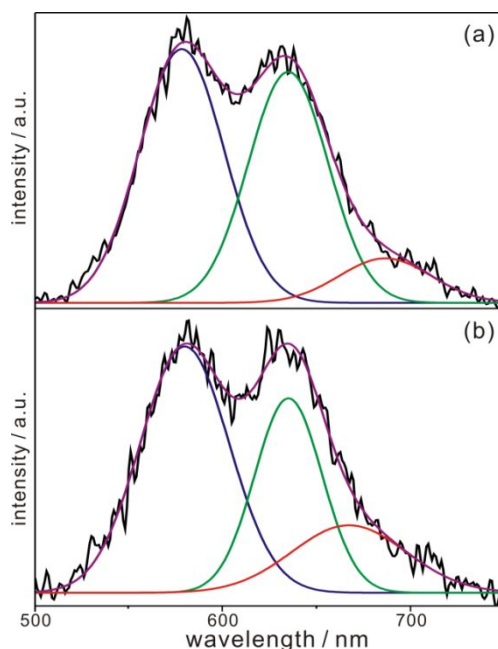


**Figure 4-3.** Emission spectra (black) of thin (a) and thick NFs (b) in cyclohexanone with excitation at 355 nm, fitted with three Gaussian curves  $\lambda_1$  (blue),  $\lambda_2$  (green), and  $\lambda_3$  (red); violet curves represent the sum of the three fitted curves.

Figure 4-3 shows that each emission spectrum of thin and thick NFs with excitation at 355 nm has been deconvoluted into three Gaussian curves having the maxima at 579 (blue), 635 (green), and 677 nm (red), as given in Table 4-1. The blue curves are ascribed to the recombination of relaxed  $S_1$  excitons to the ground state of free or amorphous chains. On the other hand, the green curves are attributed to transition from the lowest-excited singlet state to the lowest vibrational level of the ground state (0-0 transition) of aggregated chains, and the red curves are due to transition from the lowest-excited singlet state to the first-excited vibrational level of the ground state (0-1 transition) of aggregated chains.<sup>33,34,38</sup> As mentioned with the absorption spectra of NFs, the dominant coupling type of NFs can be also easily figured

out by intensity difference between the 0-0 transition and the 0-1 vibronic transition of emission spectra.<sup>34,35</sup> It has been reported<sup>34</sup> that the  $I_{em}^{0-0}/I_{em}^{0-1}$  value of 65 kDa P3HT NFs having the strong J-type coupling is 1.8 while the value of 13 kDa P3HT NFs having the weak H-type coupling is 0.88. In our NFs, the apparent  $I_{em}^{0-0}/I_{em}^{0-1}$  of thin NFs (4.2) is 2.5 times greater than that of thick NFs (1.7). Like the absorption spectra, this result also strongly supports that the J-aggregate character is predominant in thin NFs due to the effect of intrachain aggregation along the transverse axis, whereas the H-aggregate character becomes as important as the J-aggregate character in thick NFs due to the increase of interchain interactions along the longitudinal axis between neighboring chains. Figure S4-5 shows that the 0-0 and the 0-1 transitions of aggregated chains around 630 and 690 nm, respectively, are much weaker than the respective ones of thin NFs due to the amorphous structure of pristine NFs, as discussed with the absorption spectra of Figure S4-4.

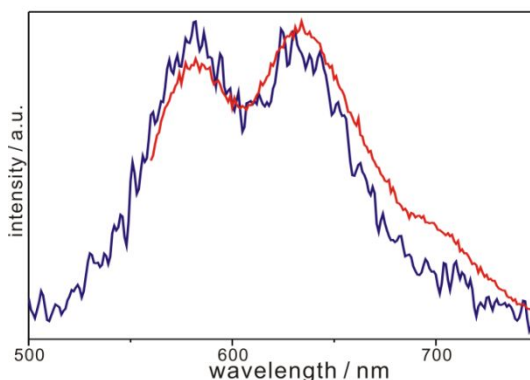


**Figure 4-4.** Emission spectra of thick NFs (b) in cyclohexanone with excitation at 355 (blue) and 532 nm (red).

**Table 4-1. Three Gaussian Curves Fitted to Each Emission Spectrum of NFs Dispersed in Cyclohexanone**

sample	$\lambda_{\text{ex}}$ (nm)	$\lambda_1^{\text{a}}$ (nm)	$\lambda_2^{\text{b}}$ (nm)	$\lambda_3^{\text{c}}$ (nm)
thin NFs	355	578±27 (48%) <sup>d</sup>	635±25 (42%)	687±29 (10%)
thick NFs		580±28 (51%)	635±21 (31%)	668±36 (18%)
thin NFs	532	577±23 (37%)	632±28 (44%)	689±37 (19%)
thick NFs		578±23 (34%)	632±26 (37%)	683±44 (29%)

<sup>a</sup> Due to the 0-0 transition of free chains. <sup>b</sup> Due to the 0-0 transition of aggregated chains. <sup>c</sup> Due to the 0-1 transition of aggregated chains. <sup>d</sup> Intensity percentage of each curve.

In aggregate P3HT systems such as films and NFs, the excited state is split into two different energy states due to the existence of inter- (H-type) or intrachain (J-type) aggregation.<sup>13,14</sup> Since the excitation energy is another critical factor associated with the formation of the split excited states of NFs,<sup>14,37</sup> we have also obtained the emission spectra of NFs with excitation at 532 nm (Figure S4-6). As shown in Table 4-1 and Figure S4-6, each emission spectrum of both thin and thick NFs in cyclohexanone with excitation at 532 nm has been deconvoluted into three Gaussian curves having the maxima at

577, 632, and 686 nm. With decreasing excitation energy from 3.49 eV (355 nm) to 2.33 eV (532 nm), the intensity fraction of the 0-0 transition of free or amorphous chains has been found to decrease. The  $I_{em}^{0-0}/I_{em}^{0-1}$  of thin NFs (2.3) is 1.8 times greater than that of thick NFs (1.3). In comparison, difference between the  $I_{em}^{0-0}/I_{em}^{0-1}$  values of thin and thick NFs in emission spectra with excited at 532 nm is smaller than that with excitation at 355 nm. In Figure 4-4, we definitely show that the emission spectra of NFs are quite sensitive to excitation energy. Compared with the 0-0 transition of free or amorphous chains at ~580 nm, the 0-0 transition of aggregated chains at ~630 nm is weaker with excitation at 355 nm but stronger with excitation at 532 nm. Furthermore, the 0-1 vibronic transition of aggregated chains at ~690 nm is eminent with excitation at 532 nm.

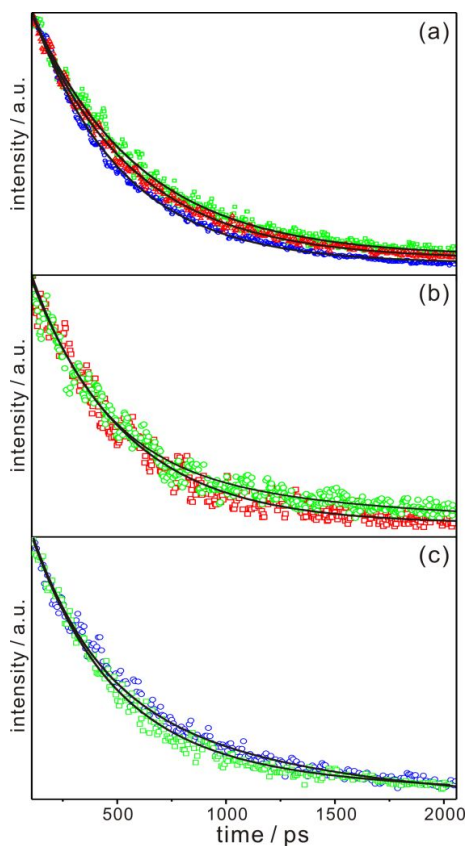


**Figure 4-5.** Emission kinetic profiles of thick NFs excited at 355 nm and monitored at 580 (blue), 650 (green), and 690 nm (red) (a), thin (green) and thick NFs (red) excited at 355 nm and monitored at 650 nm (b), and thick NFs excited at 355 (blue) and 532 nm (green) and monitored at 650 nm (c). NFs were dispersed in cyclohexanone, and solid lines are best-fitted curves to extract kinetic constants.

Figure 4-5a shows the emission kinetic profiles of thick NFs are quite dependent on the monitored wavelengths. We have assigned the decay times monitored at 580 nm of 433 ps for thick NFs and 440 ps for thin NFs to the decay of the relaxed  $S_1$  excitons of non-aggregated P3HT chains (Table 4-2).<sup>25,26,30</sup> Intrachain or interchain energy transfer ( $\sim 20$  and  $\sim 100$  ps)<sup>26</sup> has been hardly observed because its time scale is similar to our instrument response time (25 ps). Meanwhile, emission at 650 and 690 nm arises from the

recombination of the relaxed  $S_1$  excitons of aggregated P3HT chains. High intrachain or interchain aggregation within NFs can form a higher singlet exciton state (quasi-continuous band) via the singlet exciton-exciton annihilation (singlet fusion, Scheme 4-2)<sup>14</sup> due to the increase of interactions between adjacent  $S_1$  excitons in highly ordered regions. Thus, as shown in Table 4-2, the emission kinetic profile of thick NFs monitored at 650 nm has been deconvoluted into two decay components of 280 ps (55%) and 1100 ps (45%) while that monitored at 690 nm has two decay components of 250 ps (45%) and 900 ps (55%). Since the shorter decay is much faster than the recombination of normal relaxed  $S_1$  excitons, this process has been assigned to the biexciton recombination; the recombination of one  $S_1$  exciton increases the recombination probability of adjacent  $S_1$  excitons.<sup>39</sup> The longer decay component of ~1500 ps is due to the increased delocalization of relaxed  $S_1$  excitons induced by intrachain aggregation associated with the regioregularity and planarity of polymer chains.<sup>11,39</sup> Overall, the emission decay kinetic constants of NFs at 690 nm are found to be shorter than those at 650 nm because two-dimensional interchain effect inducing the nongeminate recombination of relaxed  $S_1$  excitons is more important at 690 nm than at 650 nm (Table 4-2).

**Table 4-2. Emission Decay Kinetic Constants of NFs Dispersed in Cyclohexanone**

sample	$\lambda_{\text{ex}}$ (nm)	$\lambda_{\text{mon}}$ (nm)	$I_0^a$	decay time (ps)	mean time (ps)
thin NFs	355	580	1.00	440	440
		650	0.16	320 (70%) + 1800 (30%)	584
		690	0.30	300 (57%) + 920 (43%)	567
	532	580	0.97	420	420
		650	0.07	380 (81%) + 2000 (19%)	633
		690	0.09	370 (80%) + 1100 (20%)	516
thick NFs	355	580	0.56	433	433
		650	0.13	280 (55%) + 1100 (45%)	649
		690	0.26	250 (45%) + 900 (55%)	607
	532	580	1.00	420	420
		650	0.04	340 (78%) + 1800 (22%)	661
		690	0.08	330 (75%) + 1100 (25%)	522
pristine NFs	355	580	1.00	400	400
		650	0.20	340 (75%) + 1000 (25%)	505
		690	0.27	330 (70%) + 900 (30%)	501

<sup>a</sup> Relative initial intensity.

As shown in Figure 3-5b and Table 4-2, the emission kinetic profile of thin NFs excited at 355 nm and monitored at 650 nm decays slower than that of thick NFs. High intrachain aggregation in J-type P3HT NFs has been reported to form delocalized  $S_1$  excitons, inducing nongeminate recombination. On the other hand, lower intrachain aggregation in H-type P3HT NFs forms localized  $S_1$  excitons, inducing faster geminate recombination dominantly.<sup>11</sup> However, since our thick NFs have both coupling types of H-aggregate and J-aggregate, the recombination of relaxed  $S_1$  excitons, faster than that in thin NFs, can be attributed to the probability

increase of the nongeminate recombination of relaxed  $S_1$  excitons due to interchain aggregation along the longitudinal axis. Since the probability of interactions between adjacent  $S_1$  excitons increases in thick NFs, the interchain mixing occurs more efficiently in thick NFs than in thin NFs. Therefore, the fraction of the fast decay component in thin NFs is greater than that in thick NFs. This result indicates that other charge-carriers such as polaron pairs and polarons are generated rapidly from higher singlet exciton states produced by the interchain mixing (singlet fusion) in competition with the vibrational relaxation of  $S_1$  excitons (Scheme 4-2).<sup>14</sup>

As discussed in Figure 4-4, since the excitation energy affects the excited state of NFs, we have also obtained the emission kinetic profiles of our NFs with excitation at 532 nm (Figure 4-5c). With decreasing excitation energy from 3.49 eV (355 nm) to 2.33 eV (532 nm), the fraction of the fast decay component increases in the emission kinetic profiles of both thin and thick NFs (Table 4-2). This result also suggests that the formation of a higher singlet exciton state associated with the fast decay component can be controlled by two critical factors: the excitation energy and the coupling type of NFs. As shown in Table 4-2, the emission decay kinetic profiles of pristine NFs excited at 355 nm and monitored at 650 and 690 nm have been also obtained. Compared to thin NFs, the decay time of the slow component monitored at 650 nm is shorter and the fraction of the fast component monitored at 690 nm is smaller. These results also indicate that non-aggregated or amorphous chains are predominant in pristine NFs. Although

we have concentrated our attention on the decay dynamics of relaxed  $S_1$  excitons, from now on, we will focus on the formation pathway and the decay dynamics of polaron pairs (PP), localized (LP), delocalized polarons (DP), and triplet ( $T_1$ ) excitons in NFs.

Femtosecond transient-absorption (TA) spectra of aggregate P3HT systems such as films and NFs have been diversely reported<sup>13-15,40b,41-44</sup> to understand the formation and decay of charge carriers such as excitons, PP, LP, and DP. Photoinduced absorption bands around 660, 740, 820, 1000, and 1200 nm have been assigned to PP, DP,  $T_1$  excitons, LP, and  $S_1$  excitons, respectively.<sup>14,40b,41</sup> Thus, as shown in Figure 4-6 and Figure S4-7, we have obtained picosecond TA kinetic profiles of NFs at various probe wavelengths from 660 nm to 1200 nm to gain a profound insight into the excited-state absorption species of NFs. Figure S4-7 observed in time windows of 50 ps shows that although initial TA signals at 0 ps have been observed definitely, any rise components have not been observed. This suggests that in competition with vibrational relaxation to  $S_1$  excitons ( $\sim 1$  ps) the fast formation of PP, DP, and LP takes place from higher singlet exciton states. Each TA kinetic profile of PP absorption at 660 nm in Figure 4-6a observed in time windows of 1000 ps has been deconvoluted into two decay components of 18 ps (74%) and 212 ps (26%) for thin NFs and 34 ps (78%) and 463 (22%) for thick NFs (Table 4-3). We have assigned the fast decay component (0.7 ps for thin NFs and 0.6 ps for thick NFs) to the downhill relaxation of self-trapped excitons (Table S4-2) and the medium decay

component (14 and 18 ps for thin NFs and 16 and 34 ps for thick NFs) to torsional relaxation or intra/interchain energy transfer (Table 4-3 and Table S4-2).<sup>28-30</sup> Especially, as shown in Figure 4-6a, the decay curve of PP of thin NFs is quite different from that of thick NFs. Since PP is an electron-hole pair bound by Coulomb interaction, this species often recombines geminately. As discussed with emission decay constants, interchain aggregation effect induces the delocalization of  $S_1$  excitons in association with nongeminate recombination. The decay time constant of PP in thin NFs (212 ps) has been found to be smaller than that in thick NFs (463 ps) because interchain aggregation is weaker than intrachain aggregation.

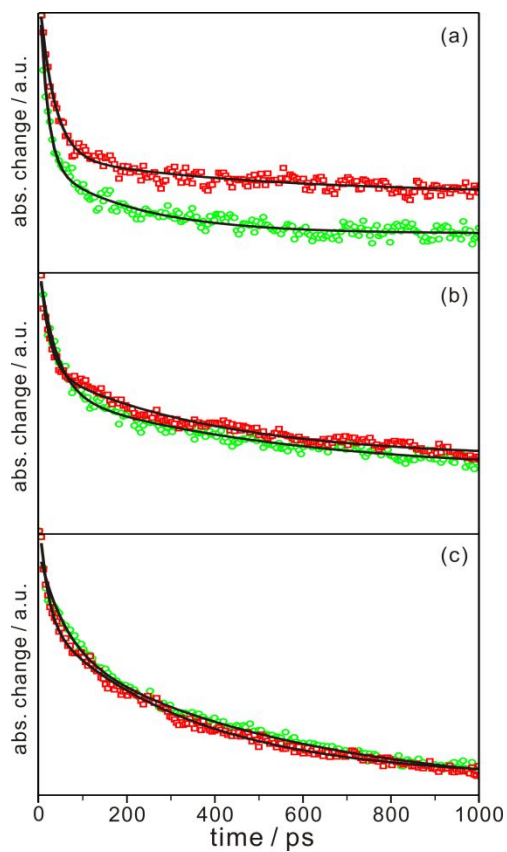


**Figure 4-6.** Picosecond transient-absorption kinetic profiles of thin NFs (green) and thick NFs (red) excited at 355 nm and probed at 660 (a), 740 (b), and 1000 nm (c). NFs were dispersed in cyclohexanone, and solid lines are best-fitted curves to extract kinetic constants.

**Table 4-3. Transient-Absorption Kinetic Constants of NFs Dispersed in Cyclohexanone with Excitation at 355 nm**

sample	window (ps)	$\lambda_{pr}$ (nm)	$A_0^a$ ( $10^{-3}$ )	decay time (ps)
thin NFs	1000	660	1.74	18 (74%) + 212 (26%)
		740	1.86	39 (63%) + 523 (37%)
		820	3.70	27 (48%) + 359 (52%)
		1000	7.40	58 (37%) + 535 (63%)
		1200	1.80	20 (40%) + 310 (60%)
	1000000	820	48.6	307,000
thick NFs	1000	660	1.66	34 (78%) + 463 (22%)
		740	2.00	21 (51%) + 383 (49%)
		820	3.45	22 (66%) + 616 (34%)
		1000	7.70	20 (33%) + 345 (67%)
		1200	2.82	20 (35%) + 290 (65%)
	1000000	820	51.5	322,000
pristine NFs	1000	660	1.20	17 (53%) + 291 (47%)
		740	1.68	36 (58%) + 526 (42%)
		820	3.12	49 (44%) + 2418 (56%)
		1000	8.10	32 (34%) + 395 (66%)
		1200	2.13	18 (33%) + 358 (67%)
	1000000	820	61.6	283,000

<sup>a</sup> Initial transient absorbance

The TA decay curves of DP and LP, namely free charge carriers, have been obtained for thin and thick NFs (Figure 4-6b,c). It has been reported<sup>41</sup> that DP bands originate from mobile polarons in ordered P3HT regions (lamellar structures with enhanced interchain coupling), whereas LP bands arise from localized polarons in disordered P3HT regions. Similarly, in our NFs, because the two-dimensional interchain effect induces the formation of DP, the initial transient absorbance of thick NFs in a time window of 50 ps is

larger than that of thin NFs (Table S4-2). The hot-exciton dissociation model is another important factor affecting the formation of LP and DP.<sup>14</sup> In other words, the formation of LP and DP is dependent on excitation energy. Since we have used one kind of excitation wavelength (355 nm), this phenomenon has not been observed in our TA kinetic profiles of NFs. However, in emission kinetic profiles of Figure 4-5c, as we have varied excitation wavelengths, this phenomenon has been observed (see the discussion of Figure 4-5c). Each TA kinetic profile of DP absorption at 740 nm in Figure 4-6b has been deconvoluted into two decay components of 39 ps (63%) and 523 ps (37%) for thin NFs and 21 ps (51%) and 383 ps (49%) for thick NFs. Unlike the decay dynamics of PP, the decay time constant of DP in thin NFs has been found to be smaller than that in thick NFs. The decay dynamics of LP is similar to that of DP; each TA kinetic profile of LP absorption at 1000 nm in Figure 4-6c has been deconvoluted into two decay components of 58 ps (37%) and 535 ps (63%) for thin NFs and 20 ps (33%) and 345 ps (67%) for thick NFs. Because P is a free-charge carrier, it recombines non-geminately. As thick NFs have both coupling types of H-aggregate and J-aggregate, the probability of the nongeminate recombination of free-charge carriers such as DP and LP increases due to the effect of interchain aggregation along the longitudinal axis, resulting in the faster recombination of DP and LP than in thin NFs. Meanwhile, Table 4-3 and Table S4-2 also show the fast (downhill relaxation of self-trapped excitons) and the medium (torsional relaxation or intra/interchain energy transfer) decay components of DP and LP in both thin

and thick NFs. As polaron is a free-charge carrier, the decay times of DP and LP in thick NFs are found to be shorter than the respective ones in thin NFs. On the other hand, because PP is an electron-hole pair bound by Coulomb interaction, the decay of PP in thick NFs is found to be slower than that in thin NFs.<sup>44</sup> As shown in Table 4-3 and Figure S4-7, we have also obtained the TA kinetic profiles of NFs at 1200 nm; each TA kinetic profile of  $S_1$  absorption at 1200 nm has been deconvoluted into two decay components of 20 ps (40%) and 310 ps (60%) for thin NFs and 20 ps (35%) and 290 ps (65%) for thick NFs. We have assigned the fast decay component of 20 ps to intra/interchain energy transfer.<sup>26</sup> Since the slow decay times are nearly consistent with the emission decay time constant of relaxed  $S_1$  excitons, the slow component has been considered to originate from the decay of relaxed  $S_1$  excitons, which is faster in thick NFs than in thin NFs due to interchain delocalization effect enhancing nongeminate recombination. As shown in Table 4-3, we have also obtained picosecond TA kinetic profiles of pristine NFs to understand the role of Au NPs in the charge-carrier dynamics of NFs. If the formation of  $S_1$  excitons in NFs is inhibited by Au NPs via energy or charge transfer, the initial transient absorbance of  $S_1$  excitons of thin NFs containing Au NPs would be significantly smaller than that of pristine NFs. However, the initial transient absorbance of  $S_1$  excitons at 1200 nm of thin NFs is slightly smaller than that of pristine NFs, whereas the initial transient absorbances of PP and DP at 660 and 740 nm, respectively, of thin NFs are

even larger than the respective ones of pristine NFs. These results suggest that Au NPs hardly hinder the formation of  $S_1$  excitons in NFs.

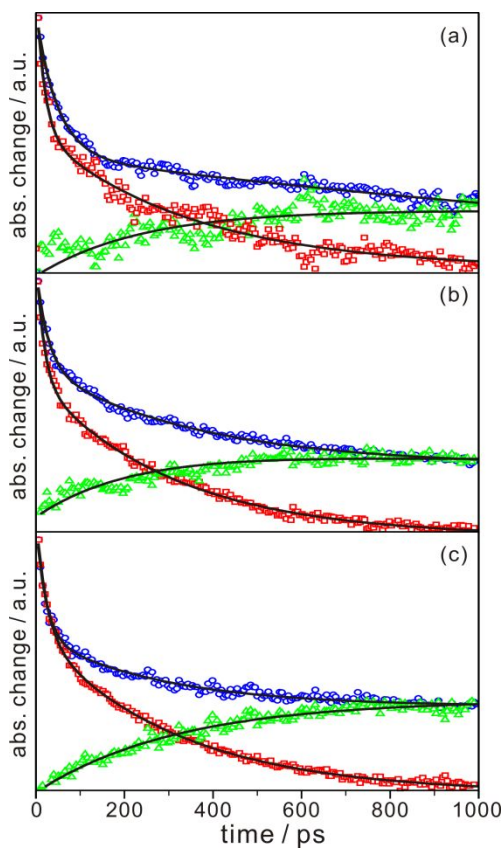


**Figure 4-7.** Picosecond transient-absorption kinetic profiles of pristine NFs (a), thin NFs (b), and thick NFs (c) excited at 355 nm and monitored at 820 (blue) and 1200 nm (red). Green triangles in each panel have been obtained by subtracting red squares from blue circles. Solid lines are best-fitted curves to extract time constants.

Unlike  $S_1$  excitons,  $T_1$  excitons have the advantage of a long lifetime ( $10^6 \sim 10^3$  s), expanding the diffusion length associated with optoelectronic-device performances. Because  $T_1$  excitons are usually generated in a small amount in conjugated polymers, formation mechanisms, such as singlet

fission,<sup>14</sup> intersystem crossing (ISC),<sup>25,28</sup> and nongeminate recombination of delocalized polaron species,<sup>11</sup> of T<sub>1</sub> excitons have been studied to overcome the low density of T<sub>1</sub> excitons. We have obtained TA kinetic profiles at 820 nm to gain the information of T<sub>1</sub> excitons; each TA kinetic profile in Figure 3-7 and Figure S3-7 has been deconvoluted into two decay components (Table 4-3 and Table S4-2). As shown in Figure 3-7, we have obtained the rise curves (green triangles) associated with formation dynamics of T<sub>1</sub> excitons by subtracting the TA decay profiles of S<sub>1</sub> absorption at 1200 nm from the TA decay profiles of S<sub>1</sub> and T<sub>1</sub> absorption at 820 nm.<sup>14</sup> The formation time constants of 200 ps for pristine NFs, 250 ps for thin NFs, and 380 ps for thick NFs have been obtained via fitting exponential functions of  $-A_r \exp(-t/\tau_r) + A_d \exp(-t/\tau_d) + B$  to the rise curves of Figure 4-7. The obtained rise times are considerably shorter than a reported ISC time (1.2 ns).<sup>28</sup> As interchain mixing related to the formation of PP and DP occurs less efficiently in pristine NFs than in both thin and thick NFs, T<sub>1</sub> formation via singlet fission from a higher singlet exciton state occurs faster and more efficiently in pristine NFs than in both thin and thick NFs (Scheme 4-2). The threshold energy requirement for the singlet fission has been reported as two thermalized T<sub>1</sub> excitons (2ET<sub>1</sub>).<sup>14</sup> The energy level of the lowest T<sub>1</sub> exciton state (ET<sub>1</sub>) has been estimated to be 1.43 eV for pristine NFs and 1.40 eV for both thin and thick NFs from the energy level of the lowest S<sub>1</sub> exciton state (ES<sub>1</sub>) and the energy gap between ES<sub>1</sub> and ET<sub>1</sub> ( $\Delta E_{ST}$ ),<sup>14</sup> as the energy level of the lowest S<sub>1</sub> exciton state has been calculated from absorption spectra as

1.88 eV for pristine NFs and 1.84 eV for both thin and thick NFs and the singlet-triplet splitting energy  $\Delta E_{ST}$  has been reported to be 0.45 eV for highly ordered poly(3-octylthiophene) films. Therefore, the threshold energy for the singlet fission has been estimated as 2.86 eV for pristine NFs and 2.80 eV for both thin and thick NFs. Because we used 355 nm (3.49 eV) as the excitation wavelength, the singlet fission could be observed in our TA kinetic profiles of NFs. In the next discussion, we will clearly suggest that  $T_1$  excitons in NFs are mainly produced through the singlet fission rather than through ISC.

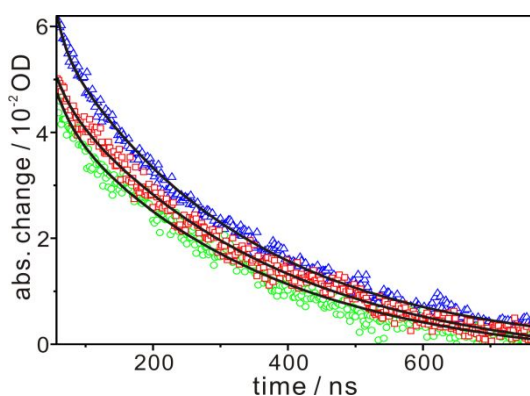


**Figure 4-8.** Nanosecond transient-absorption kinetic profiles of pristine NFs (blue), thin NFs (green), and thick NFs (red). Samples were excited at 355 nm and probed at 820 nm. Solid lines are best-fitted curves to extract time constants.

We have also obtained nanosecond time-resolved TA kinetic profiles of NFs to support the formation path way of  $T_1$  excitons in NFs (Figure 4-8). Each TA kinetic profile of  $T_1$  absorption at 820 nm has been deconvoluted into a single decay component (Table 4-3). The  $T_1$  absorption kinetic profiles of non-aggregated P3HT and Au@P3HT NPs in chloroform have been reported<sup>30</sup> to have a lifetime of  $\sim 235$  ns, which is considerably smaller than

the  $T_1$  decay times of our NFs. In both thin and thick NFs, because the threshold energy for the singlet fission is 2.80 eV,  $T_1$  excitons were hardly observed with excitation at 532 nm (2.33 eV) on a nanosecond time scale. In addition, the initial TA signals at 820 nm of thin and thick NFs are not larger than that of pristine NFs, suggesting that most  $T_1$  excitons in NFs are not generated through ISC. Therefore, we conclude that  $T_1$  excitons in our prepared NFs are mainly generated through the singlet fission from a higher singlet exciton state produced by the singlet fusion.

#### **4. 5. Conclusions**

The formation and decay dynamics of  $S_1$  and  $T_1$ , PP, and LP and DP dependent on the aggregate types of NFs has been comprehensively investigated by time-resolved emission and TA spectroscopy. The thickness of NFs associated with a transition in dominant exciton coupling from intrachain to interchain coupling has been facilely tuned via controlling the concentration of Au@P3HT NPs in cyclohexanone. The emission ratio of the 0-0 transition to the 0-1 vibronic transition of thin NFs (4.2) having thickness of 15 nm is 2.5 times greater than that of thick NFs (1.7) having thickness of 25 nm, indicating that the J-aggregate character is predominant in thin NFs, whereas the H-aggregate character becomes as important as the J-aggregate character in thick NFs. With increasing excitation energy, the fraction of the fast emission decay component has been found to decrease, suggesting that

the fast formation of localized PP, LP, and DP results from higher singlet exciton states produced by the singlet fusion. Since thick NFs have both coupling types of H-aggregates and J-aggregates, the faster recombination of relaxed  $S_1$  excitons in thick NFs than in thin NFs can be attributed to the increased nongeminate recombination of relaxed  $S_1$  excitons due to interchain aggregation. The faster decay dynamics of DP and LP in thick NFs than in thin NFs is due to the larger interchain stacking effect inducing the delocalization of DP and LP. As interchain aggregation is weaker than intrachain aggregation, PP decays faster in thin NFs than in thick NFs. The initial TA signal of  $S_1$  excitons of thin NFs is slightly smaller than that of pristine NFs whereas the initial TA signals of PP and DP of thin NFs are even larger than the respective ones of pristine NFs, suggesting that Au NPs hardly hinder formation of  $S_1$  excitons. The formation time of  $T_1$  excitons was considerably shorter than a reported ISC time, and  $T_1$  excitons were hardly observed with excitation at 532 nm on a nanosecond time scale. However,  $T_1$  excitons have been observed with excitation at 355 nm. The initial TA signal of pristine NFs on a nanosecond time scale is larger than those of thin and thick NFs. Thus,  $T_1$  excitons within our prepared NFs are mainly generated through the singlet fission from a higher singlet exciton state rather than through ISC from the lowest  $S_1$  exciton state.

## 4. 6. References

- (1) (a) Noguez, C. *J. Phys. Chem. C* **2007**, *111*, 3806–3819. (b) Ray, P. C. *Chem. Rev.* **2010**, *110*, 5332–5365.
- (2) Kim, J.-Y.; Lee, D.; Kim, H. J.; Lim, I.; Lee, W. I.; Jang, D.-J. *J. Mater. Chem. A* **2013**, *1*, 5982–5988.
- (3) Kim, H.-B.; Jang, D.-J. *CrystEngComm* **2012**, *14*, 6946–6951.
- (4) Kim, S. J.; Ah, C. S.; Jang, D.-J. *Adv. Mater.* **2007**, *19*, 1064–1068.
- (5) Huynh, W. U.; Dittmer, J. J.; Alivisatos, A. P. *Science* **2002**, *295*, 2425–2427.
- (6) Park, D. H.; Kim, M. S.; Joo, J. *Chem. Soc. Rev.* **2010**, *39*, 2439–2452.
- (7) Reiss, P.; Couderc, E.; De Girolamo, J.; Pron, A. *Nanoscale* **2011**, *3*, 446–489.
- (8) Stratakis, E.; Kymakis, E. *Mater. Today* **2013**, *16*, 133–146.
- (9) Siringhaus, H.; Brown, P.; Friend, R.; Nielsen, M. M.; Bechgaard, K.; Langeveld-Voss, B.; Spiering, A.; Janssen, R. A.; Meijer, E.; Herwig, P. *Nature* **1999**, *401*, 685–688.
- (10) Park, S.-J.; Kang, S.-G.; Fryd, M.; Saven, J. G.; Park, S.-J. *J. Am. Chem. Soc.* **2010**, *132*, 9931–9933.
- (11) Thomas, A. K.; Garcia, J. A.; Ulibarri-Sanchez, J.; Gao, J.; Grey, J. K. *ACS Nano* **2014**, *8*, 10559–10568.
- (12) Barnes, M. D.; Baghar, M. *J. Polym. Sci. Pol. Phys.* **2012**, *50*, 1121–1129.

- (13) Guo, J.; Ohkita, H.; Benten, H.; Ito, S. *J. Am. Chem. Soc.* **2010**, *132*, 6154–6164.
- (14) Guo, J.; Ohkita, H.; Benten, H.; Ito, S. *J. Am. Chem. Soc.* **2009**, *131*, 16869–16880.
- (15) Ohkita, H.; Cook, S.; Astuti, Y.; Duffy, W.; Tierney, S.; Zhang, W.; Heeney, M.; McCulloch, I.; Nelson, J.; Bradley, D. D. C.; et al. *J. Am. Chem. Soc.* **2008**, *130*, 3030–3042.
- (16) Nagarjuna, G.; Baghgar, M.; Labastide, J. A.; Algaier, D. D.; Barnes, M. D.; Venkataraman, D. *ACS Nano* **2012**, *6*, 10750-10758.
- (17) Huettner, S.; Sommer, M.; Hodgkiss, J.; Kohn, P.; Thurn-Albrecht, T.; Friend, R. H.; Steiner, U.; Thelakkat, M. *ACS Nano* **2011**, *5*, 3506-3515.
- (18) He, M.; Zhao, L.; Wang, J.; Han, W.; Yang, Y.; Qiu, F.; Lin, Z. *ACS Nano* **2010**, *4*, 3241-3247.
- (19) Gilroy, J. B.; Lunn, D. J.; Patra, S. K.; Whittell, G. R.; Winnik, M. A.; Manners, I. *Macromolecules* **2012**, *45*, 5806-5815.
- (20) Berson, S.; De Bettignies, R.; Bailly, S.; Guillerez, S. *Adv. Func. Mater.* **2007**, *17*, 1377-1384.
- (21) Kamkar, D. A.; Wang, M.; Wudl, F.; Nguyen, T.-Q. *ACS Nano* **2012**, *6*, 1149-1157.
- (22) Xu, J.; Hu, J.; Liu, X.; Qiu, X.; Wei, Z. *Macromol. Rapid Commun.* **2009**, *30*, 1419-1423.
- (23) Kim, F. S.; Jenekhe, S. A. *Macromolecules* **2012**, *45*, 7514-7519.

- (24)(a) Choi, S. Y.; Lee, J. U.; Lee, J. W.; Lee, S.; Song, Y. J.; Jo, W. H.; Kim, S. H. *Macromolecules* **2011**, *44*, 1771-1774. (b) Kim, J. S.; Lee, J. H.; Park, J. H.; Shim, C.; Sim, M.; Cho, K. *Adv. Funct. Mater.* **2011**, *21*, 480-486. (c) Shimomura, T.; Takahashi, T.; Ichimura, Y.; Nakagawa, S.; Noguchi, K.; Heike, S.; Hashizume, T. *Phys. Rev. B* **2011**, *83*, 115314.
- (25) Cook, S.; Furube, A.; Katoh, R. *Energ. Environ. Sci.* **2008**, *1*, 294–299.
- (26) Ferreira, B.; da Silva, P. F.; Seixas de Melo, J. S.; Pina, J.; Maçanita, A. *J. Phys. Chem. B* **2012**, *116*, 2347–2355.
- (27)(a) Grancini, G.; Polli, D.; Fazzi, D.; Cabanillas-Gonzalez, J.; Cerullo, G.; Lanzani, G. *J. Phys. Chem. Lett.* **2011**, *2*, 1099–1105. (b) Grancini, G.; Biasiucci, M.; Mastroia, R.; Scotognella, F.; Tassone, F.; Polli, D.; Gigli, G.; Lanzani, G. *J. Phys. Chem. Lett.* **2012**, *3*, 517–523.
- (28)(a) Banerji, N.; Cowan, S.; Vauthey, E.; Heeger, A. J. *J. Phys. Chem. C* **2011**, *115*, 9726–9739. (b) Banerji, N.; Seifert, J.; Wang, M.; Vauthey, E.; Wudl, F.; Heeger, A. J. *Phys. Rev. B* **2011**, *84*, 075206.
- (29) Xie, Y.; Li, Y.; Xiao, L.; Qiao, Q.; Dhakal, R.; Zhang, Z.; Gong, Q.; Galipeau, D.; Yan, X. *J. Phys. Chem. C* **2010**, *114*, 14590–14600.
- (30) Lee, D.; Jang, D. *J. Polymer* **2014**, *55*, 5469-5476.
- (31) Xu, T.; Yan, M.; Hoefelmeyer, J. D.; Qiao, Q. *RSC Adv.* **2012**, *2*, 854-862.
- (32)(a) Labastide, J. A.; Baghgar, M.; Dujovne, I.; Venkatraman, B. H.; Ramsdell, D. C.; Venkataraman, D.; Barnes, M. D. *J. Phys. Chem. Lett.*

- 2011**, 2, 2089-2093. (b) Magnanelli, T. J.; Bragg, A. E. *J. Phys. Chem. Lett.* **2015**, 6, 438-445.
- (33)(a) Spano, F. C.; Silva, C. *Annu. Rev. Phys. Chem.* **2014**, 65, 477-500.  
(b) Yamagata, H.; Spano, F. *J. Chem. Phys.* **2012**, 136, 184901. (c)  
Spano, F. C. *Acc. Chem. Res.* **2009**, 43, 429-439.
- (34) Baghgar, M.; Labastide, J. A.; Bokel, F.; Hayward, R. C.; Barnes, M. D. *J. Phys. Chem. C* **2014**, 118, 2229-2235.
- (35)(a) Niles, E. T.; Roehling, J. D.; Yamagata, H.; Wise, A. J.; Spano, F. C.; Moule, A. J.; Grey, J. K. *J. Phys. Chem. Lett.* **2012**, 3, 259-263. (b)  
Panzer, F.; Sommer, M.; Bäessler, H.; Thelakkat, M.; Köhler, A. *Macromolecules* **2015**, 48, 1543-1553.
- (36) Baghgar, M.; Barnes, A. M.; Pentzer, E.; Wise, A. J.; Hammer, B. A.; Emrick, T.; Dinsmore, A. D.; Barnes, M. D. *ACS Nano* **2014**, 8, 8344-8349.
- (37) Baghgar, M.; Labastide, J.; Bokel, F.; Dujovne, I.; McKenna, A.; Barnes, A. M.; Pentzer, E.; Emrick, T.; Hayward, R.; Barnes, M. D. *J. Phys. Chem. Lett.* **2012**, 3, 1674-1679.
- (38) Carach, C.; Gordon, M. J. *J. Phys. Chem. B* **2013**, 117, 1950-1957.
- (39) Labastide, J. A.; Baghgar, M.; McKenna, A.; Barnes, M. D. *J. Phys. Chem. C* **2012**, 116, 23803-23811.
- (40)(a) Gao, J.; Kamps, A.; Park, S.-J.; Grey, J. K. *Langmuir* **2012**, 28, 16401-16407. (b) Martin, T. P.; Wise, A. J.; Busby, E.; Gao, J.; Roehling, J. D.; Ford, M. J.; Larsen, D. S.; Moulé, A. J.; Grey, J. K. *J.*

- Phys. Chem. B* **2012**, *117*, 4478-4487. (c) Hu, Z.; Adachi, T.; Haws, R.; Shuang, B.; Ono, R. J.; Bielawski, C. W.; Landes, C. F.; Rossky, P. J.; Vanden Bout, D. A. *J. Am. Chem. Soc.* **2014**, *136*, 16023-16031.
- (41) Hwang, I.-W.; Moses, D.; Heeger, A. J. *J. Phys. Chem. C* **2008**, *112*, 4350-4354.
- (42) Kandada, A. R. S.; Grancini, G.; Petrozza, A.; Perissinotto, S.; Fazzi, D.; Raavi, S. S. K.; Lanzani, G. *Sci. Rep.* **2013**, *3*, 2073.
- (43) Tamai, Y.; Matsuura, Y.; Ohkita, H.; Benten, H.; Ito, S. *J. Phys. Chem. Lett.* **2014**, *5*, 399-403.
- (44) Ogata, Y.; Kawaguchi, D.; Tanaka, K. *Sci. Rep.* **2015**, *5*, 8436.

#### 4. 7. Supporting Information

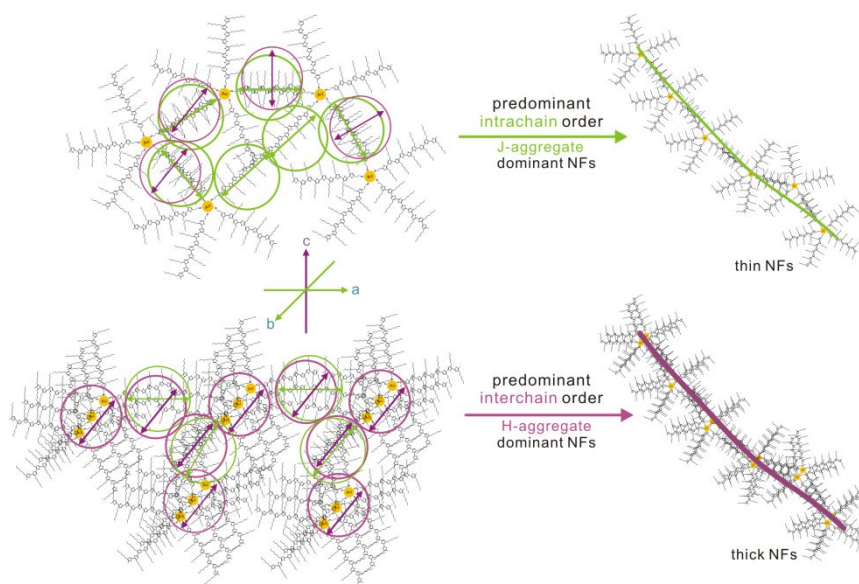


**Figure S4-1.** Proposed formation mechanisms of thin and thick NFs.

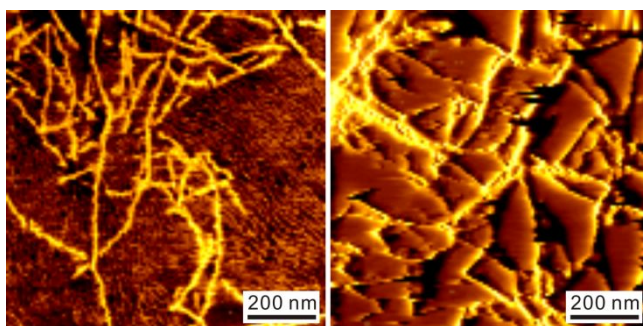


**Figure S4-2.** AFM images of thin (left) and thick NFs (right).

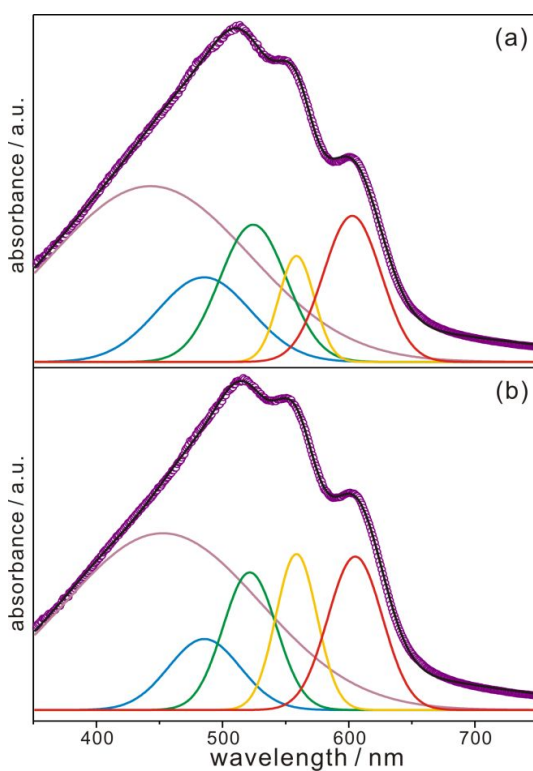


**Figure S4-3.** Absorption spectra (circles) of thin (a) and thick NFs (b). While Gaussian-fitted curves 1 (violet) and 2 (blue) are attributed to the  $S_0$ - $S_1$  transition of free chains, curves 3 (green), 4 (yellow), and 5 (red) are attributed to the 0-2, the 0-1, and the 0-0 transitions of aggregated chains, respectively. Black curves represent the sum of the five fitted curves. The exact locations and the absorbance percentages of the five fitted curves are outlined in Table S4-1.

**Table S4-1. Spectral Positions of Five Gaussian Curves Fitted to Each Absorption Spectrum of NFs Dispersed in Cyclohexanone**

sample	curve 1 (nm)	curve 2 (nm)	curve 3 (nm)	curve 4 (nm)	curve 5 (nm)
thin NFs	443±93 (54%) <sup>a</sup>	485±44 (12%)	524±31 (14%)	559±17 (6%)	603±27 (14%)
thick NFs	453±91 (56%)	486±33 (8%)	522±25 (12%)	559±19 (11%)	605±25 (13%)
pristine NFs	422±58 (27%)	479±36 (26%)	515±26 (19%)	555±22 (16%)	603±23 (12%)

<sup>a</sup>Absorbance percentage of each curve.

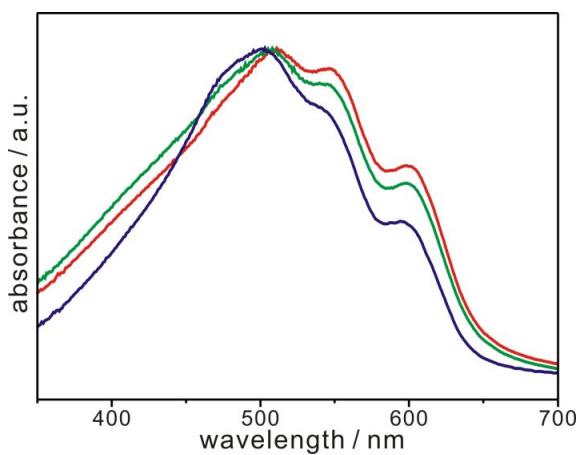


**Figure S4-4.** Absorption spectra of pristine NFs (blue), thin NFs (green), and thick NFs (red).

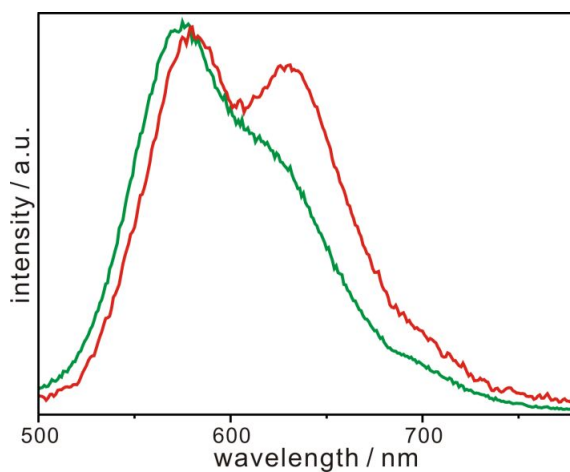


**Figure S4-5.** Emission spectra of pristine NFs (green) and thin NFs (red) in cyclohexanone with excitation at 430 nm.

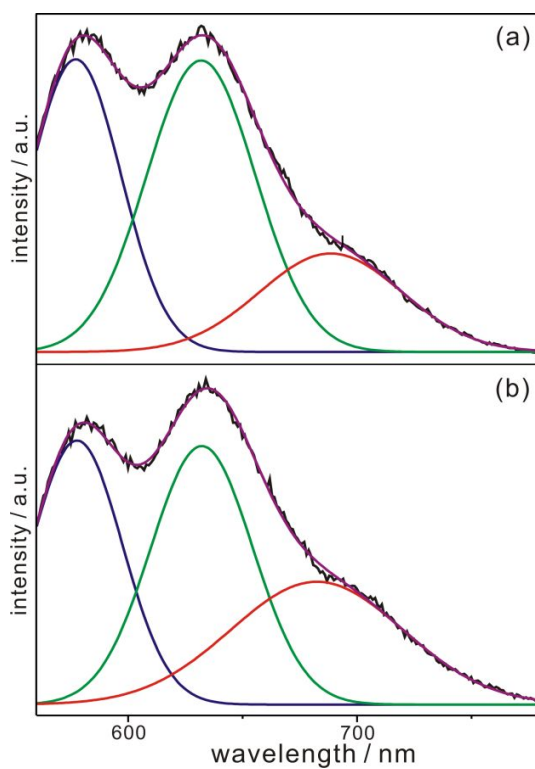


**Figure S4-6.** Emission spectra (circles) of thin (a) and thick NFs (b) in cyclohexanone with excitation at 532 nm, fitted with three Gaussian curves  $\lambda_1$  (blue),  $\lambda_2$  (green), and  $\lambda_3$  (red); black curves represent the sum of the three fitted curves.

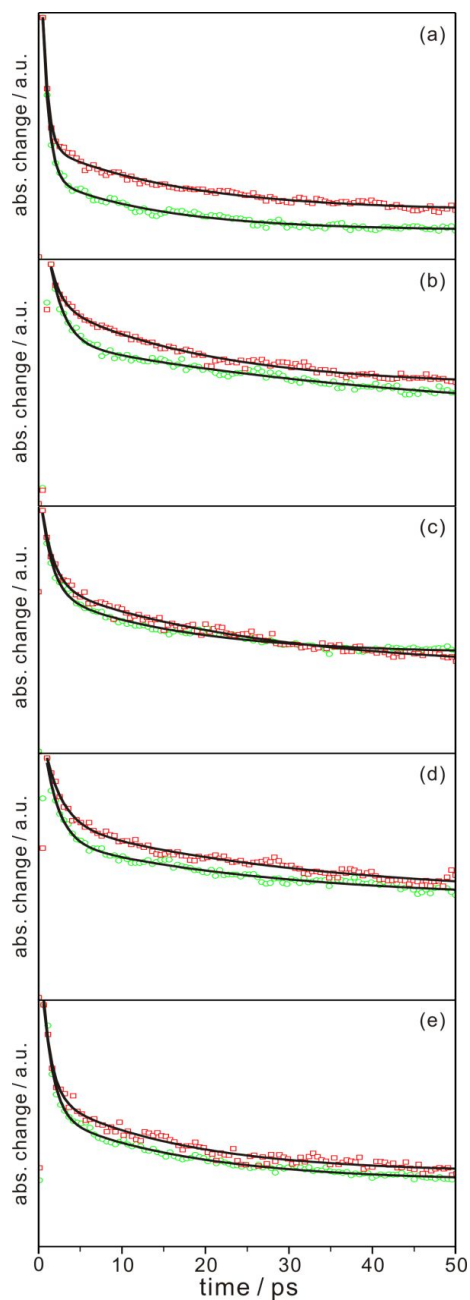


**Figure S4-7.** Picosecond transient-absorption kinetic profiles of thin NFs (green) and thick NFs (red) excited at 355 nm and probed at 660 (a), 740 (b), 820 (c), 1000 (d), and 1200 nm (e) observed in time windows of 50 ps. NFs were dispersed in cyclohexanone, and solid lines are best-fitted curves to extract kinetic constants.

**Table S4-2. Transient-Absorption Kinetic Constants of NFs Dispersed in Cyclohexanone with Excitation at 355 nm, Observed in Time Windows of 50 ps**

sample	$\lambda_{pr}$ (nm)	$A_0^a$ ( $10^{-3}$ )	decay time (ps)
thin NFs	660	5.38	0.7 (76%) + 14 (24%)
	740	2.42	1.7 (46%) + 44 (54%)
	820	3.42	1.3 (58%) + 16 (42%)
	1000	11.1	1.7 (57%) + 26 (43%)
	1200	3.71	1.2 (68%) + 17 (32%)
thick NFs	660	4.61	0.6 (69%) + 16 (31%)
	740	2.69	1.2 (25%) + 18 (75%)
	820	3.13	1.4 (47%) + 25 (53%)
	1000	9.95	2.0 (43%) + 29 (57%)
	1200	3.99	1.1 (60%) + 16 (40%)
pristine NFs	660	2.80	1.0 (71%) + 24 (29%)
	740	1.99	1.6 (31%) + 63 (69%)
	820	3.60	1.5 (40%) + 90 (60%)
	1000	10.4	1.3 (34%) + 18 (66%)
	1200	4.09	1.7 (38%) + 38 (62%)

<sup>a</sup> Initial transient absorbance

## **Chapter 5. Excited-State Dynamics of an Amphiphilic Diblock Copolymer Self-Assembled from Mixed Solvents**

## 5. 1. Abstract

An amphiphilic diblock-copolymer consisting of poly(3-hexylthiophene) and poly(4-vinylpyridine) has been synthesized and self-assembled from mixed selective solvents of tetrahydrofuran and methanol to produce nanostructures having photoluminescence spanning from the blue to the red. The emission decay times of the nanostructures have been found to increase with the fraction of methanol, suggesting that the probability of the nongeminate recombination of relaxed  $S_1$  excitons decreases with the increase of medium polarity. The emission decay times are shorter at 690 nm than at 650 nm, indicating that two-dimensional interchain effect is more important for the 0-1 vibronic transition than for the 0-0 transition. The initial intensity percentage of the fast component of biphasic emission decay is much larger with excitation at 532 than with excitation at 355 nm, suggesting that other charge carriers such as polarons are generated rapidly from  $S_1$  excitons in competition with vibrational relaxation.

## 5. 2. Introduction

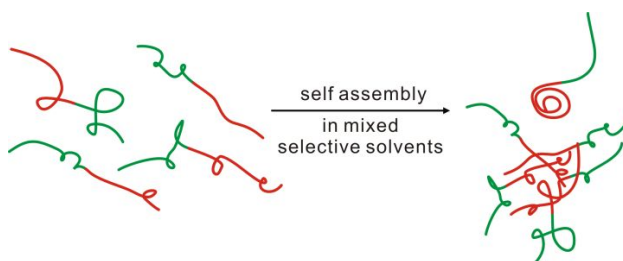
The fabrication and characterization of nanostructured materials having functional properties have been widely explored due to their potential applications in the field of nanotechnology.<sup>1-4</sup> Among numerous nanostructured materials, conjugated polymers have been extensively studied for applications in optoelectronic devices such as light-emitting diodes, biosensors, and photovoltaic cells because of their advantages such as lightweight, flexibility, processability, roll-to-roll production, low cost, and large area.<sup>5-8</sup> In spite of these diverse advantages, organic solar cells containing active layers based on conjugated polymers have not been commercialized well due to their low power-conversion efficiency.<sup>9</sup> Thus, many research groups have diversely reported solutions such as the synthesis of low-band-gap conjugated polymers,<sup>10</sup> the functionality enhancement of conjugated polymers,<sup>11</sup> the development of new device-fabrication processes,<sup>12</sup> and the fabrication of hybrid nanocomposites composed of inorganic nanoparticles and organic conjugated polymers<sup>13,14</sup> in order to overcome this low-efficiency problem. In particular, amphiphilic diblock copolymers consisting of a rod-shape polymer such as poly(3-hexylthiophene) (P3HT), which is most commonly used in optoelectronic devices, have received intense attention for applications in photovoltaic cells because of their excellent optical and transport properties highly dependent on their nanoscale morphology, which is also tunable facilely with selective solvents.<sup>15,16</sup> Since a rod-shape polymer and a coil-shape polymer are covalently linked in an amphiphilic diblock copolymer, compared to conjugated

homo polymers and polymer blends, amphiphilic diblock copolymers can be spontaneously separated into two different transport channels of a well-ordered or amorphous structure on the nano-sized scale, facilitating the migration of charge carriers to improve optoelectronic device performances.<sup>17</sup> Quasi-living polymerization methods such as atom transfer radical polymerization (ATRP),<sup>18</sup> ring-opening metathesis polymerization (ROMP),<sup>19</sup> and reversible addition-fragmentation chain transfer polymerization (RAFT)<sup>20</sup> have been reported numerously as synthetic strategies of amphiphilic diblock copolymers consisting of P3HT.

The aggregates of conjugated polymers can be distinguished by two types of fundamental electronic interactions: intrachain head-to-tail (HT) through-bond interactions lead to J-aggregate behaviors and interchain Coulombic head-to-head (HH) interactions lead to H-aggregate behaviors.<sup>21</sup> When interchain HH order is dominant in H-aggregate nanofibers (NFs), the 0-0 electronic transition is forbidden by symmetry ( $\Sigma\mu = 0$ ) and less intense than the 0-1 vibronic sideband, giving rise to 0-0/0-1 intensity ratios smaller than 1. In contrast, when intrachain HT order is dominant in J-aggregate NFs, the 0-0 transition is allowed ( $\Sigma\mu \neq 0$ ) and more intense than the 0-1 vibronic sideband, thus giving rise to 0-0/0-1 intensity ratios larger than 1.<sup>21-25</sup>

Diverse recent spectroscopic studies on various assembled types of pristine P3HT and amphiphilic diblock copolymers consisting of P3HT have shown that the formation and decay of charge carriers such as excitons and polarons are strongly dependent on the conformation and packing behaviors of P3HT chains.<sup>22-24,26-35</sup>

However, many aspects of the photophysical properties of amphiphilic diblock copolymers self-assembled in mixed selective solvents remain still unclear. In this paper, we present that an amphiphilic diblock copolymer (P3HT-*b*-P4VP) consisting of a rod-shape poly(3-hexylthiophene) block and a coil-shape poly(4-vinylpyridine) block has been synthesized by the RAFT polymerization of 4-vinylpyridine using a trithiocarbonate-terminated P3HT as a macro-RAFT agent (Scheme S5-1).<sup>20</sup> The mixed-solvent method<sup>36</sup> has been used to fabricate self-assembled nanostructures in a dilute solution by adding methanol (MeOH) as a poor solvent to tetrahydrofuran (THF) (Scheme 5-1). The emission colors of self-assembled P3HT-*b*-P4VP nanostructures have been facilely tuned from the blue to the red by altering the fraction of MeOH in mixed solvents of MeOH and THF. It has been found that the emission of P3HT-*b*-P4VP around 480 nm is enormously stronger and decays much more slowly in a 5:1 (v/v) mixture solution of MeOH and THF than in a 1:5 (v/v) mixture solution of MeOH and THF, indicating that the conjugation length of P3HT is extensively reduced in a polar solvent. Meanwhile, emission around 650 nm originates from the 0-0 transition of aggregated chains associated with J-type (intrachain) aggregation while emission around 690 nm is due to the 0-1 vibronic transition of aggregated chains associated with H-type (interchain) aggregation. The emission decay times of self-assembled P3HT-*b*-P4VP have been found to be shorter at 690 nm than at 650 nm, indicating that two-dimensional interchain effect inducing the nongeminate recombination of relaxed S<sub>1</sub> excitons is stronger in H-type aggregates than in J-type aggregates.



**Scheme 5-1. Schematic for the fabrication of P3HT-*b*-P4VP nanostructures self-assembled from mixed selective solvents, where the red and the green indicate P3HT and P4VP, respectively.**

### 5. 3. Experimental Section

**5. 3. 1. Synthesis.** The detailed synthetic and characterization procedures of hydroxypropyl-terminated poly(3-hexylthiophene) (P3HT-OH) ( $M_n = 10,400 \text{ g mol}^{-1}$ , PDI = 1.13, MALDI-MS  $m/z = 6,960$ ) have already been reported,<sup>33</sup> and 3-benzylsulfanylthiocarbonylsulfanylpropionic acid chloride (RAFT agent) was synthesized as previously described.<sup>20</sup> Amphiphilic diblock copolymer P3HT-*b*-P4VP consisting of P3HT and poly(4-vinylpyridine) (P4VP) was synthesized *via* the RAFT polymerization of 4-vinyl pyridine using a trithiocarbonate-terminated P3HT as a macro-RAFT agent (Scheme S5-1), as described in a previous report.<sup>20</sup> For the fabrication of self-assembled nanostructures in mixed solvents, 1.0 mg of P3HT-*b*-P4VP was completely dissolved in 3.0 mL of THF of a nonselective solvent at room temperature. Then, MeOH as a quantitative selective polar solvent of the P4VP block was added into the limp orange-colored P3HT-*b*-P4VP solution to reach a certain volume ratio of MeOH to THF ( $R$ ). The mixture solution was turned into a homogeneous transparent violet-colored solution and incubated in

an argon glove box at room temperature for a day to generate self-assembled P3HT-*b*-P4VP nanostructures.

**5. 3. 2. Characterization.**  $^1\text{H}$  (500 MHz) and  $^{13}\text{C}$  (125 MHz) spectra were acquired in  $\text{CDCl}_3$  using a Varian/Oxford As-500 spectrometer. Size-exclusion chromatography (SEC) was performed using a Waters system consisting of a 1515 pump and a 2414 refractive-index detector and a Shodex GPC LF-804 column. Matrix-assisted laser desorption ionization time-of-flight (MALDI-TOF) mass spectra were recorded using an Applied Biosystems Voyager-DE STR biospectrometry workstation. Transmission electron microscopy (TEM) images were obtained using a Hitachi H7600 microscope; a TEM sample was prepared by evaporating and drying a colloidal droplet on a carbon-coated copper grid in an argon glove box at room temperature. Absorption spectra were measured with a Scinco S3100 UV/vis spectrophotometer, and emission spectra were obtained using a home-built fluorometer consisting of a 75 W Acton Research XS 432 Xe lamp with an Acton Research Spectrapro150 monochromator of 0.15 m and an Acton Research PD438 photomultiplier tube attached to an Acton Research Spectrapro300 monochromator of 0.30 m. Picosecond emission kinetic profiles with excitation of 355 or 532 nm pulses from a mode-locked Quantel YG901-10 Nd:YAG laser of 25 ps were detected using a Hamamatsu C2830 streak camera of 10 ps attached to a Princeton Instruments RTE128H CCD detector. Emission wavelengths were selected using combined band-pass and cut-off filters. Emission kinetic constants were extracted by fitting measured kinetic profiles to computer-simulated kinetic curves convoluted with instrument temporal response functions.

## 5. 4. Results and Discussion

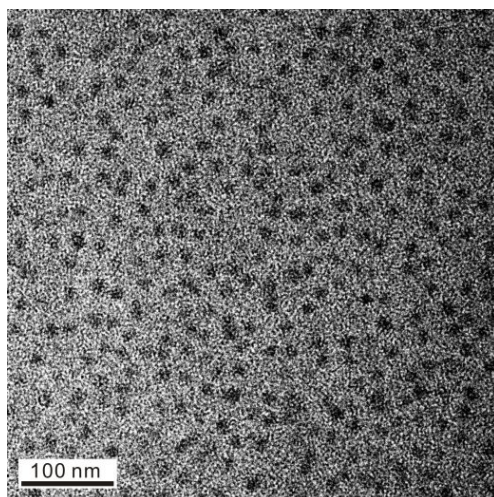


**Figure 5-1.** TEM image of P3HT-*b*-P4VP nanostructures self-assembled in a mixed solvent of  $R = 1.0$ .

The molar and weight fractions of the P4VP block in P3HT-*b*-P4VP were estimated by measuring  $^1\text{H}$  NMR spectra (Figure S5-1).<sup>15b</sup> The measured integration value of the two aromatic protons of the P4VP signal in the range of 6.70–6.10 ppm (4.82) relatively to the integration value of the aromatic proton of the P3HT signal at 6.98 ppm has indicated that the mole fraction of the P4VP block in P3HT-*b*-P4VP is 0.69. Since the molar weights of the repeating units of P3HT and P4VP are 166 g/mol and 105 g/mol, respectively, the weight fraction of the P4VP block in P3HT-*b*-P4VP has been estimated as 0.60. Figure 5-1 shows that P3HT-*b*-P4VP chains in a 1 : 1 (v/v) mixed solvent of MeOH and THF are self-assembled into nanoparticles having an average diameter of  $14.5 \pm 1.5$ . It is suggested that the nanoparticles have P3HT@P4VP core-shell nanostructures because, in mixed

solvents of MeOH and THF, the hydrophilic P4VP block is likely to be exposed at the exterior positions and the hydrophobic P3HT block is likely to be aggregated at the interior positions. The photophysical properties of self-assembled P3HT-*b*-P4VP nanostructures dependent on aggregated types of P3HT blocks will be discussed with static and time-resolved optical spectra of self-assembled P3HT-*b*-P4VP in mixed solvents of MeOH and THF.

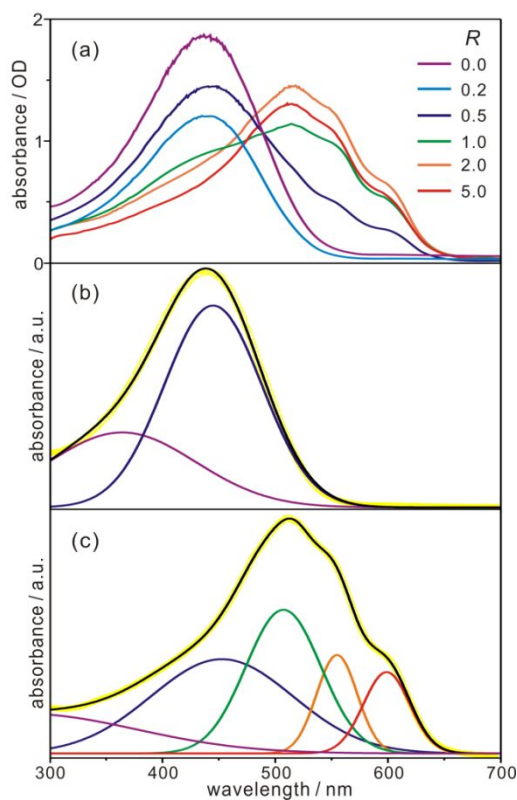


**Figure 5-2.** Absorption spectra of P3HT-*b*-P4VP self-assembled in mixed solvents of indicated *R* values (a). Absorption spectra (yellow circles) of P3HT-*b*-P4VP in mixed solvents of *R* = 0.2 (b) and 5.0 (c); Gaussian curves of  $\lambda_{a1}$  (violet),  $\lambda_{a2}$  (blue),  $\lambda_{a3}$  (green),  $\lambda_{a4}$  (orange), and  $\lambda_{a5}$  (red), whose sums are represented by black curves, have been fitted to the absorption spectra.

Figure 5-2a shows that P3HT-*b*-P4VP chains exist mostly as isolated chains in pure THF of a nonselective solvent of  $R = 0$ ; the absorption spectrum of P3HT-*b*-P4VP shows a broad featureless band with the maximum at 437 nm arising from the characteristic intrachain  $\pi$ - $\pi$  transition of P3HT. However, in mixed selective solvents of MeOH and THF, the absorption spectra of P3HT-*b*-P4VP shift to the red largely and their spectral band widths become broad on a large scale with the increase of the  $R$  value (Figure S5-2a), suggesting that P3HT-*b*-P4VP chains become aggregated gradually with the polarity increase of the medium to form P3HT@P4VP core-shell nanostructures (Figure 5-1). The red-shifted absorption of the P3HT block is generally observed in aggregate P3HT systems such as films and NFs having highly ordered packing and strong intrachain/interchain interactions. This suggests that the highly regioregular P3HT of P3HT-*b*-P4VP can self-organize to form semicrystalline lamellar morphologies when the fraction of MeOH in mixed selective solvents of MeOH and THF is high.

**TABLE 5-1. Spectral Positions of Gaussian Curves Fitted to Each Absorption Spectrum of P3HT-*b*-P4VP in Solutions of Different *R* Values**

<i>R</i>	$\lambda_{a1}$ (nm)	$\lambda_{a2}$ (nm)	$\lambda_{a3}$ (nm)	$\lambda_{a4}$ (nm)	$\lambda_{a5}$ (nm)
0.0	333±83 (30%) <sup>a</sup>	440±52 (70%)			
0.2	364±77 (36%)	445±51 (64%)			
0.5	322±96 (30%)	432±54 (41%)	491±45 (18%)	558±20 (6%)	601±22 (5%)
1.0	302±74 (20%)	428±56 (31%)	516±49 (38%)	558±18 (4%)	602±23 (7%)
2.0	224±126 (29%)	448±75 (33%)	512±40 (23%)	556±20 (7%)	600±20 (8%)
5.0	277±117 (22%)	453±74 (33%)	507±39 (26%)	555±21 (10%)	599±24 (9%)

<sup>a</sup>Absorbance percentage of each curve.

Whereas Figure 5-2b shows the absorption spectrum of P3HT-*b*-P4VP in mixed selective solvents at *R* = 0.2 can be deconvoluted into two Gaussian bands, Figure 5-2c displays that the spectrum at *R* = 5.0 has been deconvoluted into five Gaussian curves. A close examination in Table 5-1 reveals that the absorption spectra of P3HT-*b*-P4VP in mixture solvents of MeOH and THF with *R* values of  $\leq 0.2$  and  $\geq 0.5$  can be deconvoluted into two and five Gaussian curves, respectively. Each absorption spectrum of P3HT-*b*-P4VP in mixed solvents of  $R \leq 0.2$  can be deconvoluted into only two high-energy curves of  $\lambda_{a1}$  and  $\lambda_{a2}$  arising from the transition of free P3HT blocks of P3HT-*b*-P4VP chains because the influence of THF is still dominant. On the other hand, each absorption spectrum of P3HT-*b*-P4VP in mixed solvents at  $R \geq 0.5$  can be deconvoluted into two high-energy curves of  $\lambda_{a1}$  and  $\lambda_{a2}$ , arising from the transition of free P3HT blocks of P3HT-*b*-P4VP chains, and three low-energy curves of  $\lambda_{a3}$ ,  $\lambda_{a4}$ , and  $\lambda_{a5}$ , originating from the 0-2 ( $A_0$ -

2), 0-1 ( $A_{0-1}$ ), and 0-0 transitions ( $A_{0-0}$ ), respectively, of aggregated P3HT blocks of P3HT-*b*-P4VP. In mixed solvents of  $R = 0.5$ , the absorbance percentage of  $\lambda_{a1}$  and  $\lambda_{a2}$  curves due to the transition of free P3HT blocks in a high-energy region (71%) is much larger than that of  $\lambda_{a3}$ ,  $\lambda_{a4}$ , and  $\lambda_{a5}$  curves due to the transitions of aggregated P3HT blocks in a low-energy region (29%). However, in mixed solvents of  $R \geq 1.0$ , the absorbance percentage of the transitions of free P3HT blocks is similar to that of the transitions of aggregated P3HT blocks. Thus, Figure 5-2 and Table 5-1 have indicated that the polarity increase of the medium induces the H or J-type aggregation of hydrophobic P3HT blocks at the interior positions of P3HT@P4VP core-shell nanostructures.

The relative intensities of the origin (0-0) and the first-vibronic (0-1) transitions in the absorption spectra have been introduced to distinguish the dominant coupling type, H-type (interchain aggregate) or J-type (intrachain aggregate), in aggregate P3HT systems.<sup>21</sup> Information on the dominant coupling type and the coupling magnitude is associated with the intensity ratio of the 0-0 and the 0-1 transitions according to eq 1<sup>21-25</sup>

$$\frac{A_{0-0}}{A_{0-1}} = \left( \frac{1 - 0.24W / \omega_0}{1 + 0.073W / \omega_0} \right)^2 \quad (1)$$

where  $W$  is the exciton bandwidth and  $\omega_0$  is the vibrational energy of the symmetric vinyl stretch. Since the exciton bandwidth is related to the strength of excitonic coupling between adjacent chains, the dominant coupling type can be readily figured out by intensity difference between the 0-0 and the 0-1 vibronic transitions

of absorption spectra. When excitonic coupling within chains is stronger than excitonic coupling between neighboring chains, the 0-0 transition is allowed ( $\Sigma\mu \neq 0$ ) and more intense than the 0-1 vibronic sideband; this is often observed in J-aggregation-dominant nanostructures. On the other hand, when excitonic coupling between neighboring chains is stronger than excitonic coupling within chains, the 0-0 transition is forbidden ( $\Sigma\mu = 0$ ) and less intense than the 0-1 vibronic sideband; this is usually observed in H-aggregation-dominant nanostructures. As shown in Table 5-1, the absorbance ratio,  $A_{0-0}/A_{0-1}$ , of the 0-0 transition to the 0-1 vibronic transition in mixed solvents of  $R = 1.0$  is 1.75. On the other hand, when the  $R$  values of mixed solvents are 2.0 and 5.0, the  $A_{0-0}/A_{0-1}$  values become 1.14 and 0.90, respectively. Thus, Table 5-1 indicates that the J-aggregate character is predominant in mixed solvents of  $R = 1.0$  due to the effect of intrachain aggregation along the transverse axis, whereas the H-aggregate character is as important as the J-aggregate character in mixed solvents of  $R = 2.0$  or 5.0 due to the increase of interchain interactions along the longitudinal axis between neighboring chains with the polarity increase of the medium.

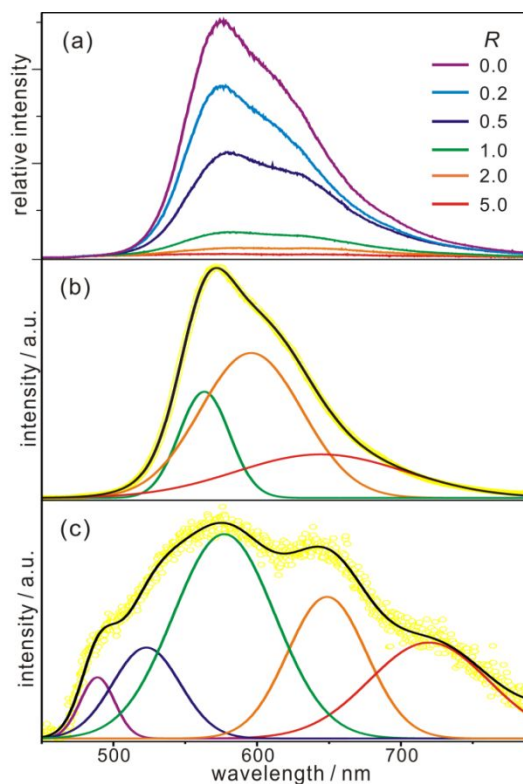


**Figure 5-3.** Emission spectra of P3HT-*b*-P4VP self-assembled in mixed solvents of indicated *R* values (a). Emission spectra (yellow circles) of P3HT-*b*-P4VP in mixed solvents of *R* = 0.2 (b) and 5.0 (c) with excitation at 355 nm; Gaussian curves of  $\lambda_{e1}$  (violet),  $\lambda_{e2}$  (blue),  $\lambda_{e3}$  (green),  $\lambda_{e4}$  (orange), and  $\lambda_{e5}$  (red), whose sums are represented by black curves, have been fitted to the emission spectra.

Figure 5-3a shows that the emission intensity of P3HT-*b*-P4VP in mixed selective solvents decreases gradually and drastically with the increase of the *R* value. Figure S5-2b displays that the spectral band width of P3HT-*b*-P4VP emission becomes broad significantly and stepwisely with the increase of the *R* value. These results also indicate that P3HT blocks associate to form aggregated nanostructures gradually with the polarity increase of mixed solvents, as described with Figure 5-2. The emission spectrum of P3HT-*b*-P4VP in pure THF (*R* = 0) is slightly different from that of pristine P3HT. The emission spectra of P3HT-*b*-P4VP and pristine

P3HT in THF commonly consist of two distinguished parts: the peak around 560 nm arising from the 0-0 transition of free chains due to the recombination of relaxed  $S_1$  excitons to the ground state and a shoulder around 620 nm arising from vibronic transitions related to the strong chain-stretching and torsional-twisting motions of polymer chains. However, the shoulder region due to the vibronic transitions is more eminent in the emission spectrum of P3HT-*b*-P4VP in THF than in that of pristine P3HT in THF, suggesting that vibronic transitions are enhanced when P3HT blocks are linked covalently to P4VP blocks.

**Table 5-2. Gaussian Curves Fitted to Each Emission Spectrum of P3HT-*b*-P4VP Self-Assembled from Mixed Solvents of Different *R* Values with Excitation at 355 nm**

<i>R</i>	$\lambda_{e1}$ (nm)	$\lambda_{e2}$ (nm)	$\lambda_{e3}$ (nm)	$\lambda_{e4}$ (nm)	$\lambda_{e5}$ (nm)
0.0			563±20 (21%) <sup>a</sup>	597±40 (53%)	646±68 (26%)
0.2			563±20 (19%)	596±42 (54%)	644±69 (27%)
0.5			567±25 (29%)	616±36 (33%)	638±78 (38%)
1.0	483±8 (1%)	512±24 (3%)	564±27 (23%)	616±45 (44%)	664±81 (28%)
2.0	490±15 (2%)	537±30 (14%)	577±28 (24%)	634±38 (40%)	711±50 (20%)
5.0	488±13 (4%)	521±27 (12%)	573±40 (40%)	643±31 (22%)	712±47 (22%)

<sup>a</sup>Intensity percentage of each curve.

Figure 5-3b and Table 5-2 indicate that each emission spectrum of P3HT-*b*-P4VP in mixed solvents of MeOH and THF at  $R \leq 0.5$  has been deconvoluted into three Gaussian curves consisting of  $\lambda_{e3}$ , arising from the 0-0 transition of free P3HT chains, and  $\lambda_{e4}$  and  $\lambda_{e5}$ , arising from the vibronic transitions of free P3HT chains,

suggesting that the influence of THF is still dominant in mixed solvents at  $R \leq 0.5$ . However, Figure 5-3c and Table 5-2 designate that each emission spectrum of P3HT-*b*-P4VP in mixed solvents at  $R \geq 1.0$  can be deconvoluted into five Gaussian curves of  $\lambda_{e1}$ ,  $\lambda_{e2}$ ,  $\lambda_{e3}$ ,  $\lambda_{e4}$ , and  $\lambda_{e5}$ . The  $\lambda_{e3}$  curve has already been ascribed to the recombination of relaxed  $S_1$  excitons to the ground state of free P3HT blocks. On the other hand, the  $\lambda_{e4}$  curve is attributed to the transition from the lowest-excited singlet state to the lowest vibrational level of the ground state (0-0) of aggregated P3HT blocks, and the  $\lambda_{e5}$  curve is due to transition from the lowest-excited singlet state to the first-excited vibrational level of the ground state (0-1) of aggregated P3HT blocks. Since H- and J-type excitonic couplings give rise to different selection rules, the nature of the couplings can be also determined readily from the quantitative differences of emission spectra. Thus, the intensity ratio,  $I_{em}^{0-0}/I_{em}^{0-1}$ , of the 0-0 transition to the 0-1 vibronic transition in emission can be used to identify the type and the strength of the dominant excitonic coupling. Table 5-2 shows that the  $\lambda_{e4}$  and  $\lambda_{e5}$  curves due to the 0-0 and the 0-1 transitions of aggregated P3HT blocks, respectively, are prevailing and spectrally separate by only 48 nm from each other in the emission spectrum of P3HT-*b*-P4VP in mixed solvents of  $R = 1.0$ . However, the  $\lambda_{e4}$  and  $\lambda_{e5}$  curves in the emission spectrum of P3HT-*b*-P4VP in mixed solvents of  $R = 2.0$  are spectrally separate largely by 77 nm. Furthermore, the  $I_{em}^{0-0}/I_{em}^{0-1}$  of P3HT-*b*-P4VP at  $R = 2.0$  is two times larger than that at  $R = 5.0$ . Thus, the spectral and the intensity changes of the  $\lambda_{e4}$  and  $\lambda_{e5}$  curves are considered to suggest that the dominant coupling type of P3HT-*b*-P4VP self-assembled in mixed selective solvents changes gradually from J-type aggregation into H-type

aggregation as the  $R$  value increases. Moreover, unlike the emission spectra of P3HT-*b*-P4VP in mixed solvents of  $R \leq 0.5$ , those in mixed solvents of  $R \geq 1.0$  have two additional peaks of  $\lambda_{e1}$  and  $\lambda_{e2}$  in a high-energy region from 483 nm to 537 nm, indicating that the conjugation length of P3HT is considerably reduced in a polar medium. Overall, Figure 5-3 and Table 5-2 have shown that the emission colors of self-assembled P3HT-*b*-P4VP nanostructures can be facilely tuned from the blue to the red by changing the polarity of the medium.

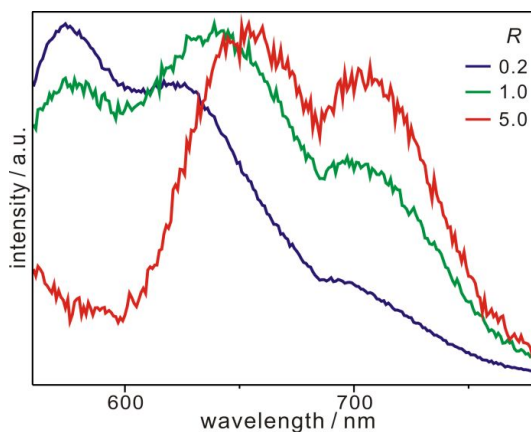


**Figure 5-4.** Peak-normalized emission spectra of self-assembled P3HT-*b*-P4VP in mixed solvents of indicated  $R$  values with excitation at 532 nm.

Since the excitation energy is another critical factor associated with the photophysical properties of aggregated P3HT systems, we have also obtained the emission spectra of P3HT-*b*-P4VP self-assembled in mixed solvents with excitation at 532 nm (Figure 5-4). As shown in Figure S5-3 and Table S5-1, each emission spectrum of P3HT-*b*-P4VP self-assembled in mixed solvents with excitation at 532 nm has been deconvoluted into three Gaussian curves of  $\lambda_{e3}$  at  $\sim 570$  nm,  $\lambda_{e4}$  at  $\sim 640$  nm, and  $\lambda_{e5}$  at  $\sim 710$  nm. The  $I_{em}^{0-0}/I_{em}^{0-1}$  of P3HT-*b*-P4VP in mixed solvents of  $R =$

1.0 is 2.0 times larger than that in mixed solvents of  $R = 5.0$ . This result is in agreement with the observation from the emission spectra with excitation at 355 nm in Table 5-2. Meanwhile, compared with the 0-0 transition of free P3HT blocks around 570 nm, the 0-0 and the 0-1 transitions of aggregated P3HT blocks around 640 and 710 nm, respectively, are stronger with excitation at 532 nm than the respective ones with excitation at 355 nm. In addition, the 0-0 and the 0-1 transitions of aggregated P3HT blocks deconvoluted from the emission spectrum of P3HT-*b*-P4VP in mixed solvents of  $R = 1.0$  with excitation at 532 nm are well separate by 72 nm, unlike those with excitation at 355 nm. Thus, the comparison of Figure 5-4 with Figure 5-3 has shown that the emission spectra of self-assembled P3HT-*b*-P4VP nanostructures are really sensitive to the excitation energy. The photophysical properties of self-assembled P3HT-*b*-P4VP nanostructures depending on the excitation energy will be further discussed with time-resolved emission kinetic profiles.

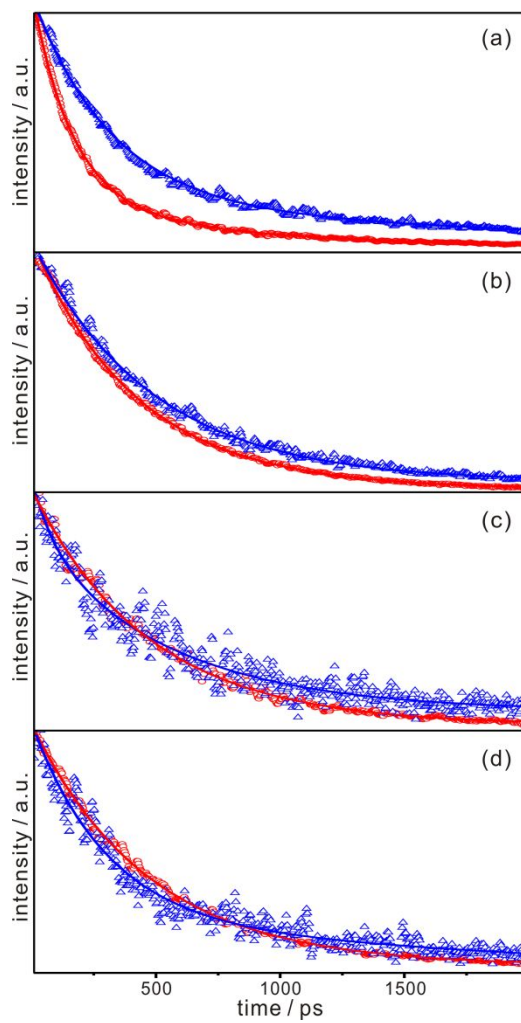


**Figure 5-5.** Emission kinetic profiles of P3HT-*b*-P4VP in mixed solvents of  $R = 0.2$  (red) and 5.0 (blue) excited at 355 nm and monitored at 451 (a), 572 (b), 651 (c), and 691 nm (d). Solid lines are best-fitted curves to extract kinetic constants.

**Table 5-3. Emission Kinetic Constants of P3HT-*b*-P4VP Self-Assembled in Mixed Solvents of MeOH and THF at various *R* Values**

<i>R</i>	$\lambda_{\text{ex}}$ (nm)	$\lambda_{\text{mon}}$ (nm)	decay time (ps)	mean time (ps)
0.2	355	451±12	180 (81%) + 1000 (19%) <sup>a</sup>	336
1.0			250 (81%) + 1600 (19%)	506
5.0			380 (81%) + 2800 (19%)	840
0.2		572±15	460 (95%) + 850 (5%)	480
1.0			470 (93%) + 1200 (7%)	521
5.0			470 (90%) + 1800 (10%)	603
0.2		651±4	450 (70%) + 800 (30%)	555
1.0			400 (70%) + 950 (30%)	565
5.0			280 (70%) + 1500 (30%)	646
0.2		691±4	330 (55%) + 780 (45%)	532
1.0			320 (55%) + 830 (45%)	549
5.0			180 (55%) + 1050 (45%)	571
0.2	532	610+	350 (90%) + 800 (10%)	395
1.0			250 (90%) + 900 (10%)	315
5.0			115 (95%) + 1800 (5%)	199

<sup>a</sup>Initial intensity percentage of each component.

We have obtained picosecond emission kinetic profiles of P3HT-*b*-P4VP in mixed selective solvents of different *R* values to gain a profound insight into the decay dynamics of relaxed S<sub>1</sub> excitons (Figure 5-5 and Table 5-3); the excited-state dynamics of P3HT-*b*-P4VP in mixed solvents is really dependent on *R* values and monitored wavelengths. The emission kinetic profiles of P3HT-*b*-P4VP nanostructures self-assembled in mixed solvents monitored at 451 nm (Figure 5-5a) and 572 nm (Figure 5-5b) reveal that mean decay times increase with the increase

of  $R$  value. As suggested by the appearance of two additional  $\lambda_{e1}$  and  $\lambda_{e2}$  curves in the static emission spectra of P3HT-*b*-P4VP at  $R \geq 1.0$ , the conjugation length of P3HT blocks are reduced extensively in a polar medium, resulting in the probability decrease of the nongeminate recombination of relaxed  $S_1$  excitons with the increase of the  $R$  value. It is known that emission around 580 nm with a lifetime of  $\sim 500$  ps arises from the recombination of the  $S_1$  excitons of non-aggregated P3HT chains.<sup>32,33</sup> Because the existence of torsional defects and the coil-like conformation of P3HT blocks make planarization difficult in the excited state, the recombination time of the  $S_1$  excitons of P3HT-*b*-P4VP in mixed solvents increases with the increase of the  $R$  value. Meanwhile, emission at 651 and 691 nm arises from the recombination of the relaxed  $S_1$  excitons of highly aggregated P3HT blocks in mixed solvents. High intrachain or interchain aggregation can form a high-energy singlet exciton (quasi-continuous band) *via* the singlet exciton-exciton annihilation (singlet fusion) due to the increase of interactions between adjacent  $S_1$  excitons in highly ordered regions. As shown in Table 5-3, the emission kinetic profiles of P3HT-*b*-P4VP nanostructures self-assembled in mixed solvents of various  $R$  values monitored at 650 and 690 nm have been deconvoluted into two decay components. The fast component decays on a shorter time scale than the recombination of normal relaxed  $S_1$  excitons ( $\sim 500$  ps) and its decay time decreases with the increase of the  $R$  value. Thus, we have assigned the fast component to the biexciton recombination; the recombination of one  $S_1$  exciton increases the recombination probability of adjacent  $S_1$  excitons.<sup>22</sup> Meanwhile, the slow decay component is due to the increased delocalization of relaxed  $S_1$  excitons induced by intrachain aggregation

associated with the regioregularity and planarity of polymer chains.<sup>22</sup> The lifetime of the fast emission decay component monitored at 650 and 690 nm decreases with the increase of the  $R$  value, whereas the lifetime of the slow emission decay component increases with the  $R$  value. These results suggest that high intrachain or interchain aggregation in P3HT-*b*-P4VP nanostructures self-assembled in mixed solvents generates delocalized  $S_1$  excitons, inducing nongeminate recombination effectively in a polar medium. As mentioned with the static emission spectra, emission decay around 650 nm originates from the 0-0 transition of aggregated P3HT blocks associated with J-type (intrachain) aggregation, and emission decay around 690 nm is due to the 0-1 vibronic transition of aggregated P3HT blocks associated with H-type (interchain) aggregation. Overall, the emission decay kinetic constants of P3HT-*b*-P4VP in mixed solvents at 690 nm are found to be shorter than those at 650 nm because two-dimensional interchain effect inducing the nongeminate recombination of relaxed  $S_1$  excitons is more important for the 0-1 vibronic transition than for the 0-0 transition.

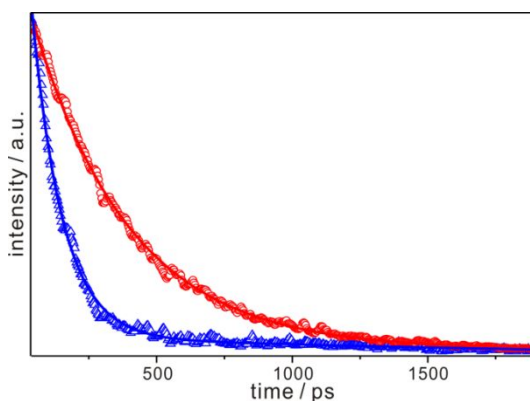


**Figure 5-6.** Emission kinetic profiles of P3HT-*b*-P4VP in mixed solvents of  $R = 0.2$  (red) and 5.0 (blue) excited at 532 nm and monitored at 610+ nm. Solid lines are best-fitted curves to extract kinetic constants.

We have also obtained the emission decay kinetic profiles of P3HT-*b*-P4VP in mixed selective solvents of different  $R$  values with excitation at 532 nm to further investigate the photophysical properties of self-assembled P3HT-*b*-P4VP nanostructures depending on the excitation energy (Figure 5-6). Table 5-3 shows that the initial intensity percentage of the fast decay component in the emission kinetic profiles of P3HT-*b*-P4VP self-assembled in mixed solvents is much larger with with excitation at 532 than with excitation at 355 nm. This result suggests that other charge carriers such as polaron pairs and polarons are generated rapidly from higher singlet exciton states in competition with vibrational relaxation.<sup>28,29</sup> As discussed with Figure 5-4, because higher singlet exciton states associated with the fast formation of charge carriers such as polaron pairs and polarons can be efficiently formed with the higher excitation energy, the 0-1 vibronic transition of aggregated chains at ~690 nm, arising from interchain aggregation, in the emission spectra of P3HT-*b*-P4VP self-assembled in mixed solvents is less intense with

excitation at 355 nm than with excitation at 532 nm. Thus, the 0-1 vibronic transition of aggregated chains at ~690 nm is eminent with excitation at 532 nm.

## 5. 5. Conclusions

Amphiphilic diblock-copolymer P3HT-*b*-P4VP consisting of poly(3-hexylthiophene) and poly(4-vinylpyridine) has been synthesized by the RAFT polymerization of 4-vinyl pyridine using a trithiocarbonate-terminated P3HT as a macro-RAFT agent. The emission colors, spanning from the blue to the red, of the self-assembled P3HT-*b*-P4VP nanostructures have been facilely tuned by altering the fraction of MeOH in mixed solvents of MeOH and THF. The emission kinetic profiles of P3HT-*b*-P4VP nanostructures self-assembled in mixed solvents monitored at 450 nm and 570 nm reveal that mean decay times increase due to the probability decrease of the nongeminate recombination of relaxed  $S_1$  excitons with the increase of the  $R$  value. As emission decay at 650 nm originates from the 0-0 transition of aggregated chains associated with J-type (intrachain) aggregation and emission decay at 690 nm is due to the 0-1 vibronic transition of aggregated chains associated with H-type (interchain) aggregation, the emission decay constants of self-assembled P3HT-*b*-P4VP are found to be shorter at 690 nm than those at 650 nm. This result indicates that two-dimensional interchain effect inducing the nongeminate recombination of relaxed  $S_1$  excitons is more important for the 0-1 vibronic transition than for the 0-0 transition. The initial intensity percentage of the fast emission decay component is much larger with with excitation at 532 than that

with excitation at 355 nm, suggesting that other charge carriers such as polaron pairs and polarons are generated rapidly from higher singlet exciton states in competition with vibrational relaxation.

## 5. 6. References

- (1) Noguez, C. *J. Phys. Chem. C* **2007**, *111*, 3806–3819. (b) Ray, P. C. *Chem. Rev.* **2010**, *110*, 5332–5365.
- (2) Kim, J.-Y.; Lee, D.; Kim, H. J.; Lim, I.; Lee, W. I.; Jang, D.-J. *J. Mater. Chem. A* **2013**, *1*, 5982–5988.
- (3) Kim, H.-B.; Jang, D.-J. *CrystEngComm* **2012**, *14*, 6946–6951.
- (4) Kim, S. J.; Ah, C. S.; Jang, D.-J. *Adv. Mater.* **2007**, *19*, 1064–1068.
- (5) (a) Scharber, M. C.; Mühlbacher, D.; Koppe, M.; Denk, P.; Waldauf, C.; Heeger, A. J.; Brabec, C. J. *Adv. Mater.* **2006**, *18*, 789–794. (b) Hains, A. W.; Liang, Z.; Woodhouse, M. A.; Gregg, B. A. *Chem. Rev.* **2010**, *110*, 6689–6735. (c) Lubber, E. J.; Buriak, J. M. *ACS Nano* **2013**, *7*, 4708–4714.
- (6) (a) Halls, J. J. M.; Pichler, K.; Friend, R. H.; Moratti, S. C.; Holmes, A. B. *Appl. Phys. Lett.* **1996**, *68*, 3120–3122. (b) Shaheen, S. E.; Brabec, C. J.; Sariciftci, N. S.; Padinger, F.; Fromherz, T.; Hummelen, J. C. *Appl. Phys. Lett.* **2001**, *78*, 841–843.
- (7) (a) Jamieson, F. C.; Agostinelli, T.; Azimi, H.; Nelson, J.; Durrant, J. R. *J. Phys. Chem. Lett.* **2010**, *1*, 3306–3310. (b) Albrecht, S.; Schindler, W.; Kurpiers, J.; Kniepert, J.; Blakesley, J. C.; Dumsch, I.; Allard, S.;

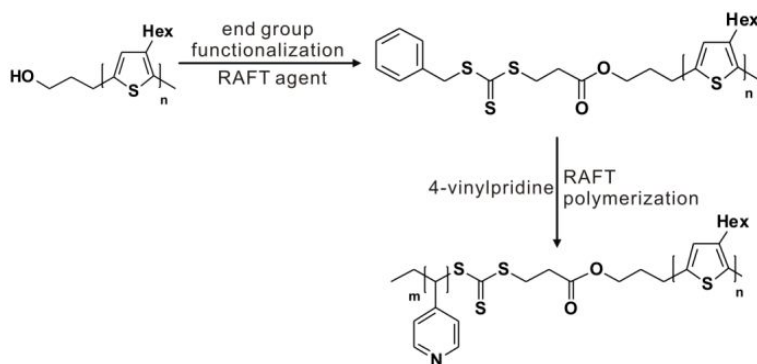
- Fostiropoulos, K.; Scherf, U.; Neher, D. *J. Phys. Chem. Lett.* **2012**, *3*, 640–645.
- (8) (a) Brenner, T. J. K.; McNeill, C. R. *J. Phys. Chem. C* **2011**, *115*, 19364–19370. (b) Luria, J. L.; Hoepker, N.; Bruce, R.; Jacobs, A. R.; Groves, C.; Marohn, J. A. *ACS Nano* **2012**, *6*, 9392–9401.
- (9) (a) Coakley, K. M.; McGehee, M. D. *Chem. Mater.* **2004**, *16*, 4533–4542. (b) Facchetti, A. *Chem. Mater.* **2011**, *23*, 733–758.
- (10) (a) Yamamoto, S.; Ohkita, H.; Benten, H.; Ito, S. *J. Phys. Chem. C* **2012**, *116*, 14804–14810. (b) Hou, J.; Chen, T. L.; Zhang, S.; Chen, H.-Y.; Yang, Y. *J. Phys. Chem. C* **2009**, *113*, 1601–1605. (c) Fischer, F. S. U.; Tremel, K.; Saur, A.-K.; Link, S.; Kayunkid, N.; Brinkmann, M.; Herrero-Carvajal, D.; López Navarrete, J. T.; Ruiz Delgado, M. C.; Ludwigs, S. *Macromolecules* **2013**, *46*, 4924–4931.
- (11) (a) Mao, Z.; Vakhshouri, K.; Jaye, C.; Fischer, D. A.; Fernando, R.; DeLongchamp, D. M.; Gomez, E. D.; Sauvé, G. *Macromolecules* **2013**, *46*, 103–112. (b) Richter, T. V.; Braun, C. H.; Link, S.; Scheuble, M.; Crossland, E. J. W.; Stelzl, F.; Würfel, U.; Ludwigs, S. *Macromolecules* **2012**, *45*, 5782–5788.
- (12) (a) Sary, N.; Richard, F.; Brochon, C.; Leclerc, N.; Lévêque, P.; Audinot, J.-N.; Berson, S.; Heiser, T.; Hadziioannou, G.; Mezzenga, R. *Adv. Mater.* **2010**, *22*, 763–768. (b) Lombardo, C. J.; Danielson, E. L.; Glaz, M. S.; Ooi, Z.-E.; Vanden Bout, D. A.; Dodabalapur, A. *J. Phys. Chem. B* **2013**, *117*, 4503–4509.

- (13) (a) Liao, H.-C.; Tsao, C.-S.; Lin, T.-H.; Jao, M.-H.; Chuang, C.-M.; Chang, S.-Y.; Huang, Y.-C.; Shao, Y.-T.; Chen, C.-Y.; Su, C.-J.; et al. *ACS Nano* **2012**, *6*, 1657–1666. (b) Tu, Y.-C.; Lin, J.-F.; Lin, W.-C.; Liu, C.-P.; Shyue, J.-J.; Su, W.-F. *CrystEngComm* **2012**, *14*, 4772–4776.
- (14) (a) Shen, H.; Bienstman, P.; Maes, B. *J. Appl. Phys.* **2009**, *106*, 073109. (b) Yen, W.-C.; Lee, Y.-H.; Lin, J.-F.; Dai, C.-A.; Jeng, U.-S.; Su, W.-F. *Langmuir* **2011**, *27*, 109–115.
- (15) (a) Park, S.-J.; Kang, S.-G.; Fryd, M.; Saven, J. G.; Park, S.-J. *J. Am. Chem. Soc.* **2010**, *132*, 9931–9933. (b) Lohwasser, R. H.; Thelakkat, M. *Macromolecules* **2012**, *45*, 3070–3077.
- (16) He, M.; Zhao, L.; Wang, J.; Han, W.; Yang, Y.; Qiu, F.; Lin, Z. *ACS Nano* **2010**, *4*, 3241–3247. (b) Gilroy, J. B.; Lunn, D. J.; Patra, S. K.; Whittell, G. R.; Winnik, M. A.; Manners, I. *Macromolecules* **2012**, *45*, 5806–5815.
- (17) Huettner, S.; Sommer, M.; Hodgkiss, J.; Kohn, P.; Thurn-Albrecht, T.; Friend, R. H.; Steiner, U.; Thelakkat, M. *ACS Nano* **2011**, *5*, 3506–3515.
- (18) Choi, S. Y.; Lee, J. U.; Lee, J. W.; Lee, S.; Song, Y. J.; Jo, W. H.; Kim, S. H. *Macromolecules* **2011**, *44*, 1771–1774.
- (19) Ahn, S.-k.; Pickel, D. L.; Kochemba, W. M.; Chen, J.; Uhrig, D.; Hinestrosa, J. P.; Carrillo, J.-M.; Shao, M.; Do, C.; Messman, J. M. *ACS Macro Lett.* **2013**, *2*, 761–765.
- (20) Palaniappan, K.; Hundt, N.; Sista, P.; Nguyen, H.; Hao, J.; Bhatt, M. P.; Han, Y.-Y.; Schmiedel, E. A.; Sheina, E. E.; Biewer, M. C.; et al. *J. Polym. Sci., Part A: Polym. Chem.* **2011**, *49*, 1802–1808.

- (21) (a) Spano, F. C.; Silva, C. *Annu. Rev. Phys. Chem.* **2014**, *65*, 477-500. (b) Yamagata, H.; Spano, F. *J. Chem. Phys.* **2012**, *136*, 184901. (c) Spano, F. *C. Acc. Chem. Res.* **2009**, *43*, 429-439.
- (22) (a) Baghgar, M.; Labastide, J. A.; Bokel, F.; Hayward, R. C.; Barnes, M. D. *J. Phys. Chem. C* **2014**, *118*, 2229-2235. (b) Labastide, J. A.; Baghgar, M.; McKenna, A.; Barnes, M. D. *J. Phys. Chem. C* **2012**, *116*, 23803-23811.
- (23) (a) Niles, E. T.; Roehling, J. D.; Yamagata, H.; Wise, A. J.; Spano, F. C.; Moule, A. J.; Grey, J. K. *J. Phys. Chem. Lett.* **2012**, *3*, 259-263. (b) Panzer, F.; Sommer, M.; Bässler, H.; Thelakkat, M.; Köhler, A. *Macromolecules* **2015**, *48*, 1543-1553.
- (24) Baghgar, M.; Labastide, J.; Bokel, F.; Dujovne, I.; McKenna, A.; Barnes, A. M.; Pentzer, E.; Emrick, T.; Hayward, R.; Barnes, M. D. *J. Phys. Chem. Lett.* **2012**, *3*, 1674-1679.
- (25) Carach, C.; Gordon, M. J. *J. Phys. Chem. B* **2013**, *117*, 1950-1957.
- (26) Thomas, A. K.; Garcia, J. A.; Ulibarri-Sanchez, J.; Gao, J.; Grey, J. K. *ACS Nano* **2014**, *8*, 10559-10568.
- (27) Barnes, M. D.; Baghar, M. *J. Polym. Sci. Pol. Phys.* **2012**, *50*, 1121-1129.
- (28) Guo, J.; Ohkita, H.; Bente, H.; Ito, S. *J. Am. Chem. Soc.* **2010**, *132*, 6154-6164.
- (29) Guo, J.; Ohkita, H.; Bente, H.; Ito, S. *J. Am. Chem. Soc.* **2009**, *131*, 16869-16880.
- (30) Ohkita, H.; Cook, S.; Astuti, Y.; Duffy, W.; Tierney, S.; Zhang, W.; Heeney, M.; McCulloch, I.; Nelson, J.; Bradley, D. D. C.; et al. *J. Am.*

- Chem. Soc.* **2008**, *130*, 3030–3042.
- (31) Cook, S.; Furube, A.; Katoh, R. *Energ. Environ. Sci.* **2008**, *1*, 294–299.
- (32) Ferreira, B.; da Silva, P. F.; Seixas de Melo, J. S.; Pina, J.; Maçanita, A. *J. Phys. Chem. B* **2012**, *116*, 2347–2355.
- (33) Lee, D.; Jang, D. *J. Polymer* **2014**, *55*, 5469–5476.
- (34) (a) Grancini, G.; Polli, D.; Fazzi, D.; Cabanillas-Gonzalez, J.; Cerullo, G.; Lanzani, G. *J. Phys. Chem. Lett.* **2011**, *2*, 1099–1105. (b) Grancini, G.; Biasiucci, M.; Mastria, R.; Scotognella, F.; Tassone, F.; Polli, D.; Gigli, G.; Lanzani, G. *J. Phys. Chem. Lett.* **2012**, *3*, 517–523.
- (35) (a) Banerji, N.; Cowan, S.; Vauthey, E.; Heeger, A. J. *J. Phys. Chem. C* **2011**, *115*, 9726–9739. (b) Banerji, N.; Seifert, J.; Wang, M.; Vauthey, E.; Wudl, F.; Heeger, A. J. *Phys. Rev. B* **2011**, *84*, 075206.
- (36) Kiriya, N.; Jähne, E.; Adler, H.-J.; Schneider, M.; Kiriya, A.; Gorodyska, G.; Minko, S.; Jehnichen, D.; Simon, P.; Fokin, A. A. *Nano Lett.* **2003**, *3*, 707–712.

## 5. 7. Supporting Information



Scheme S5-1. Synthesis of P3HT-*b*-P4VP.

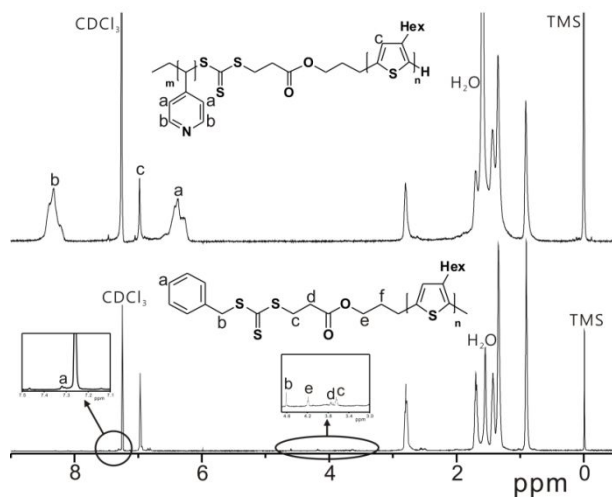
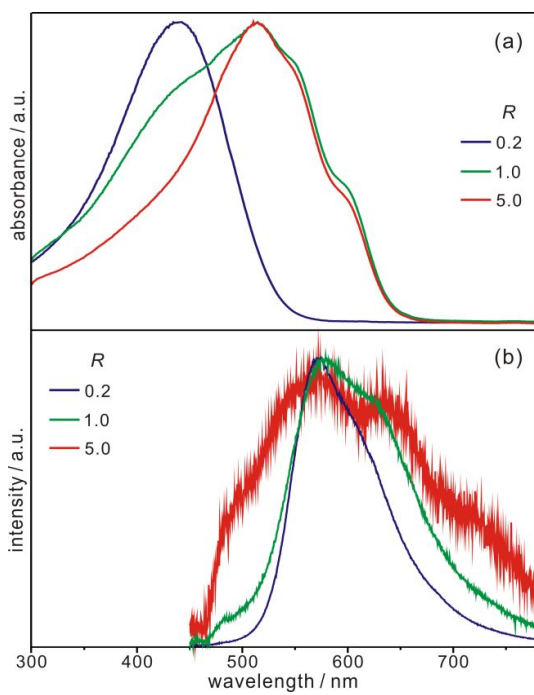
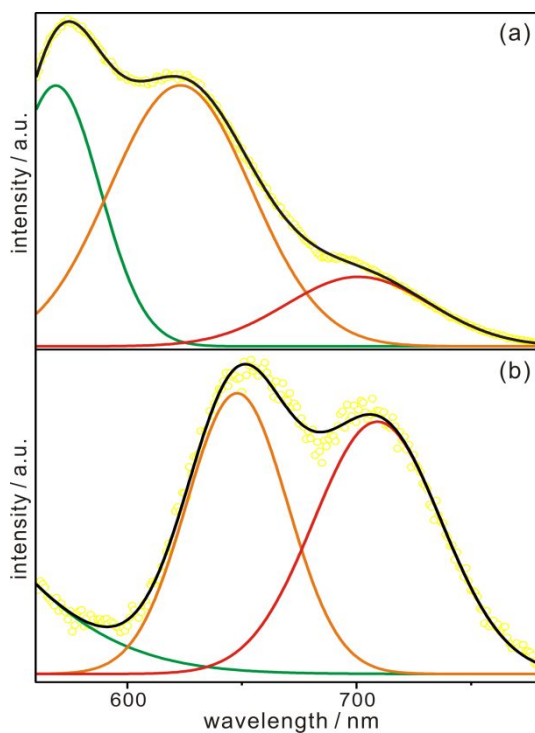


Figure S5-1. <sup>1</sup>H NMR spectra (500 MHz, CDCl<sub>3</sub>) of diblock copolymer P3HT-*b*-P4VP (top) and trithiocarbonate-terminated P3HT (bottom).



**Figure S5-2.** Maximum-normalized absorption (a) and emission spectra (b) of P3HT-*b*-P4VP in mixed solvents of indicated *R* values. Samples were excited at 355 nm for the emission spectra.



**Figure S5-3.** Emission spectra (yellow circles) of P3HT-*b*-P4VP in solutions at  $R = 0.2$  (a) and  $5.0$  (b) with excitation at  $532$  nm. Gaussian curves of  $\lambda_{e3}$  (green),  $\lambda_{e4}$  (orange), and  $\lambda_{e5}$  (red), whose sums are represented by black curves, have been fitted to the emission spectra.

**Table S5-1. Gaussian Curves Fitted to Each Emission Spectrum of P3HT-*b*-P4VP Self-Assembled from Mixed Solvents of Different  $R$  Values with Excitation at  $532$  nm**

$R$	$\lambda_{e3}$ (nm)	$\lambda_{e4}$ (nm)	$\lambda_{e5}$ (nm)
0.2	$568 \pm 23$ (33%)	$623 \pm 36$ (53%)	$700 \pm 37$ (14%)
1.0	$570 \pm 28$ (30%)	$640 \pm 35$ (48%)	$712 \pm 32$ (22%)
5.0	$560 \pm 75$ (19%)	$649 \pm 25$ (43%)	$709 \pm 32$ (38%)

<sup>a</sup>Intensity percentage of each curve.

## Appendix

### A.1. List of Publications

1. Mee Rahn Kim, **Dongki Lee**, and Du-Jeon Jang "Template-based electrochemically-controlled growth of segmented multi-metal nanorods" *J. Nanomater.* **2010**, 203756(1)-203756(7).
2. Mee Rahn Kim, **Dongki Lee**, and Du-Jeon Jang "Facile fabrication of hollow Pt/Ag nanocomposites having enhanced catalytic properties" *Appl. Catal. B: Environ.* **2011**, 103, 253-260.
3. **Dongki Lee**, Jiyeon Park, Mee Rahn Kim, and Du-Jeon Jang "Facile hydrothermal fabrication of hollow hexagonal hydroxyapatite prisms" *CrystEngComm* **2011**, 13, 5455-5459.
4. Jin-Ah Kwak, **Dongki Lee**, and Du-Jeon Jang "Facile fabrication of platinum nanobubbles having efficient catalytic degradation performances" *Appl. Catal. B: Environ.*, **2013**, 142-143, 323-328.
5. **Dongki Lee** and Du-Jeon Jang "Charge-carrier relaxation dynamics of poly(3-hexylthiophene)-coated gold hybrid nanoparticles" *Polymer*, **2014**, 55, 5469-5476.
6. **Dongki Lee**, Jaewon Lee, Ki-Hee Song, Hanju Rhee, and Du-Jeon Jang "Formation and decay of charge carriers in aggregated nanofibers consisting of poly(3-hexylthiophene)-coated gold nanoparticles" *Phys. Chem. Chem. Phys.* **2016**, 18, 2087-2096.
7. **Dongki Lee**, Joon Ki Kim, and Du-Jeon Jang "Excited-state dynamics of an amphiphilic diblock copolymer self-assembled from mixed solvents" *Submitted to The Journal of Physical Chemistry.*

8. **Dongki Lee**, Sugyeong Jeong, Jung-Hwa Park, Soo Young Park, and Du-Jeon Jang “Effects of gold nanorods on the excited-state dynamics and photovoltaic performances of hybrid nanocomposites containing poly(3-hexylthiophene)” *Submitted to The Journal of Physical Chemistry*.

## A.2. List of Presentations

### A.2.1. International Presentations

1. “Catalytic properties of hollow platinum nanoparticles” **Dongki Lee**, Mee Rahn Kim, and Du-Jeon Jang, Particles 2011, Berlin, Germany (**2011**)
2. “Facile hydrothermal fabrication of hollow hexagonal hydroxyapatite prisms” **Dongki Lee**, Ji Yeon Park, Mee Rahn Kim, and Du-Jeon Jang, 2012 Material Research Society Spring Meeting & Exhibit, San Francisco, USA (**2012**)

### A.2.2. Domestic Presentations

1. “Hollow Pt/Ag nanocomposites: galvanic fabrication and their enhanced catalytic properties” Mee Rahn Kim, **Dong Ki Lee**, and Du-Jeon Jang, The 106th Annual Meeting of Korean Chemical Society, Daegu, Korea (**2010**).
2. “Hollow Pt triangular nanoplates: galvanic fabrication and their enhanced catalytic properties” **Dongki Lee** and Du-Jeon Jang, The 108th Annual Meeting of Korean Chemical Society, Daejeon, Korea (**2011**).
3. “Fabrication of hollow platinum nanoplates via a galvanic replacement” **Dongki Lee** and Du-Jeon Jang, The 110th Annual Meeting of Korean Chemical Society, Busan, Korea (**2012**).
4. “Synthesis and spectroscopic study of organic/inorganic hybrid poly(3-hexylthiophene)-Au nanoparticles” **Dongki Lee** and Du-Jeon Jang, The 111th Annual Meeting of Korean Chemical Society, Goyang, Korea (**2013**).

5. “Facile self-assembly fabrication and time-resolved fluorescence study of hybrid Au@P3HT nanowires” **Dongki Lee** and Du-Jeon Jang, The 113th Annual Meeting of Korean Chemical Society, Goyang, Korea (2014).

## Abstract (Korean)

높은 위치선택성 폴리 3-헥실싸이오펜을 함유하고 있는 다양한 형태의 나노구조체를 합성하여 나노구조체 내부에서 생성되는 다양한 여기 상태의 동력학을 정류상태 그리고 시간분해 흡수 및 형광 분광학을 이용하여 연구하였다. 1 장에서는 폴리 3-헥실싸이오펜의 합성 방법과 특징적인 광학 성질 그리고 다양한 광학 소자에의 응용에 대해서 간단하게 기술하였다.

2 장에서는 폴리 3-헥실싸이오펜의 여기자와 금 나노입자에서 발생된 표면 플라즈몬 공명현상 간의 상호 작용에 대한 내용을 설명하고 있다. 높은 위치선택성 폴리 3-헥실싸이오펜의 말단에 싸이올기를 도입하여 손쉬운 방법으로 금 전구체를 환원하여 폴리 3-헥실싸이오펜으로 잘 기능화되어진 안정한 유/무기 금 나노 복합체 입자를 합성하였다. 전자현미경, X-선 회절 분석법, 그리고 열중량분석법 등의 다양한 기기 분석을 통하여 금 나노 입자가 고분자 기반 매체에 거대한 뭉침현상없이 안정하게 잘 분산되어있는 것을 확인하였다. 시간 분해 흡수 및 형광 분광학을 통해서 폴리 3-헥실싸이오펜의 여기자에서 금입자로 에너지 옮김 현상이 발생하여 합성된 나노구조체 내에서 생성된 일중항 여기자의 소멸 시간이 본래의 폴리 3-헥실싸이오펜 보다 더 빠르게 나타나는 것을 관측하였다.

3 장에서는 금 나노 막대 입자가 폴리 3-헥실싸이오펜의 여기상태와 유기태양전지 효율에 미치는 영향에 대한 내용을 기술하였다. 말단에 싸이올기가 도입된 폴리 3-헥실싸이오펜을 이용하여 69 nm 의 길이를 가지고 있는 금 나노 막대의 표면을 기능화하여 새로운 유/무기 나노 복합체를 합성하였다. 금 나노 막대 표면에 화학적으로 결합된 폴리 3-헥실싸이오펜의 고정된 가닥 구조 때문에 합성된 나노복합체의 일중항 여기자의 에너지 전달과 소멸시간이 본래의 폴리 3-헥실싸이오펜 보다

더 느리게 나타나는 것을 확인하였다. 또한 기존의 유기박막태양전지의 효율보다 합성된 나노구조체를 3% 첨가하여 제조한 유기박막태양전지의 효율이 27% 증가한 것을 확인하였다.

4 장에서는 높은 위치선택성 폴리 3-헥실싸이오펜을 함유하고 있는 유/무기 금 나노 복합체 입자의 자기조립 현상을 이용하여 합성한 두가지 다른 종류의 1 차원 나노구조체의 여기상태에 대한 내용을 기술하였다. 초고속 시간 분해 흡광 분광학을 이용하여 나노구조체 내부에서 생성되는 다양한 여기 상태의 생성과 소멸을 관찰하였다. 고분자 사슬내에서의 상호작용이 우세한 일차원 나노 구조체보다 고분자 사슬간의 상호작용이 우세한 일차원 나노 구조체의 일중항 소멸시간이 더 빠르게 관측되었다. 특히 기존에 보고된 여기상태항간교차 생성시간보다 더 빠른 삼중항 여기자의 생성 시간을 확인 함으로써, 폴리 3-헥실싸이오펜으로 구성된 일차원 나노 구조체 내에서 생성된 삼중항 여기자는 가장 낮은 일중항 에너지에서부터 시작되는 경로보다 더 높은 일중항 에너지 상태에서부터 더 효과적으로 생성된다는 것을 확인하였다.

5 장에서는 비극성 고분자인 폴리 3-헥실싸이오펜과 극성 고분자인 폴리 4 바이닐피리딘으로 구성된 양친매성 공중합체의 여기상태에 대한 내용을 기술하였다. 합성된 양친매성 공중합체를 무차별 용매인 테트라하이드로퓨란에 완벽하게 녹인후에 대표적인 극성용매인 메탄올을 서서히 첨가하면서 비극성 고분자인 폴리 3-헥실싸이오펜의 자기조립을 유도하였다. 메탄올의 첨가량이 증가 되면서 450, 650, 그리고 690 nm 부근에서 새로운 형광이 관찰하였다. 유도된 나노구조체 내부의 폴리 3-헥실싸이오펜의 감긴형태의 구조로 인하여 450 nm 파장에서 관찰된 일중항 여기자의 소멸 시간은 메탄올 함량의 증가와 함께 느려지는 것을 관찰하였으며, 폴리 3-헥실싸이오펜의 사슬내 그리고 사슬간의 상호작용으로 인하여 650 과 690 nm 파장에서 관찰된 일중항 여기자의

소멸 시간은 메탄올 함량의 증가와 함께 기존의 폴리 3-헥실싸이오펜의 소멸시간보다 더 빠르게 관찰이 되었다.

주요어: 나노복합체, 1 차원 나노구조체, 여기상태, 폴리 3-헥실싸이오펜, 자기조립, 표면 플라즈몬 공명, 시간분해 분광학

학번: 2011-30101